UNIVERSITY OF CALIFORNIA
Los Angeles

Mathematical Modeling and Theory of Microencapsulation and Inertial Migration.

A dissertation submitted in partial satisfaction
of the requirements for the degree
Doctor of Philosophy in Mathematics

by

Kyung Ha

2022

ABSTRACT OF THE DISSERTATION

Mathematical Modeling and Theory of Microencapsulation and Inertial Migration.

by

Kyung Ha
Doctor of Philosophy in Mathematics
University of California, Los Angeles, 2022
Professor Andrea Bertozzi, Chair

Abstract:

Microfluidics, fluid dynamics on the micro-scale, has been an active area of research due to its applications - separating particles, mixing fluids, and generating microdroplets. This thesis presents a mathematical model and analysis of two microfluidic technologies. The first is the use of micro-particles to form uniform microdroplets. We build a model using surface tension energy minimization to prove that the uniform distribution of droplets is an energy minimum distribution. Additionally, we use a random pairwise interaction model to understand the amount of mixing needed to achieve the uniform distribution. Based on this mathematical model we show that adding larger particles reduces the amount of mixing required and suggests an improved particle design.

The second is the focusing of particles flowing through a duct. Depending on both the size and shape of the particle and duct, the focusing can happen on different positions in the duct cross-section or not happen at all. Understanding the particle dynamics of the cross-section is important for the development of related technologies. We develop a simplified approximate model that combines the drag force due to Dean flow and the lift force with a single parameter

that characterizes the relative strength between the two. The cross-sectional dynamics of this model preserve that of the full model. The simplified model exhibits three distinct dynamics as the single parameter changes. We analyze the three cross-sectional dynamics and the bifurcations between them.

The dissertation of Kyung Ha is approved.

Christina Kim

Marcus Leigh Roper

Dino Di Carlo

Andrea Bertozzi, Committee Chair

University of California, Los Angeles

2022

TABLE OF CONTENTS

LIST OF FIGURES

LIST OF TABLES

ACKNOWLEDGMENTS

First, I would like to thank my advisor, Andrea Bertozzi, for her guidance and encouragement the past six years. I cannot imagine anybody else that could have been as helpful as you have been. You have gave me advice not only on the research but also on becoming a researcher.

I also want to thank Dino Di Carlo, his team - Chueh-Yu Wu, Ghulam Destgeer, Mengxing Ouyang, Joseph de Rutte, Vishwesh Shah, Alexis Joo, Simon Ng - for introducing me and guiding me throughout the microdroplet modeling problem. Dino Di Carlo has been a great collaborator explaining the science behind the problem, giving advice to improve my mathematical model and teaching me how to communicate mathematical results to a broader audience. I express extra thanks to Joseph de Rutte as he was the one who answered the questions when I started the research, which was extra helpful.

I cannot leave out the Andrea Bertozzi's postdocs and students who also worked on the microdroplet research. Bao Wang, Claudia Falcon, Wen Li, Sean Carney, Eric Hester, and Jason Brown, thank you so much for all the helpful discussions. Also, the UCLA 2019 REU summer research group - Ryan Shijie Du, Lily Liu, Simon Ng, Sneha Sambandam, Bernardo Hernandez Adame, Hansell Perez, Claudia Falcon - thank you for conducting the experiments and challenging me to improve my theory and communication skills. Especially Claudia Falcon, I thank you for showing how to be a good mentor during the REU research.

I thank Yvonne Stokes, Brendan Harding, Dan Stoecklein and Rahil Valani for working on the inertial migration phenomenon. Yvonne Stokes, thank you for introducing me to the problem and the hospitality during my visit at the University of Adelaide. Brendan Harding, thank you for answering all the questions during the visit.

Chapter 2 is adapted from [HRD22] and I acknowledge my coauthors Joseph de Rutte, Dino Di Carlo and Andrea Bertozzi. Joseph de Rutte provided the experimental expertise in the that has been incorporated in the introduction. Dino Di Carlo and Andrea Bertozzi

oversaw the research and provided inspiring ideas.

Chapter 3 is adapted from [DLN21] and I acknowledge my coauthors Ryan Shijie Du, Lily Liu, Simon Ng, Sneha Sambandam, Bernardo Hernandez Adame, Hansell Perez, Claudia Falcon, Joseph de Rutte, Dino Di Carlo, and Andrea Bertozzi. The 2019 UCLA REU members - Ryan Shijie Du, Lily Liu, Simon Ng, Sneha Sambandam, Bernardo Hernandez Adame, Hansell Perez - conducted the experiments and simulations, and wrote the paper. Claudia Falcon, Joseph de Rutte, I, Dino Di Carlo, and Andrea L Bertozzi mentored the team and provided the mathematical and experimental expertise.

Chapter 4 is adapted from [HHB22] and I acknowledge my coauthors Brendan Harding, Andrea Bertozzi, and Yvonne Stokes. Brendan Harding built the reduced model, and I analyzed the dynamics of the model. Andrea Bertozzi, and Yvonne Stokes guided the research and provided inspiring ideas. I also thank the Warkiani Laboratory at the University of Technology Sydney (https://www.warkianilab.com) for providing the photo of Figure 4.1b.

Although not adapted to this thesis I would also like to thank my coauthors of [GHH20] - Rachel Grotheer, Yihuan Huang, Pengyu Li, Elizaveta Rebrova, Deanna Needell, Longxiu Huang, Alona Kryshchenko, Xia Li, Oleksandr Kryshchenko - and my coauthors of [DST21] - David Davini, Bhargav Samineni, Benjamin Thomas, Amelia Huong Tran, Cherlin Zhu, Ganesh Dasika, Laurent White.

I also thank the generous funding that was provided by the Simons Foundation for supporting my research, Simons Math + X project (510776). In addition I would like to acknowledge the following grants that supported the research: Chapter 2 and Chapter 3 by the National Science Foundation Grant (EEC-1648451 and DMS-1659676); Chapter 4 by the Australian Research Council's Discovery Projects funding scheme (DP160102021 and DP200100834) and the Australian Research Council's Future Fellowship (FT160100108).

I would like to thank all my friends from UCLA. This includes everybody mentioned so far and Prof. Marcus Roper, Hangjie Ji, Wonjun Lee, Bumsu Kim, Kevin Bui, Shyr-Shea

Chang, Dohyun Kwon, Michael Puthawala, Dustan Levenstein, Gyu Eun Lee, Blaine Talbut, Zane Li, Christopher Shriver, Kaitlyn Shriver, Paul Han, Chanel Zee, Thomas Tu, Jacob Moorman, Chao Zehan, Francis White, Siting Liu, Yuzo Makitani, Kevin Bui and Brian Barch.

I would also thank the professors Woong Kook and Seung-Yeal Ha at my undergraduate university, Seoul National University, who encouraged me to pursue a Ph.D. degree and study applied mathematics.

I would like to mention my family, who has supported me and encouraged me to study abroad. My dad taught me mathematics when I was young after he came back from work. This inspired my interest in it. My mom encouraged me to keep on studying and comforted me when I was stressed. My younger brother always cheered me up, thank you all.

Finally I thank Bohyun Kim, my fiancée as she was always there to celebrate when papers got published, and there to help me when I was struggling. In 2016, I arrived at UCLA expecting a Ph.D. I did not know that I would meet you.

VITA

2016 B.S. (Mathematics), Seoul National University.

2016–2018 Teaching Assistant, Mathematics Department, UCLA.

2019 REU co-mentor, UCLA.

2021 RIPS academic mentor, IPAM.

2018–Present Graduate Student Researcher, Mathematics Department, UCLA.

PUBLICATIONS

C.-Y. Wu, M. Ouyang, B. Wang, J. de Rutte, A. Joo, M. Jacobs, K. Ha, A. L. Bertozzi, and D. Di Carlo, "Monodisperse drops templated by 3D-structured microparticles." In *Science Advances*, 6(45), 2020. *https://doi.org/10.1126/sciadv.abb9023*

R. Grotheer, Y. Huang, P. Li, E. Rebrova, D. Needell, L. Huang, A. Kryshchenko, X. Li, K. Ha, and O. Kryshchenko., "COVID-19 Literature Topic-Based Search via Hierarchical NMF." In *Proceedings of the 1st Workshop on NLP for COVID-19 (Part 2) at EMNLP 2020*, pp. 2569–2574. IEEE, 2020.

R. S. Du, L. Liu, S. Ng, S. Sambandam, B. H. Adame, H. Perez, K. Ha, C. Falcon, J. de Rutte, D. Di Carlo, A. L. Bertozzi, "Statistical energy minimization theory for systems of drop-carrier particles" *Physical Review E*, 104(1):015109, 2021. *https://doi.org/10.1103/PhysRevE.104.015109*

D. Davini, B. Samineni, B. Thomas, A. H. Tran, C. Zhu, K. Ha, G. Dasika, and L. White "Using physics-informed regularization to improve extrapolation capabilities of neural networks." In *Neurips 2021 "Machine Learning and the Physical Sciences" Workshop session*, 2021.

K. Ha, B. Harding, A. L. Bertozzi, and Y. M. Stokes. "Dynamics of small particle inertial migration in curved square ducts." In *SIAM Journal on Applied Dynamical Systems*, 2022. *https://doi.org/10.1137/21M1430935*

J. de Rutte, R. Dimatteo, M. M. Archang, M. van Zee, D. Koo, S. Lee, A. C. Sharrow, P. J. Krohl, M. Mellody, S. Zhu, J. V. Eichenbaum, M. Kizerwetter, S. Udani, K. Ha, R. C. Willson, A. L. Bertozzi, J. B. Spangler, R. Damoiseaux, and D. Di Carlo, "Suspendable Hydrogel Nanovials for Massively Parallel Single-Cell Functional Analysis and Sorting." In *ACS Nano*, 2022. *https://doi.org/10.1021/acsnano.1c11420*

K. Ha, J. de Rutte, D. Di Carlo, and A. Bertozzi, "Surface energy minimizing configurations for axisymmetric microparticles." In *Journal of Engineering Mathematics*, 2022. https://doi.org/10.1007/s10665-022-10216-9

CHAPTER 1

Introduction

Microfluidics, fluid dynamics on a micron-scale, has been an active area of research for the last twenty years propelled by the demands from microbiology [Di 09]. The applications include enhancing passive mixing of multiple fluids [WLW12], concentrating and separating particles and cells mixed in a sample [BBH10], and increasing biological and chemical assay sensitivity by using microdroplets [CND15].

Our two main research focus on mathematically modeling microfluidic phenomena and solving the challenges that arise from the development of such technologies. Chapters 2 and 3, a collaboration with Prof. Dino Di Carlo's group, considers the area of droplet microfluidics - generating micro-liter droplets using micro-sized particles [WOW20]. We show that the uniform distribution of droplets observed in the experiments agrees with the surface tension energy minimizing distribution (Chapter 2). We also conduct macroscale experiments to confirm the results and developed a probabilistic theory on the number of interactions needed to achieve the energy minimizing distribution (Chapter 3). Chapter 4, a collaboration with Prof. Yvonne Stokes' group, focuses on understanding the focusing of particles flowing in a curved duct. We construct a dynamical system of the migration of particles based on [HSB19] by reducing it into a single parameter model. Dynamic systems analysis shows that the simplified model and the complete model agree qualitatively (Chapter 4).

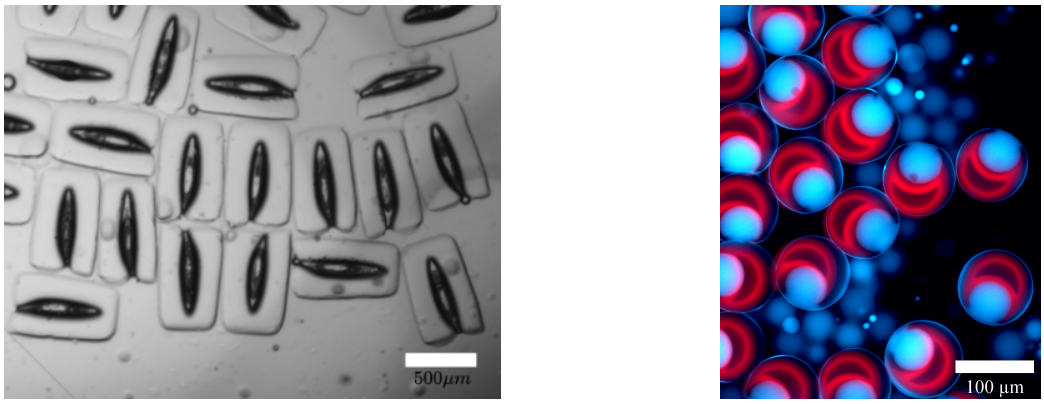

(a) (b)

Figure 1.1: Experimental photos of "dropicles". In both images, water is captured inside DCPs which are surrounded by oil. In (a) the DCPs are those in [WOW20]. The DCPs in (b) are those in [RDA22] and have a shape of a sphere with a hollowed out sphere. (b) is a false-color image, with the DCP colored in red and water colored in blue. The surrounding oil appears dark. (Reprinted figure with permission from [HRD22])

1.1 Generating Microdroplets using Microparticles

Uniform, fixed volume, microscale fluid droplets are a powerful tool for performing high-throughput bioassays [BHW07, MRK20] as well as single-cell analyses [WGZ14, WB10, MBS15]. A benefit of such technology is that by compartmentalizing a larger volume into sub-components, individual cells or molecules can be analyzed more precisely. This is due to the secretion of molecules from a cell, or the products of reactions of individual molecules, accumulating at high concentrations when confined at small volumes. Conventional technologies focus on droplet formation and manipulation via flow in microchannels [KKN97, ABS03, TCL06] or in electrowetting devices [LBF08, NK12, XZG17]. The downsides to these approaches are that the droplets generated are energetically unstable and eventually coalesce; and they require expensive microfluidic equipment and specialized skills, limiting the adoption of the techniques in most research labs [MHR10].

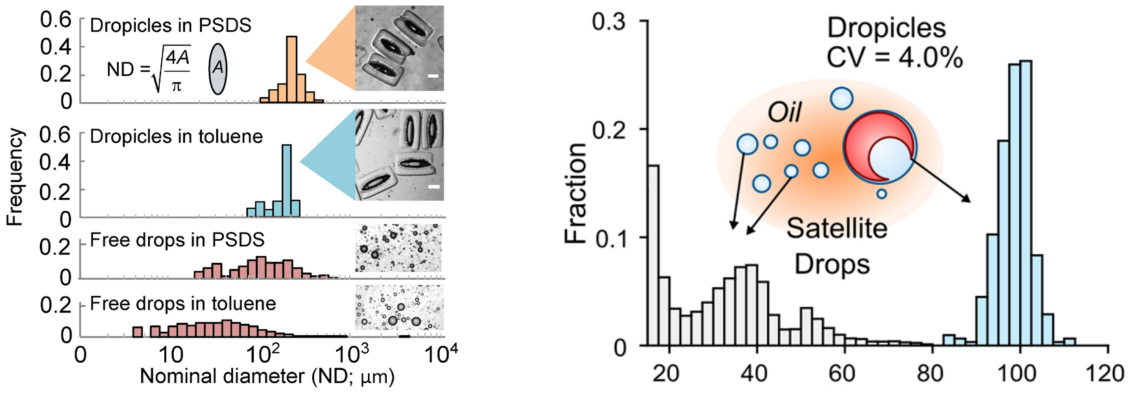

(a) (b)

Figure 1.2: Histograms of the size of the water droplets with and without DCPs. The DCPs are those shown in Figure 1.1 respectively. Compared to droplets that are not attached to the DCPs, droplets captured by the DCPs are uniform in size. (a) is reprinted from [WOW20] (© The Authors, some rights reserved; exclusive licensee AAAS. Distributed under a CC BY-NC 4.0 License) and (b) is reprinted with permission from [RDA22]. Copyright 2022 American Chemical Society.

Recently, Drop-Carrier Particles (DCPs) have emerged as an alternative microparticle-based approach to create uniform compartments for performing biological assays [WOW20, DOW20, DOD21, LRD21, RDA22] (Figure 1.1). With a complex geometry comprised with a hydrophilic inner part and hydrophobic outer part the DCPs capture uniform-sized droplets by having favored surface energy conditions (Figure 1.2). These DCPs result in isolated water droplets on the nanoliter or sub-nanoliter scale when simply mixed by pipetting. These droplet-particle complex, which we refer as dropicles, are energetically stable and do not coalesce or exchange fluids with each other (Figure 1.3). Molecules accumulating in these small volumes can also bind to the DCP, enabling analysis with standard equipment such as flow cytometers. This can lead to "lab on a particle" technologies in which experiments can be done on thousands of individual cells. Another advantage of the DCP technology is that they can be manufactured in bulk elsewhere and delivered to the labs.

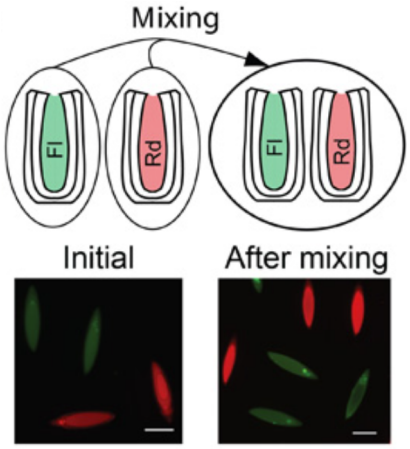

Figure 1.3: The dropicles do not exchange fluids with each other. Images of two groups -red and green- of dropicles before agitation (left) and after agitation (right). Notice that the color of the droplets stay the same after agitation, demonstrating that the fluids do not exchange fluid once formed. Reprinted from [WOW20] (© The Authors, some rights reserved; exclusive licensee AAAS. Distributed under a CC BY-NC 4.0 License).

The DCPs can be manufactured in different shapes and with different materials; it is important to optimize the DCPs to enhance performance (Figure 1.4). For applications of DCPs, an optimal design is one that (a) captures a uniform and predetermined amount of target fluid once fully mixed (b) reduces the amount of mixing required to achieve this fully mixed state and (c) reduces the number of DCPs that are connect to each other by the target fluid. Although the performance of a DCP can be measured by direct physical experiments, this is expensive. We develop a mathematical framework using surface energy minimizing surfaces and random pairwise interactions that provides a theory that measures a DCPs performance on (a) and (b).

DCPs are sufficiently small so that surface tension dominates the equilibrium physics and other forces (e.g. buoyancy) are ignored. Therefore we use the theory of minimal energy surfaces with volume constraints to study the equilibrium configurations for a variety of fixed volumes and DCPs shapes and sizes. This is a classic problem in geometry [BBW98,

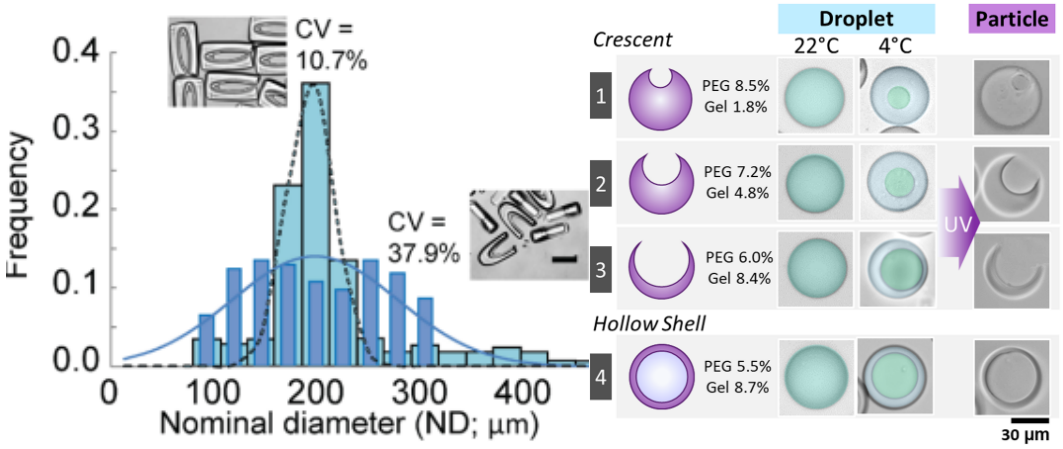

(a) (b)

Figure 1.4: Different shaped particles can be manufactured. The DCPs are those shown in Figure 1.1 respectively. (a) shows two different DCPs perform differently, one has a tighter distribution than the other. (b) shows that the composition of the chemicals change the shape and size of the inner cavity. (a) is reprinted from [WOW20] () and (b) is reprinted with permission from [LRD21],

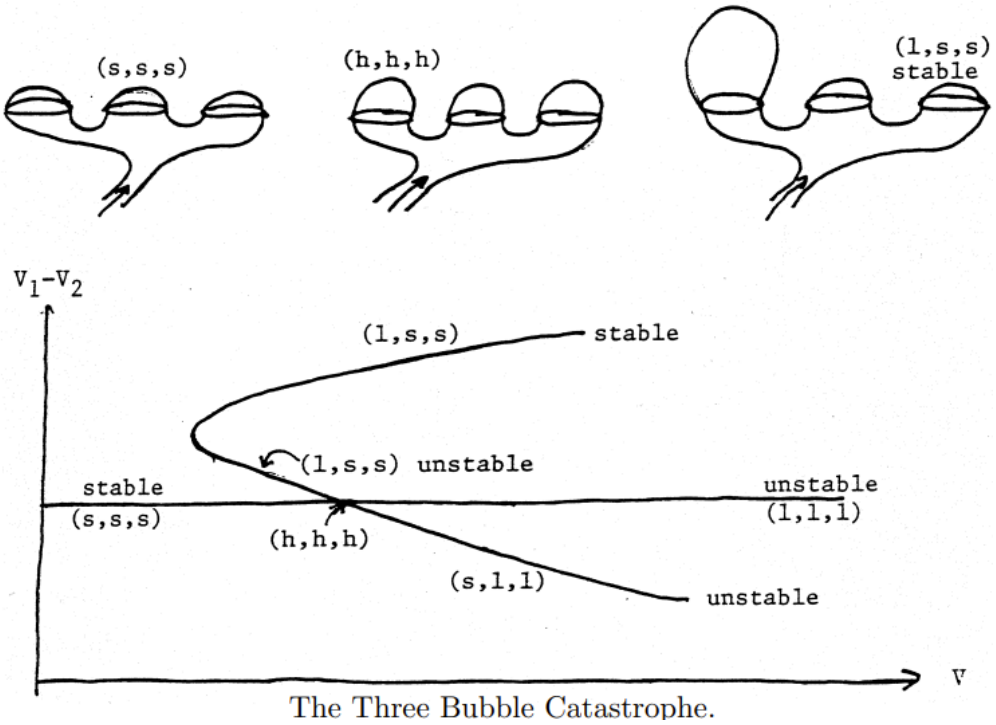

Figure 1.5: Volume distribution of a three orifice system. The stable distribution of volume is one orifice with large volume and the rest with uniform small volumes. From [Wen99]. Used with permission.

BS15]. One especially well-documented case is the problem of a liquid bridge between two axisymmetric surfaces. Common examples of such surfaces are spheres [MC65, PMC00, REM05] and flat parallel planes - two infinitely large planes [SAP02, Str92, Vog87, Vog89, Zho97], two finite sized planes [EGD70, GD71, SSA12, RS86, LS97, LS95, GD72, SP96] and a combination of the two [AHV15]. Results with more general shapes are well documented in [MBK87].

Once we calculate the energy of a single DCP with fluid volume V, $E(V)$, we minimize the energy of a multi-DCP system with fluid volume V_T, i.e.,

$$\min_{\Sigma V_i = V_T} \Sigma E(V_i).$$

For this system we prove that all except one of the DCPs fluid volume is identical, provided V_T is large enough. A similar volume distribution is observed in fluid-solid interfacial systems with multiple orifices [Wen99, VS10, HS19]. This is also a surface energy minimization problem with a volume constraint, which results in uniform small droplets forming on top of the orifices (Figure 1.5). However, for the orifices the uniform volume decrease to 0 as the total volume of the system increases, while in the DCP system the droplet volume has a non-zero lower bound.

We simulate how the DCPs exchange fluid by using a random pairwise interaction model. The random pairwise interaction model assumes that two random particles exchange fluid among themselves to minimize the energy of the two DCP system. The energy minimization theory of two DCP system agrees with the physical experiments. Also using this model we build a statistical theory on the number of interactions needed to generate a uniform distribution. Based on the statistical theory we optimize the shape of the DCP.

Throughout the thesis, we follow the terminology in [WOW20, DOW20, DOD21, LRD21, RDA22], by denoting the target liquid as water, the surrounding liquid as oil. We likewise denote the water-DCP complex as a "dropicle" (drop+particle). The particles are either hydrophilic particles (Chapter 2) or a combination of an inner hydrophilic layer and an outer hydrophobic layer (Chapter 3).

1.2 Inertial microfluidics in a curved square duct

Inertial lift is a phenomenon, first reported by Segre and Silberberg [SS61], that causes particles and cells suspended in flow through microscale devices to deviate from fluid streamlines. The applications of this effect are revolutionizing diagnostic medical technologies, the separation and identification of circulating tumor cells (CTCs) being one of many examples [LSB13, WGL14]. Other general uses include flow cytometry, rare cell isolation, cell cycle synchronization, platelet and bacteria separation, plasma extraction, particle classification,

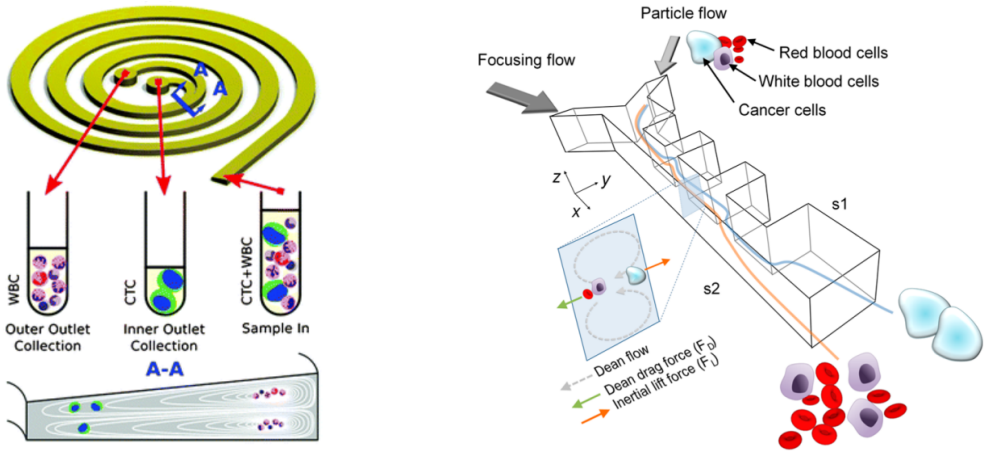

(a) (b)

Figure 1.6: Inertial microfluidic technology used to detect circulating tumor cells. They use a spiral channel with a trapezoid cross-section and a contraction-expansion array, respectively. (a) is reproduced from [WGL14] with permission from the Royal Society of Chemistry and (b) is reprinted with permission from [LSB13], Copyright 2013, American Chemical Society.

and fluid mixing [MT14]. While the effect of inertial lift on particle migration has been extensively studied for uni-directional flows [HL74, SH89, Asm99, MMG04, HLR15], many of the devices used in cutting edge microfluidics have a complex design through which there is a full three-dimensional flow. Some of the more recent advances in this field, experimental and otherwise, are described in several review articles [Di 09, GF14, SR20].

Hood et. al [HLR15] analyzed inertial migration of a neutrally buoyant spherical particle suspended in flow through a straight duct with square cross-section (Figure 1.7). As the analysis of the fully enclosed flow is challenging, they applied a combination of perturbation theory and numerical computation. Motivated by their approach, Harding et al. [HSB19] extended this work to consider the inertial migration of a neutrally buoyant spherical particle suspended in flow through curved ducts with square, rectangular and trapezoidal cross-sections (Figure 1.8); they found that rectangular and trapezoidal cross-sections had a better ability to separate particles depending on their size and these cross-sections became the primary focus

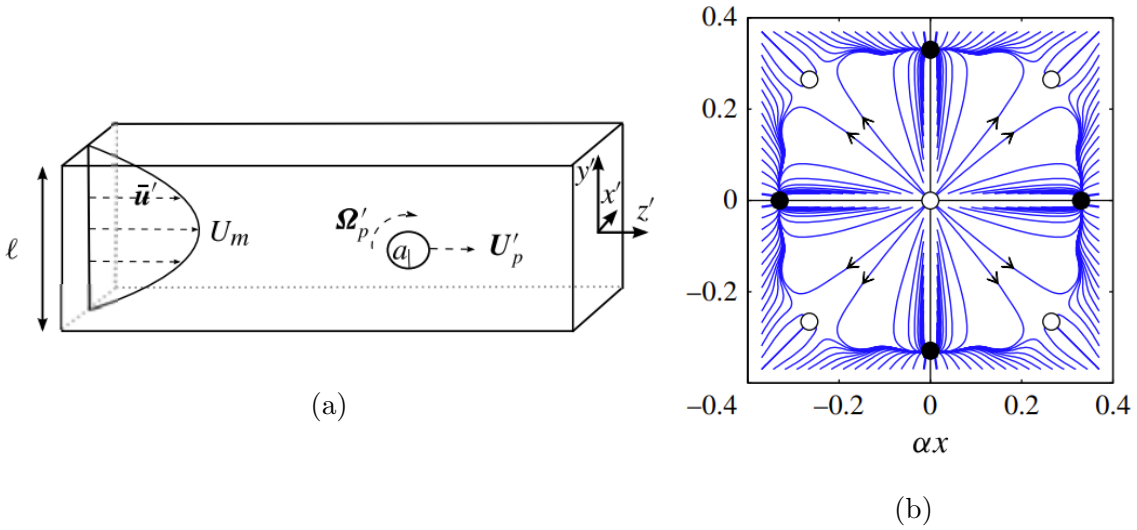

Figure 1.7: Straight duct dynamics. (a) shows the a spherical neutrally buoyant particle suspended in a straight duct flow. (b) is the cross-sectional dynamics of the particle for a particular particle size and Reynolds number. Figures are reproduced from [HLR15] (Copyright © © 2015 Cambridge University Press).

of the results presented. In particular, they demonstrated that the lateral focusing location within curved ducts with a rectangular cross-section could be approximately characterized by a dimensionless parameter κ which approximates the relative strength of the two primary drivers of particle migration - secondary flow drag to the inertial lift force. Although the paper only considered the migration of a single particle, it provides a good prediction of the behavior of sufficiently dilute suspensions in which particle-particle interaction is minimal.

In chapter 4 of this thesis we focus on curved ducts with a square cross-section which, as seen in [HSB19], exhibit a variety of interesting migration dynamics that warrant further investigation. To achieve this we construct a model of the migration forces on a particle in a curved duct which is simple to evaluate whilst still capturing the topological structure which is essential for accurate prediction of migration dynamics. The model combines the two dominant cross sectional forces - the lift force, L, and drag force due to Dean flow, D -

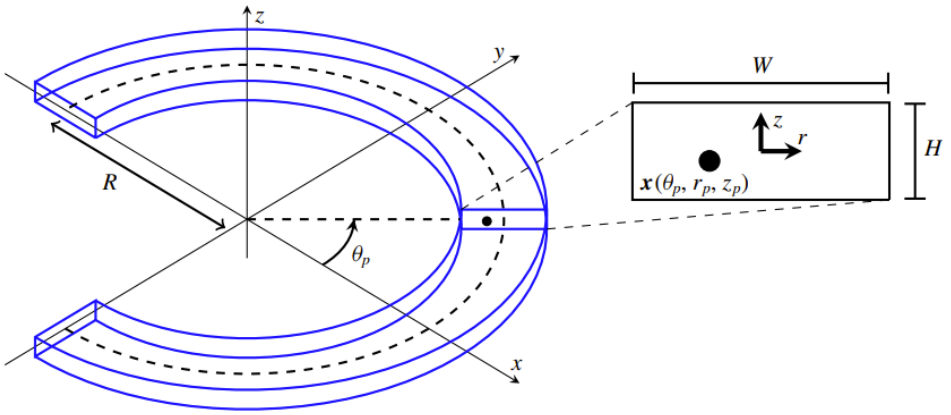

(a)

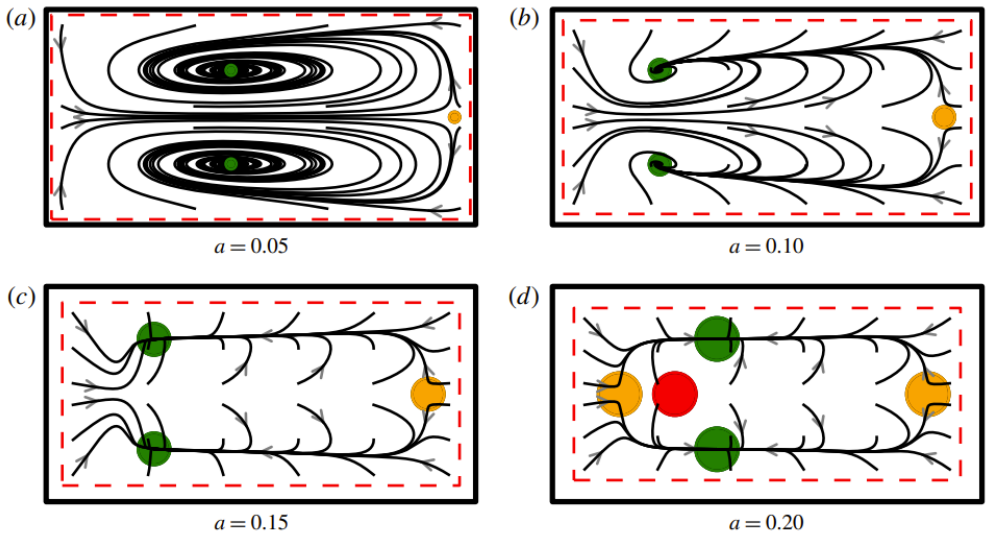

(b)

Figure 1.8: Curved duct dynamics. (a) shows the a spherical neutrally buoyant particle suspended in a curved duct flow. (b) is the cross-sectional dynamics of the particle as the particle size changes for a given duct shape and duct radius. Figures are reproduced from [HSB19] (Copyright © © 2019 Cambridge University Press).

and a dimensionless constant κ that characterizes the relative strength between the two, i.e.,

$$L/\kappa + D.$$

Based on this model we classify three distinct flow profiles and analyze the dynamics of each system and bifurcations between the profiles. We also add the dynamics through the cross-section and provide an analysis on the duct length needed to focus a majority of the particles.

CHAPTER 2

Minimal surface configurations for axisymmetric drop-carrier particles

This chapter is based on [HRD22] (Reprinted manuscript with permission from [HRD22] as follows:Ha, Kyung, et al. Journal of Engineering Mathematics 134.1 (2022): 1-19. by Springer Nature. https://doi.org/10.1007/s10665-022-10216-9).

2.1 Introduction

In this chapter, we investigate surface energy minimizing configurations for relatively complex axisymmetric DCPs compared to those that have been studied in the literature (Fig. 2.1). The axisymmetry reduces the ensuing minimization problem to a 1D problem which is relatively straightforward that enables us to derive rigorous results. Such a symmetry often corresponds to simplified manufacturing technologies for producing such DCPs in bulk. It is possible to achieve these energy minimizing configurations without the axisymmetric assumption using 3D simulations as in [WOW20]. However, this is computationally expensive compared to 1D simulations. Once we obtain the configuration of a single DCP we study the multi-DCP system and its minimal energy distribution given a fixed volume of fluid. We develop a theory for the minimum energy configuration of multi-DCP systems and perform simulations of pairwise interactions.

This chapter is organized as follows. In section 2.2, we explore three DCP configurations of interest: planar surfaces, hollow spheres, and hollow cylinders (Fig. 2.1). We deduce the

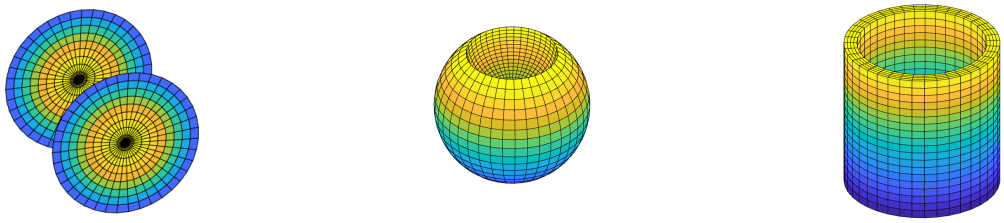

(a) Two parallel flat planes (b) Hollow sphere (c) Hollow Cylinder

Figure 2.1: Shapes of axisymmetric solids. A cross-section of (b) and (c) are shown in Fig. 2.2b and 2.2c respectively.

shape of the energy minimizing configuration and calculate the volume-energy graph for each DCP. In section 2.3, we develop a rigorous theory regarding the minimal configuration for a multi-DCP system, starting with the case of a two-DCP system. We can predict the minimal energy distribution of multi-DCP systems by observing properties of the volume-energy graph of a single water-DCP complex. In section 2.4, we simulate the interaction between two and multiple DCPs using a random pairwise interaction model. The simulation verifies the results in section 2.3 and also suggests guidelines for DCP design.

2.2 Energy minimizing surfaces

In this section, we focus on finding the minimal energy surface configuration for a given DCP and volume. By repeating these calculations for different volumes, we draw a volume-energy graph ($V - E$ graph) of a DCP.

Denote the fixed solid region by S, the finite volume of water by Ω, the water-solid interface by $\partial\Omega_{WS}$ and the water-oil interface by $\partial\Omega_{WO}$. Note that $\partial\Omega = \partial\Omega_{WS} \cup \partial\Omega_{WO}$ (Fig.

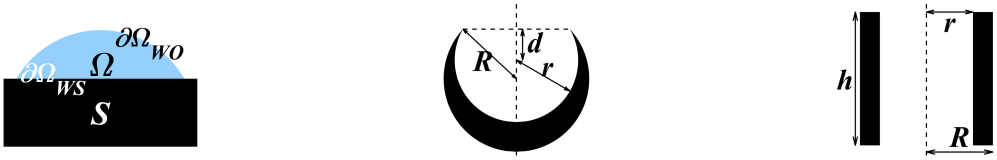

(a) (b) (c)

Figure 2.2: Examples of axisymmetric solid surfaces. (a) is a droplet (blue) on a flat surface (black). (b) and (c) are cross-sections of a hollow sphere and a hollow cylinder, respectively, with the axis of symmetry shown as a dotted vertical line. The solid phases are colored in black. In (b), R and r are the radii of the outer and inner spheres respectively, and d is the offset between the tip of the DCP and the center of the inner sphere. In the figure the parameters are $R = 1.18$, $r = 1$, and $d = 0.5$. In (c), h is the height and R and r are the inner and outer radius of the cylinder. In the figure the parameters are $R = 0.9$, $r = 0.7$ and $h = 3$.

2.2a). The interfacial tension energy of the dropicle is

$$\begin{aligned} E(\Omega) &= \sigma_{WO}|\partial\Omega_{WO}| + \sigma_{WS}|\partial\Omega_{WS}| + \sigma_{OS}(|\partial S| - |\partial\Omega_{WS}|) \\ &= \sigma_{WO}|\partial\Omega_{WO}| + (\sigma_{WS} - \sigma_{OS})|\partial\Omega_{WS}| + \sigma_{OS}|\partial S| \end{aligned} \tag{2.1}$$

where $|\partial S|$ is the surface area of the solid, $|\partial\Omega_{WO}|$ and $|\partial\Omega_{WS}|$ are the water-oil and water-solid surface areas of Ω respectively, σ_{WS}, σ_{WO} and σ_{OS} are surface tensions between water-solid, water-oil and oil-solid respectively. We consider DCPs with a partial wetting hydrophilic solid phase, i.e.

$$\sigma_{WO} > \sigma_{OS} - \sigma_{WS} > 0. \tag{2.2}$$

Throughout this thesis we use the surface tensions values $\sigma_{WO} = 1$, $\sigma_{WS} = 0.1$, and $\sigma_{OS} = 0.9$, unless stated otherwise. This choice is consistent with the use of hydrophilic materials for the DCPs in the experiments [WOW20, DOW20, LRD21, RDA22]. Qualitatively the results do not change much with modest variation in these parameters (c.f. Section 2.4.2). We note that the last term in (2.1) only depends on ∂S and is independent of the water domain Ω so

we ignore it as far as the minimal energy calculation is concerned. Also, we note that the energy equation does not take any dynamics around the dropicle into account, and therefore our model is a static fluid model. We need to find an Ω that minimizes the energy (2.1) under the volume constraint $|\Omega| = V$. Since the ratio of surface energies determine the static problem the energy can be dimensionless. Throughout this thesis, we assume that for each dropicle Ω is an open bounded and connected domain.

Solving (2.1) is well documented in [MBK87] chapter 2. The minimizing surface is a constant mean curvature surface, with a prescribed contact angle α satisfying,

$$cos\alpha = (\sigma_{OS} - \sigma_{WS})/\sigma_{WO} \tag{2.3}$$

called the Duprè-Young condition for smooth solid surfaces. For sharp surfaces (e.g. tips of Fig. 2.2b) we consider a range of contact angles rather than a single choice. The range depends on α and the angle of the sharp solid. A way to understand this is by smoothing the sharp surface locally and applying the condition in (2.3) to a specific point in the smoothed area.

The physical cases of interest here are all axisymmetric connected solids (Fig. 2.1b and 2.1c), with simply connected axisymmetric water domains. Under these assumptions, the water-oil interface $\partial\Omega_{WO}$ of the problem (2.1) is part of a sphere.

Theorem 2.2.1. *Assume the surface tensions satisfy the partial wetting condition (2.2) and the solid is axisymmetric and connected. Also, assume that the water domain is bounded, simply connected and axisymmetric. Then the water-oil interface that minimizes (2.1) is part of a sphere.*

Proof. This theorem summarizes results discussed in detail in [MBK87] chapter 2.4.4. □

The rest of this section uses this theoretical result to compute the energy-volume curves for the DCP shapes of interest. We start with the classical case of two parallel planes, which

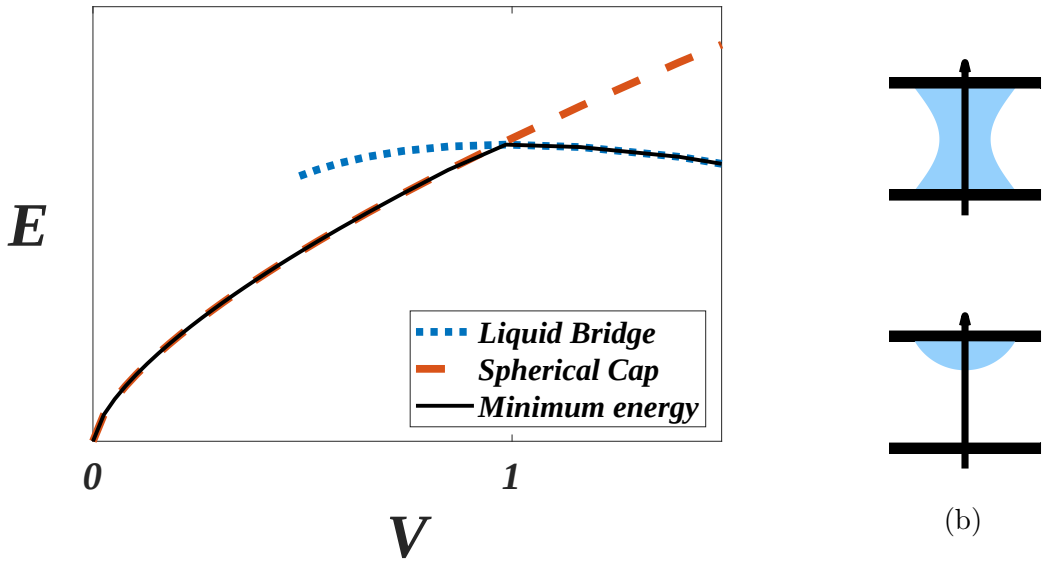

(a) (b)

Figure 2.3: Parallel plane dropicles. (a) is the $V - E$ graph of water droplets with different geometries. They are a liquid bridge on the parallel plane, and a spherical cap on one side, with their cross-sections shown in (b) respectively. The minimum energy curve is represented as a black solid line. The unit volume is $(2a)^3$ where $2a$ is the distance between the parallel planes.

are well-studied in the literature, to contrast with the hollow DCP shapes that are less well-studied.

2.2.1 Two parallel planes

The parallel plane case is well-known [Vog89]. In this case, there are two types of geometries to consider for Ω: (a) a droplet that only touches one of the planes or (b) a bridge between the two planes.

Spherical cap: For the case where the water only comes into contact with one of the planes, since the surface is connected and axisymmetric, we obtain a spherical cap as the

minimizer by applying Theorem 2.2.1. The size and shape of the sphere are decided from the volume constraint and the Duprè-Young condition.

Liquid bridge : For the case when water connects both planes of distance $2a$, using calculus of variations, it is known [Vog89] that an axisymmetric bridge forms with shape profile $f(x)$ between $-a$ and a satisfying,

$$\frac{f''}{(1+(f')^2)^{3/2}} - \frac{1}{f(1+(f')^2)^{1/2}} = 2H \tag{2.4}$$

where H is the Lagrange multiplier corresponding to the volume constraint, with Neumann boundary conditions

$$f'(-a) = \frac{\sigma}{\sqrt{1-\sigma^2}}, \quad f'(a) = -\frac{\sigma}{\sqrt{1-\sigma^2}} \tag{2.5}$$

where $\sigma = (\sigma_{WS} - \sigma_{OS})/\sigma_{WO}$ (Fig. 2.3b). The boundary conditions that arise are identical to those given by the Duprè-Young condition.

Fig. 2.3a shows the $V - E$ graph of different configurations. The $V - E$ graph for the spherical cap is calculated by minimizing (2.1) under the volume constraint using basic calculus, while the liquid bridge is calculated by solving (2.4) and (2.5) numerically using the shooting method [AP98] for a given range of H. Depending on the volume of water, the minimum energy configuration is either the spherical cap for small volumes or liquid bridge for large volumes. The transition happens where the blue dotted line and red dashed line intersect. The liquid bridge does not extend to zero volume as it requires a finite amount of water to form a bridge. Notice that we do not need to consider the case which we have multiple spherical caps. This is because the lowest energy state within the subcategory of spherical caps is the one with a single cap (Theorem 2.3.1).

2.2.2 Hollow sphere

Next, we consider a DCP shaped as in Fig. 2.2b, a larger sphere with a smaller inner sphere carved out to form an exposed cavity, which we call the hollow sphere. Assuming that the

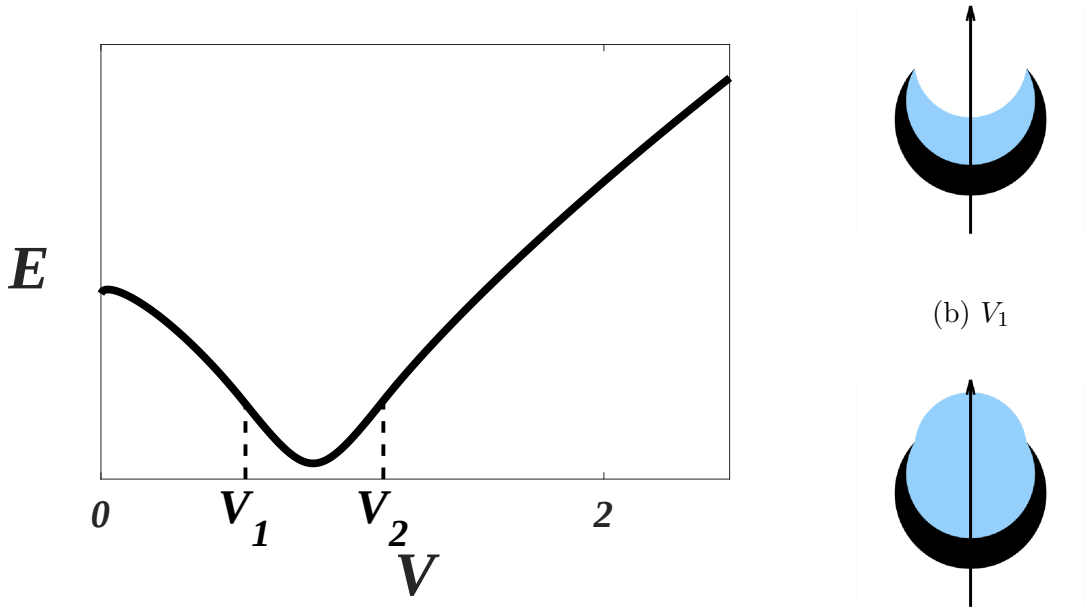

(a)

(b) V_1

(c) V_2

Figure 2.4: Hollow sphere dropicle. (a) is the $V - E$ graph of the hollow sphere DCP. The minimum is obtained when the water-oil interface is flat. (b) and (c) are cross-sections of the dropicle through the axisymmetric axis. The volume contained in each image corresponds to the volumes V_1 and V_2 indicated on the graph. The parameters of the DCP are those given in Fig. 2.2b. The unit volume is given as $V_{IS} = \frac{4}{3}\pi r^3$.

water-oil surface is axisymmetric, by Theorem 2.2.1, the shape of the minimal energy surface is a spherical cap with a curvature that can differ from those of the DCP surfaces. We can calculate the $V - E$ graph analytically following [NAM13, Bru19]. However, instead of using this analytic method, we follow a numerical method as outlined below.

1. For a given water volume and circular triple junction (contact line), there exists one spherical surface. We compute the surface energy of the entire system for this chosen contact line.

2. Fix the volume and find the contact line which minimizes the energy of the system.

3. Repeat the calculation for different volumes.

Fig. 2.4a shows the $V - E$ graph of a hollow sphere DCP with cross-section shown in Fig. 2.2b. For small volumes of water, we see a decrease in energy as the volume increases, until the water volume is large enough so that it reaches the outer edge of the hollow sphere and forms a flat surface. Two special volumes of interest are V_1, the smallest volume for which the water droplet reaches the edge of the hollow sphere, and V_2, the largest such volume. Once the water volume exceeds V_2 the energy minimizing configuration wets the outside sphere. When the contact line is away from the sharp tip, the Duprè-Young condition holds for the surface. However, for the sharp corner, the surface does not necessarily satisfy the condition.

2.2.3 Hollow cylinder

The DCP we consider in this section is an empty cylinder with a finite wall width (Fig. 2.2c), which we call a hollow cylinder. We assume that the water-oil surface is axisymmetric about the axis of the cylinder. By Theorem 2.2.1, the shape of the water-oil surface is part of a sphere. Similar to section 2.2.2, we calculate the $V - E$ graph by determining the minimum energy configuration of the top and bottom water-oil interfaces that contain the given volume (red line in Fig. 2.5a). As in Fig. 2.4a, V_1 and V_2 denote the smallest and largest volumes on which the contact line of the droplet are the edges of the inner cylinder. When the contact line is away from the edges, the Duprè-Young condition holds for the energy minimizing configuration, but not necessarily for the sharp corners.

For a sufficiently small volume, the water domain that minimizes the energy of the system (2.1) is not axisymmetric - the drop attaches to the inside wall of the cylinder. It can then be approximated by a spherical cap on a flat plane (blue line). In this thesis we assume that the cylinder is narrow enough ($r < h$ in Fig. 2.2c), so that the minimum energy configuration is axisymmetric for large enough water volumes ($V > 0.2$ in Fig. 2.5a). For such DCPs, these small volumes are not relevant to large scale systems with multiple DCPs exchanging fluid,

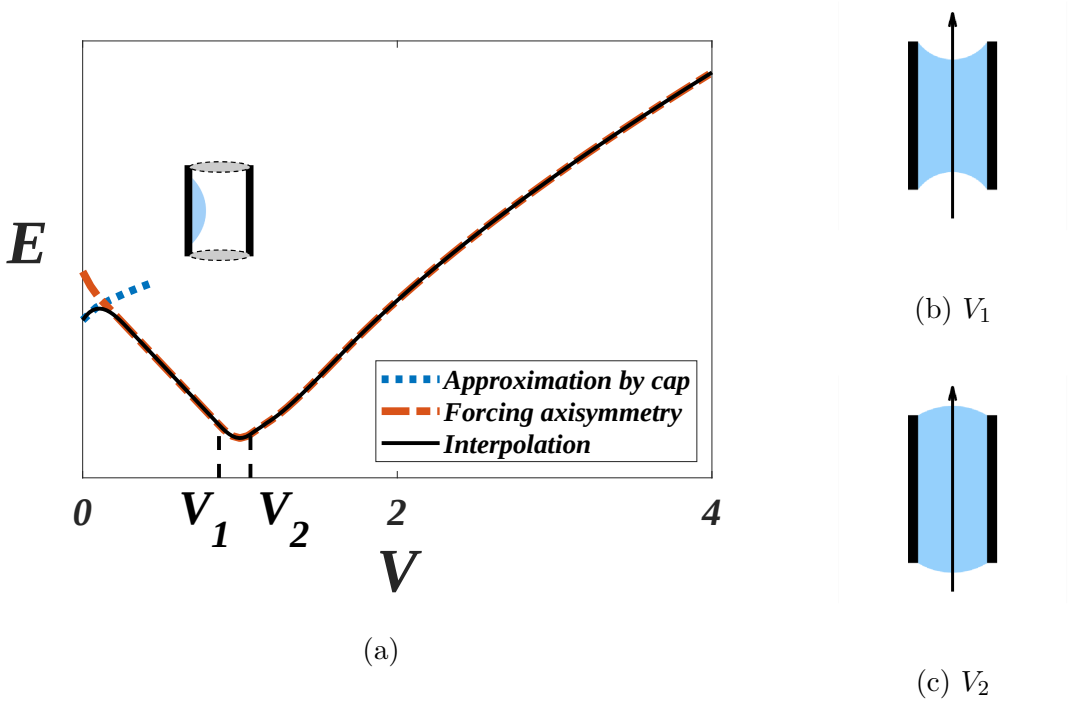

(a)

(b) V_1

(c) V_2

Figure 2.5: Hollow cylinder dropicle. (a) is the $V - E$ graph of the hollow cylinder DCP given in Fig. 2.2c. The red line represents the $V - E$ graph when axisymmetry is forced. The minimum energy is obtained when the top and bottom water-oil interfaces are flat. The blue line represents an approximation of the non-axisymmetric surface by a spherical cap and the black line is an interpolation of these two energies which is an approximation of the true $V - E$ graph. (b) and (c) are cross-sections of the dropicle through the axisymmetric axis with water volume V_1 and V_2. The unit volume is given as the volume of the inner cylinder $V_{IC} = \pi r^2 h$.

as in the following sections. For these reasons, we smooth the axisymmetric $V - E$ graph at small volumes to simplify the analysis, which requires continuity of E' with respect to E. The case of an extremely flat cylinder is addressed experimentally in [DOW20]. For such DCPs, partial filling is typically not axisymmetric, requiring careful numerical simulation of the fully 3D energy minimization problem, as was carried out in [WOW20] for another non-axisymmetric DCP shape. Finally we mention that discontinuities in E' typically result from topology changes in the minimizing configuration, when V is varied, such as in the example in Fig 2.3. The regime of interest to us for the cylinders and hollow spheres does not involve topology changes and thus can be addressed with arguments that assume continuity of E'.

2.3 Rigorous theory of energy minimizing surface

In this section, we answer how the $V - E$ graphs can be used to analyze the interactive behavior between dropicles. We develop a theory for the water distribution that minimizes energy among multiple dropicles. First we consider two identical DCPs and a fixed total volume of water. The first derivative of the graph is key in understanding how to split the water between the DCPs to achieve the energy minimum. Extending this idea we prove a theorem for systems with more than two DCPs. Throughout this thesis, we assume each dropicle contains only one DCP, i.e. no two DCPs are connected by the same water droplet. In real physical systems, sometimes one observes coalescence of these dropicles. However, this is beyond the scope of our current analysis.

2.3.1 Droplet splitting between two DCPs

For a DCP along with its $V - E$ graph, $E(V)$, we address the question of the optimal water distribution between two identical DCPs, given a fixed total water volume V_T. Does the water droplet split into two smaller drops or remain intact (Fig. 2.6)? We formulate this as

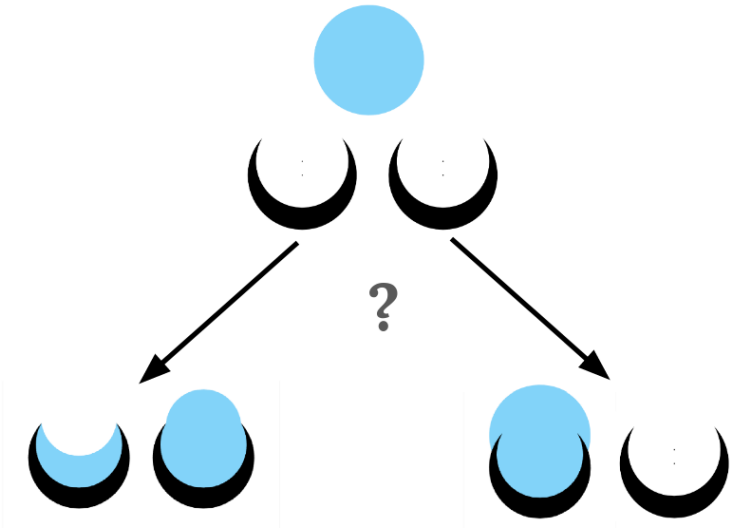

Figure 2.6: What is the optimal way to split a volume of water between two DCPs?

an optimization problem

$$\overline{V} = \underset{0 \leq V \leq V_T}{\operatorname{argmin}} \{E(V) + E(V_T - V)\}. \tag{2.6}$$

This optimization problem minimizes the sum of the static energy function $E(V)$. For this section, we only consider functions $E(V)$ that are continuously differentiable.

By the symmetry of the problem, we obtain two $\overline{V}$ for a minimum energy distribution. The smaller volume of the two, which we denote as V_S, depends on the total volume V_T and satisfies either $V_S = 0$ or

$$E'(V_S) = E'(V_T - V_S). \tag{2.7}$$

2.3.1.1 Convex and Concave $V - E$ graphs

We first note that for convex and concave $E(V)$, the result is a simple application of convexity. We state this as a theorem below.

Theorem 2.3.1. *Assume $E(V) \in \boldsymbol{C}^1[0, \infty)$. If $E(V)$ is a convex function, $V_S = V_T/2$.*

If $E(V)$ is a concave function, $V_S = 0$. If $E(V)$ is strictly convex or strictly concave, the minimizer is unique.

Proof. If $E(V)$ for $0 \leq V \leq V_T$ is a convex function the total energy function $E(V)+E(V_T-V)$ is also a convex function. The minimum of the convex function is obtained where the first derivative is 0. This is satisfied for $V_S = V_T/2$. If $E(V)$ is strictly convex this minimizer is unique.

If E is a concave function, by using concavity twice we obtain

$$E(0) + E(V_T) \leq E(V) + E(V_T - V), \tag{2.8}$$

for all $0 \leq V \leq V_T$, hence $V_S = 0$. If $E(V)$ is strictly concave the inequality is strict. □

Classical example A simple example of the concave case is an isolated water droplet in the absence of a solid phase. Since the energy minimizing configuration of a water drop in oil is a sphere, the energy graph obeys $E(V) = \sigma_{WO}(6\sqrt{\pi}V)^{2/3}$, so the graph is strictly concave. Consequently, any two spherical drops have a surface area greater than that of a single sphere with the combined volumes.

2.3.1.2 General $V - E$ graphs of DCPs

Both the hollow sphere and hollow cylinder DCPs have $V - E$ graphs with certain properties that lead to guaranteed bounds on the size of V_S. In this section we list the properties of the DCPs and prove theorems based on these properties. Our theorems require that $E(V) \in \mathbf{C}^1[0, \infty)$, which we assume for the rest of the thesis (Fig. 2.7). For the proofs, it is easier to enumerate the properties of $E'(V)$ than $E(V)$. The properties of the hollow sphere are

Property A

(P1) For some $0 < V_1 < V_2$, $E'(V)$ strictly decreases for $0 \leq V \leq V_1$, strictly increases for $V_1 \leq V \leq V_2$ and again strictly decreases for $V_2 \leq V$.

(P2) $\lim_{V \to \infty} E'(V) = 0$.

(P3) $E(V_2) - E(0) = \int_0^{V_2} E'(U)dU \leq 0$.

For such $E(V)$ the following theorem holds.

Theorem 2.3.2. *Consider two DCPs with the same $E(V)$ satisfying Property A above. For water of total volume V_T the following are true,*

1. *If $0 \leq V_T \leq V_1$, then $V_S = 0$ i.e. the other DCP contains all V_T.*
2. *The minimum energy volume of the DCP, $V_{min} := \operatorname{argmin} E(V)$, satisfies $V_1 \leq V_{min} \leq V_2$.*
3. *There exists a critical $V_b \geq V_2$, such that if $2V_b \leq V_T$, then $V_{min} \leq V_S \leq V_2$ i.e., a DCP contains a water volume in the range $[V_{min}, V_2]$. Furthermore, $V_S \to V_{min}$ as $V_T \to \infty$.*

The last result of the above theorem is important because it results in fairly uniform size volumes (between V_{min} and V_2) associated with a DCP. With many DCPs a similar result holds in which all but one DCP have a volume of water between these two bounds (cf. Fig. 2.14a). A DCP with a $V - E$ graph that yields V_1 close to V_2 and consequently V_{min} close to V_2 should trap a droplet with a specific volume between the two. This is a design feature of the DCP.

Proof. We provide Fig. 2.7a as an example of a function that satisfies the given conditions. The first result follows from Theorem 2.3.1 since $E(V)$ is concave in the range $0 \leq V \leq V_1$. For the second result, we note that since $V_{min} \neq 0$ by *(P3)*, $E'(V_{min}) = 0$ holds. Since $E'(V_1) < 0$ by *(P1)* and *(P3)*, and $E'(V_2) > 0$ by *(P1)* and *(P2)*, there are at most two V that satisfy $E'(V) = 0$, one smaller than V_1 and the other between V_1 and V_2. It is straight forward to show that V_{min} is the latter.

The last result is proved as follows. Recall that V_S should satisfy (2.7) or either equal to 0. For $V_T \geq 2V_2$, property *(P1)* leads to $E'(V_T - V) > 0$, for $V < V_T/2$. For such total volumes, these two facts and *(P1)* restrict the possible values of V_S to $0, V_\alpha, V_\beta,$ and $V_T/2$, where $0 < V_\alpha < V_1 < V_{min} \leq V_\beta \leq V_2$. Note that

$$E'(V_i) > 0 \text{ for } V_i = V_\alpha, V_\beta, \text{ and } V_T/2.$$

We show that $V_S = V_\beta$, provided that $V_T \geq 2V_b$ for some V_b.

1) Compare $V = 0$ and $V_{min} \leq V_\beta \leq V_2$:

   We show that

$$E(V_T) + E(0) - [E(V_T - V_\beta) + E(V_\beta)] \geq 0$$

   for any $V_{min} \leq V_\beta \leq V_2$ that satisfies (2.7). Notice that the left-hand side of the inequality is identical to the left-hand side of the following inequality,

$$\int_{V_T - V_\beta}^{V_T} E'(U)dU - \int_0^{V_\beta} E'(U)dU \geq -\int_0^{V_\beta} E'(U)dU.$$

   The above inequality holds since $E'(V) > 0$ for $V > V_2$. By combining $E'(V_\beta) > 0$ and *(P1)*, $E'(V) > 0$, for $V_\beta < V < V_2$. Together with *(P3)*,

$$-\int_0^{V_\beta} E'(U)dU \geq -\int_0^{V_2} E'(U)dU \geq 0. \tag{2.9}$$

2) Compare $0 < V_\alpha < V_1$ and $V_{min} \leq V_\beta \leq V_2$:

   Following the steps of the previous comparison, it is sufficient to show

$$-\int_{V_\alpha}^{V_\beta} E'(U)dU \geq 0.$$

   From $E'(V_\alpha) > 0$ and *(P1)*, $E'(V) > 0$ for $0 < V < V_\alpha$. Similar to (2.9), we deduce

$$-\int_{V_\alpha}^{V_\beta} E'(U)dU \geq -\int_0^{V_2} E'(U)dU \geq 0.$$

3) Compare $V = V_T/2$ and $V_{min} \leq V_\beta \leq V_2$: [1]

Again we want to show

$$-\int_{V_T/2}^{V_T-V_\beta} E'(U)dU + \int_{V_\beta}^{V_T/2} E'(U)dU \geq 0.$$

Note that by *(P1)*

$$-\int_{V_T/2}^{V_T-V_\beta} E'(U)dU \geq -\int_{V_T/2}^{V_T-V_\beta} E'(V_T/2)dU = -\int_{V_\beta}^{V_T/2} E'(V_T/2)dU.$$

Therefore, showing

$$\int_{V_\beta}^{V_T/2} E'(U) - E'(V_T/2)dU \geq 0$$

is sufficient. We now choose a V_b. By *(P1)* and *(P2)*, there exists a one to one correspondence between $V_{min} \leq W \leq V_2$ and $V_2 \leq V$ which satisfies $E'(W) = E'(V)$. We denote such W for V as $W(V)$. Note that, by $E'(V_{min}) = 0$, $W(V) \to V_{min}$ as $V \to \infty$. We choose a V_b that $W_b := W(V_b)$ satisfies

$$\int_{V_{min}}^{W_b} E'(V_b)dU \leq \int_{W_b}^{V_b} E'(U) - E'(V_b)dU. \tag{2.10}$$

The left-hand side and the right-hand side of the above inequality are represented as colored areas in Fig. 2.7a. Note that such V_b exists, since as $V_b \to \infty$, the left-hand side goes to 0, while the right-hand side increases from a positive value.

For $V_T \geq 2V_b$, $V_\beta \leq W_b \leq V_T/2$ holds and

$$\begin{aligned}
&\int_{V_\beta}^{V_T/2} E'(U) - E'(V_T/2)dU \\
&\geq \int_{V_\beta}^{W_b} E'(U) - E'(V_b)dU + \int_{W_b}^{V_T/2} E'(U) - E'(V_T/2)dU \\
&\geq -\int_{V_\beta}^{W_b} E'(V_b)dU + \int_{W_b}^{V_b} E'(U) - E'(V_T/2)dU \\
&\geq -\int_{V_{min}}^{W_b} E'(V_b)dU + \int_{W_b}^{V_b} E'(U) - E'(V_b)dU \geq 0.
\end{aligned}$$

[1] While preparing the defense of the thesis, I have noticed that there is a simple way to show that $V = V_T/2$ is not a minimizer. This is achieved by Theorem 2.3.4 and the fact that the neighborhood of $V = V_T/2$ is concave. This also improves the result of the theorem as $V_b = V_2$. An analogous improvement is possible on Theorem 2.3.3.

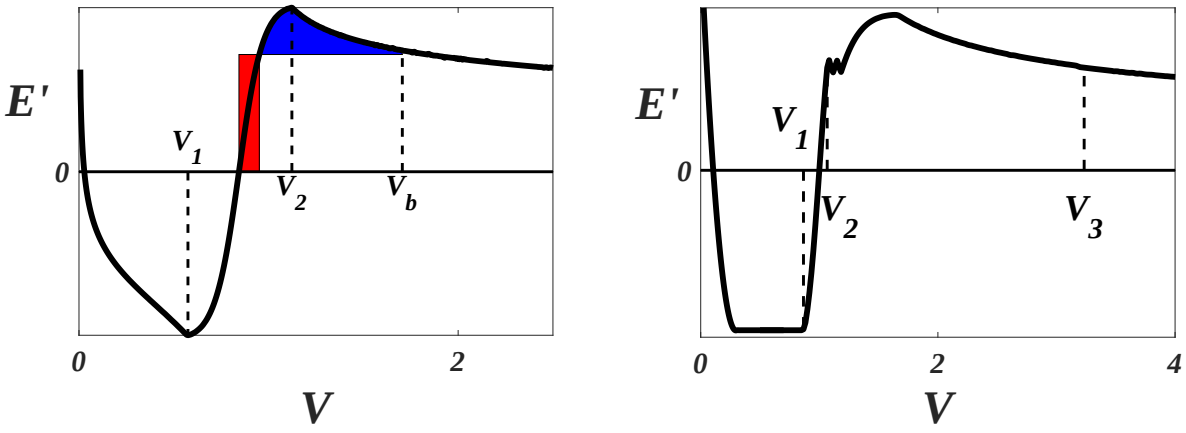

(a) $V - E'$ graph of hollow sphere

(b) $V - E'$ graph of hollow cylinder

Figure 2.7: $V - E'$ graph of the hollow sphere and hollow cylinder (Fig. 2.4 and 2.5). In (a), V_b is chosen so that (2.10) is satisfied. The area in light red and dark blue represents the value of the left- and right-hand side of (2.10) respectively. In (b) V_3 is chosen to correspond to Theorem 2.3.3.

The first and third inequality holds since $0 \leq E'(V_T/2) < E'(V_b)$. The second inequality holds since, $E'(V) \geq 0$ for $V_\beta \leq V \leq W_b$, and $E'(V) \geq E'(V_T/2)$ for $V_b \leq V \leq V_T/2$. The last inequality comes directly from (2.10). Since V_β satisfies $V_\beta = W(V_T - V_\beta)$, $V_\beta \to V_{min}$ as $V_T \to \infty$.

□

Remark 1.

1. *For the case of the $V - E$ graph of a dropicle, as the volume increases, the water-oil surface asymptotes to a sphere and the effect of the DCP on the surface energy becomes negligible. Therefore the (P2) of the theorem*

$$\lim_{V\to\infty} E'(V) \approx \lim_{V\to\infty} CV^{-1/3} = 0$$

is justified.

2. *The proof demonstrates a tighter bound $V_{min} \leq V_S \leq W_b$ regarding the last statement of the theorem.*

3. *We notice from the proof that V_b is small if $E'(V)$ increases rapidly between V_{min} and V_2. This condition has the added benefit that the range $[V_{min}, V_2]$ is small.*

Application to the hollow sphere The $V - E'$ graph of the hollow sphere is given in Fig. 2.7a with the values of V_1, V_2, and V_b. Theorem 2.3.2 predicts that when two hollow spheres and a large volume of water are present the energy minimizing distribution is one of the DCPs containing water of volume between V_{min} and V_2, and the other containing the rest. Note that the water-oil interfaces of both DCPs should have the same radius of curvature. This is due to the constant mean curvature condition of minimum energy surfaces (Section 2.2).

For the hollow cylinder, we relax the (P1) of Property A to

(P1′) There exists $0 < V_1 < V_2 < V_3$ so that $E'(V)$ decreases for $0 \leq V \leq V_1$, strictly increases for $V_1 \leq V \leq V_2$ and strictly decreases for $V_3 \leq V$. Also $E'(V) > 0$ for all $V > V_2$.

Based on this assumption, we prove a theorem with identical results.

Theorem 2.3.3. *If $E(V) \in \boldsymbol{C}^1[0, \infty)$ satisfy the conditions above, then the same conclusions of Theorem 2.3.2 hold.*

Proof. We provide Fig. 2.7b as an example of a function that satisfies the conditions of the theorem. Most parts of the proof are similar to that of Theorem 2.3.2. Only the last conclusion needs to be modified. We assume that V_3, satisfies $E'(V_3) < E'(V)$ for all $V_2 < V < V_3$. This is possible since, without loss of generality, we can choose a larger V_3 that has this property, by *(P1′)* and *(P2)*. Then for $V_T > 2V_3$, the possible values of V_S are the analogous

$0, V_\alpha, V_\beta,$ and $V_T/2$ in the previous proof. The comparisons between the possible values are similar except for the comparison between V_β and $V_T/2$, which we present below.

As in the previous proof we want to show

$$\int_{V_\beta}^{V_T/2} E'(U) - E'(V_T/2)dU \geq 0$$

for $V_T > 2V_b$, for some V_b. Again for $V \geq V_3$ there is a function $W(V)$ such that $V_{min} \leq W \leq V_2$ and $E'(W) = E'(V)$. We choose a $V_b \geq V_3$, so that the $W_b := W(V_b)$ satisfies

$$\int_{V_{min}}^{W_b} E'(V_b)dU \leq \int_{W_b}^{V_b} E'(U) - E'(V_b)dU. \tag{2.11}$$

Such V_b exists since as $V_b \to \infty$ the left-hand side goes to 0 by $W_b \to V_{min}$, while the right-hand side increases from a positive number by $E'(V) > E'(V_b)$ for $W_b < V < V_b$. The rest of the proof is similar. □

Application to the hollow cylinder Differentiating the $V - E$ graph of the hollow cylinder (Fig. 2.7b) shows Theorem 2.3.3 is applicable. If there are two such DCPs and a large enough volume of water, the energy minimum is obtained when a volume between V_{min} and V_2 is trapped in one of the DCPs. We note that the figure has four critical points for volumes near V_2, due to the hollow cylinder having a wall of finite width as explained in the next paragraph.

Fig. 2.8 shows an enlarged figure with the critical points labeled. As the volume captured by the DCP increases from 1 to A both top and bottom oil-water interfaces bulge symmetrically. However, for volumes between A and B, this symmetric configuration is no longer the energy minimum. Rather, the minimum configuration is asymmetric - on one side (the bottom side in the figure) the contact line lies between the outer and inner edges and on the other side (the top side) it is fixed on the inner edge. The contact line on the bottom reaches the outer edge for volume B. As the volume increases further till C, the contact lines are fixed again while the water-oil interfaces bulge out. Between volume C and D, the

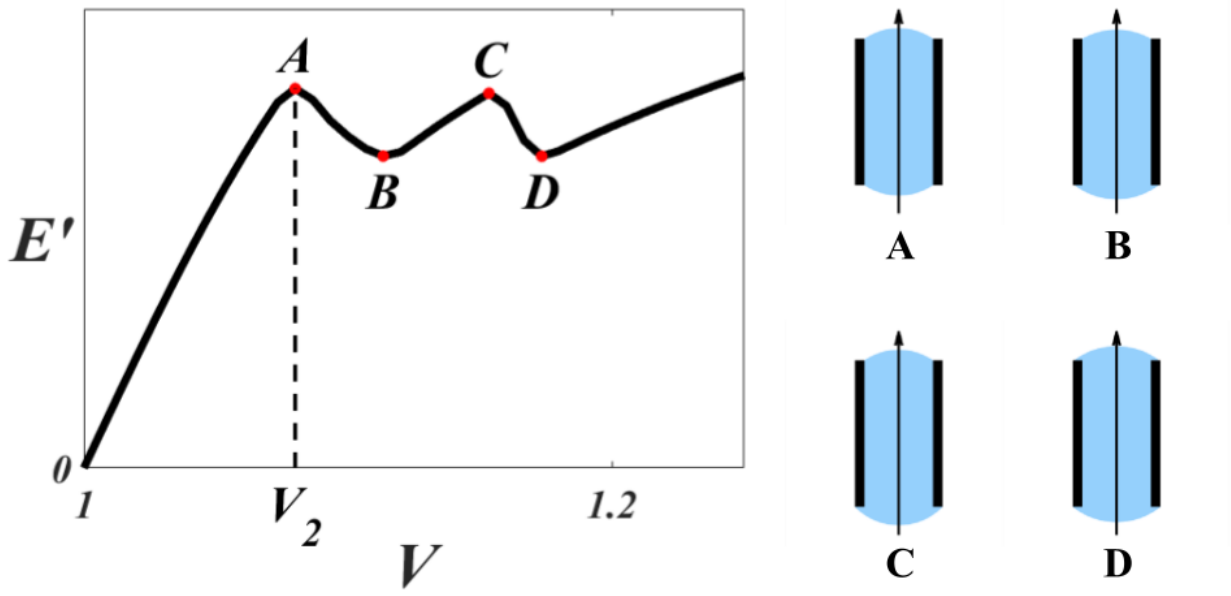

Figure 2.8: An enlarged graph of Fig. 2.7b and cross section configurations at each critical point.

top contact line moves to the outer edge. Once both contact lines are on the outer edge (volume D) the two interfaces bulge symmetrically as the volume increases until the next critical point. For volumes larger than the critical point at $V \approx 1.7$ (Fig. 2.7b), the symmetry breaks once more, with a large sphere on one side and a smaller sphere on the other side. We note that this phenomenon is similar to the configuration of droplets deposited on an orifice [HN19]. However, we emphasize that for a given volume the radius of curvature of the two water-oil interfaces are the same.

2.3.2 Droplet splitting between many DCPs

In physical applications there are many DCPs in the system (Fig. 1.1). The minimum energy distribution of such system is the solution to the optimization problem

$$\overline{\mathbf{V}} = \underset{\substack{\Sigma V_i = V_T \\ V_i \geq 0}}{\operatorname{argmin}} \{\Sigma E(V_i)\}, \tag{2.12}$$

where $\overline{\mathbf{V}}$ is a vector with N entries representing N number of DCPs and V_i being the water volume in i-th DCP. Again the key is the concave and convex properties of $E(V)$.

Theorem 2.3.4. *For an energy function $E(V)$ and $0 < a < b$, the minimizer $\overline{\boldsymbol{V}}$ of (2.12) has the following properties.*

1. *If $E(V)$ is strictly concave on (a, b), then at most one of the entries of $\overline{\boldsymbol{V}}$ is in (a, b).*
2. *If $E(V)$ is strictly convex on $[a, b]$, then all the entries of $\overline{\boldsymbol{V}}$ on the domain $[a, b]$ are equal.*

Proof. 1. Suppose not, i.e. there are two entries of $\overline{\mathbf{V}}$, $V_i \leq V_j$, that lie in (a, b). Then

$$E(V_i) + E(V_j) > E(V_i - \epsilon) + E(V_j + \epsilon)$$

for small enough ϵ. This contradicts that $\overline{\mathbf{V}}$ is the minimizer

2. Suppose not, i.e. there are two entries of $\overline{\mathbf{V}}$, $V_i < V_j$, which lie in $[a, b]$. Then

$$E(V_i) + E(V_j) > E(V_i + \epsilon) + E(V_j - \epsilon)$$

for small enough ϵ. This contradicts that $\overline{\mathbf{V}}$ is the minimizer

□

For the hollow sphere, the value of the distribution $\overline{\mathbf{V}}$ is proved rigorously, for sufficiently large total volume V_T.

Theorem 2.3.5. *If $E(V)$ satisfy Property A and $V_T \geq NV_b$, then $N-1$ entries of $\overline{\boldsymbol{V}}$ are between V_{min} and V_2.*

Proof. By Theorem 2.3.4 (a) there is at most one entry of $\overline{\mathbf{V}}$ in the interval $(0, V_1)$ and likewise in (V_2, ∞); we denote these values as V_α and V_γ; (b) the entries in $[V_1, V_2]$ are equal which we denote as V_β; (c) the only other possible entry is 0. We show that V_β and V_γ are the only allowed values. By the total volume constraint there is an entry V_γ, since otherwise, all the entries of $\overline{\mathbf{V}}$ are less than V_b, and consequently $V_T < NV_b$.

Suppose that entry i and j of $\overline{\mathbf{V}}$ are 0 and V_γ respectively. Then $V_i + V_j = V_\gamma > 2V_b$, by a total volume argument similar to above. Applying Theorem 2.3.2 to the two-DCP system with DCP i and j shows that the distribution is not a minimum energy distribution. Therefore $\overline{\mathbf{V}}$ does not have any entries with value 0. The same argument applies to V_α. The fact that $V_{\min} \leq V_\beta \leq V_2$ follows from theorem 2.3.2 applied to V_β and V_γ. □

The theorems assure that the lowest energy state has all but one of the dropicles containing the same volume of water V_β. This minimizing volume occurs in the region where $E(v)$ is convex. This is numerically demonstrated in Section 2.4.3.

Note that in this section, we do not assume any geometric properties of the DCP other than the properties of the DCP's $V-E$ graph. Therefore the theorems not only hold for axisymmetric DCPs in section 2.2 but also for any DCP with the appropriate properties [WOW20].

2.4 Numerical simulations

In this section, we simulate pairwise interactions of a multi-DCP system, in which fluid can be exchanged in a pairwise fashion to minimize the pairwise surface energy. The method randomly chooses two DCPs, each with their own fluid volume, and redistributes the volume between the DCPs so as to minimize the surface energy of that two-DCP system. This

process is repeated until the ensemble reaches a steady state.

First, we simulate the minimum energy distribution for two DCPs as a function of the total fluid volume. These simulations result in graphs that show how the fluid is distributed. These results are consistent with the rigorous theory from the previous section. In [WOW20], actual dynamic splitting experiments are done in the laboratory showing that the theoretical results are a reasonable approximation. However dynamic splitting is known to sometimes lead to local energy minima rather than the global minimizer.

2.4.1 Simulation of a two-DCP system

First, we consider the interaction of two identical DCPs. This corresponds to solving the optimization problem in section 2.3, which we restate here

$$V_S = \underset{0 \le V \le V_T/2}{\operatorname{argmin}} \{E(V) + E(V_T - V)\}. \tag{2.13}$$

Once we specify $E(V)$, we can calculate $E(V) + E(V_T - V)$ for any given total volume V_T and find V_S. We plot V_S, as V_T varies, which we call the splitting graph. The splitting graphs of the hollow sphere and the hollow cylinder are shown in Fig. 2.9.

Fig. 2.9a is the splitting graph of the hollow sphere (whose energy curve is plotted in Fig. 2.4a). For small V_T, $V_S = 0$, while for large V_T, $V_{min} \le V_S \le V_2$, which agrees with Theorem 2.3.2. Note that the theorem does not provide a prediction in the intermediate range (the domain that the droplets split evenly) which is straightforward to compute numerically. Fig. 2.9b is the splitting graph of the hollow cylinder (whose energy curve is plotted in Fig. 2.5a). Similar to the results of Fig. 2.9a the splitting graph agrees with Theorem 2.3.3.

The simulated splitting graph is compared to macroscale experiments (methods in the next chapter). The experiments use a hollow sphere and hollow cylinder DCP about 10mm in diameter, with densities of the fluids closely matched. The DCPs are initially close together sharing the same aqueous volume. They are slowly pulled apart to minimize the effect of dynamics. To plot the splitting graph we need the surface tension of the DCP. This is

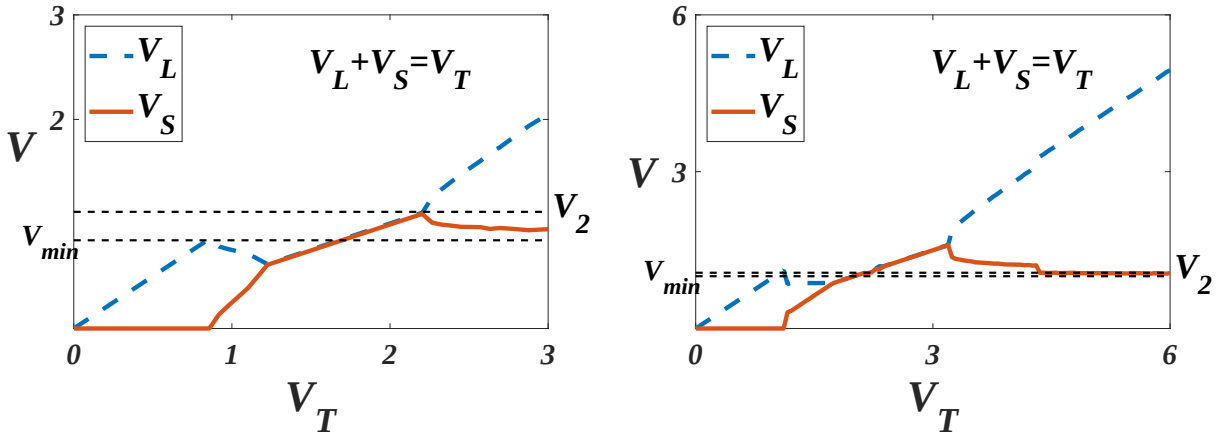

(a) Hollow sphere

(b) Hollow cylinder

Figure 2.9: Optimal splitting volume V_S of (2.13) with respect to V_T. (a) and (b) are the hollow spheres and hollow cylinders $V - E$ graph respectively (Fig. 2.4a and 2.5a). V_L and V_S indicate the larger and smaller volume of the droplets ($V_L = V_T - V_S$), while the dotted horizontal lines V_{min} and V_2 correspond to the volumes in theorems 2.3.2 and 2.3.3. The unit volumes are V_{IS} and V_{IC} respectively.

achieved by measuring the contact angle and using (2.3). The results are shown in Fig. 2.10 which the theoretical splitting graph and the experiment results agree considerably.

In Fig. 2.9, the hollow cylinder has a more complicated splitting graph. For example, V_S of the hollow sphere never exceeds V_2, while the hollow cylinder does. Also, the minimum V_T required to guarantee $V_{min} < V_S < V_2$ is smaller for the hollow sphere than the hollow cylinder. These properties are due to the finite thickness of the cylinder wall (see Appendix). Since the hollow sphere's splitting graph is simple, we focus on them in subsequent simulations.

2.4.2 Different geometries and surface tensions

In this section, we calculate the splitting graphs of the hollow sphere for different geometries and surface tensions. So far our computations are based on a specific shape of a hollow sphere

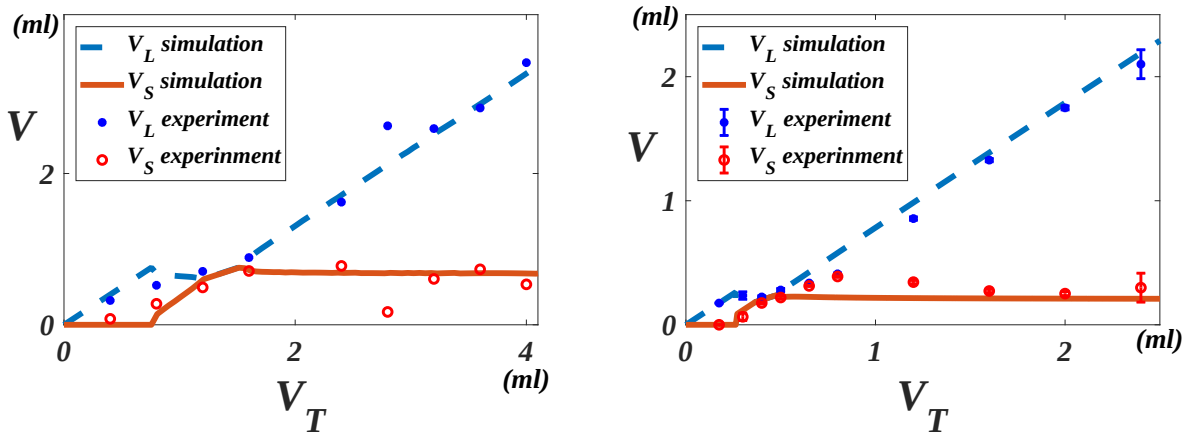

(a) Hollow sphere

(b) Hollow cylinder

Figure 2.10: Splitting graphs of the experiments and simulations (the experiments are detailed in Chapter 3). V_L and V_S indicate the larger and smaller volume of the droplets. The lines correspond to the simulations and the dots correspond to the experimental data. Each dot indicates (a) one trial or (b) three trials, and the error bars correspond to one standard deviation of the data. The surface tensions for these graphs are matched to the materials in the experiments and therefore differ from the graphs in Fig. 2.9.

DCP with fixed surface tension values. In this case, the splitting graph has two properties, (a) for small total volumes there is only one DCP that contains water and (b) for large total volumes there is a volume range that one DCP contains an amount of water volume within that range. We show that such results are robust in the sense that for a range of geometries and surface tensions the DCPs still possess these properties.

Fig. 2.11 shows the splitting graphs for spherical dropicles for three different geometries. The splitting graphs have the key features stated above. We also observe a trend that the difference between V_{min} and V_2 decreases as the opening of the DCP becomes smaller. This suggests that it may be desirable to have a hollow sphere with a small opening to create more uniform volumes amongst a set of DCPs. However, practically if the opening is too small, it might be difficult for the fluid to exchange readily and the tip of the DCP might be fragile.

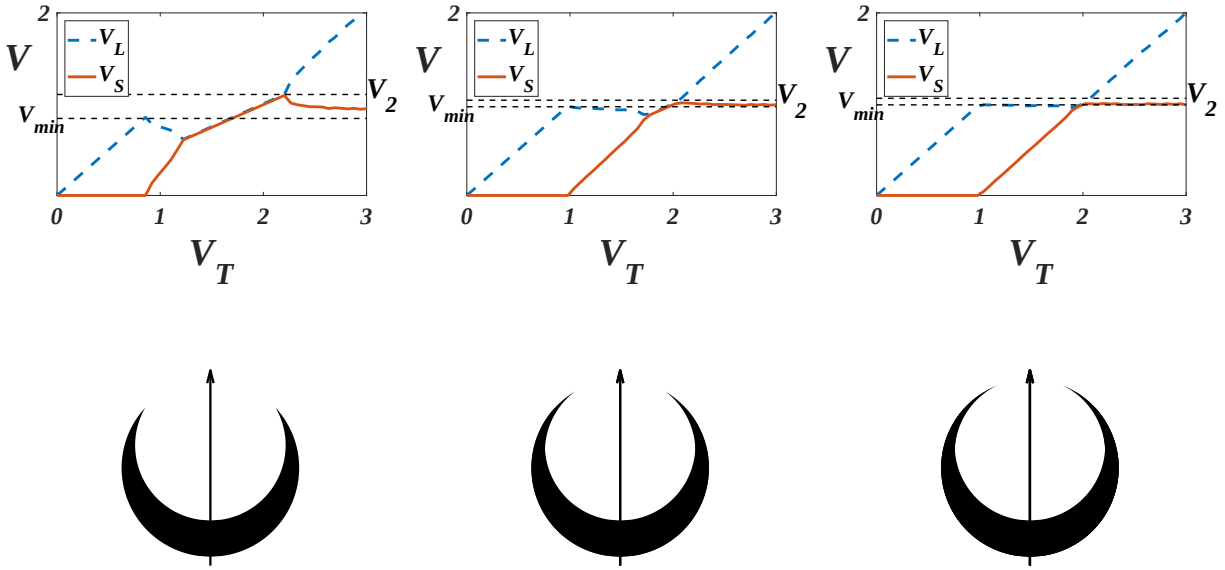

(a) (b) (c)

Figure 2.11: Splitting graphs (top row) of various hollow sphere shapes (bottom row). The shape is chosen so that r and R are fixed and d is 0.5, 0.8 and 0.9 for (a),(b) and (c) respectively (Fig. 2.2b). The unit volume is V_{IS}.

Fig. 2.12 shows the splitting graphs as we change the surface tension between oil and solid, σ_{OS}, within the range of partial wetting. Such changes have almost no effect on the splitting graph, compared to the changes in the shape of the DCP. This indicates that experiments are expected to behave similarly for a range of solid and fluid materials with different surface tensions.

2.4.3 Simulations of a multi-DCP systems

For the multi-DCP case we need to solve the optimization problem (2.12) which we restate here,

$$\overline{\mathbf{V}} = \underset{\substack{\Sigma V_i = V_T \\ V_i \geq 0}}{\operatorname{argmin}} \{\Sigma E(V_i)\}. \tag{2.14}$$

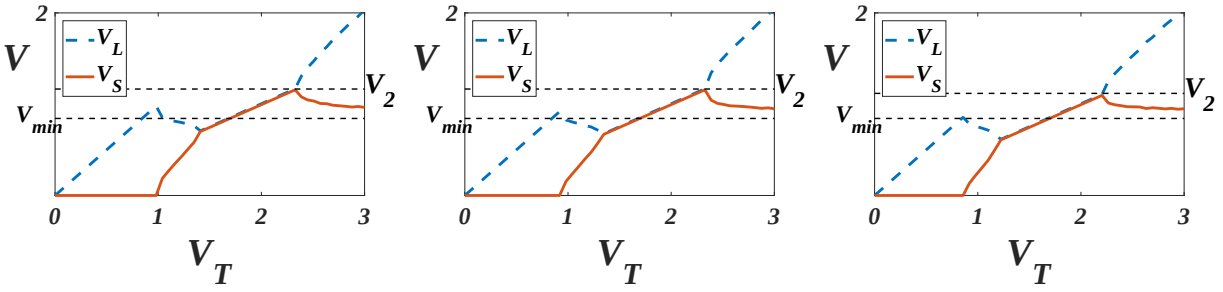

(a) σ_{OS}=0.5 (b) σ_{OS}=0.7 (c) σ_{OS}=0.9

Figure 2.12: Splitting graphs of hollow spheres with different surface tensions. Each graph has a different value of σ_{OS}, the oil-solid surface tension, which are 0.5, 0.7 and 0.9 for (a),(b) and (c) respectively. The other surface tensions are fixed as $\sigma_{WS} = 0.1$ and $\sigma_{WO} = 1$. The shape of the DCP is that of Fig. 2.11a and the unit volume is V_{IS}.

If $E(V)$ satisfies property A, we predict that all except one of the nonzero entries of $\overline{\mathbf{V}}$ have the same volume, as long as we start with sufficiently large total volume. Here we show numerically that this lowest energy state is achieved by repeated random pairwise interactions, outlined below.

Randomized procedure

1. Initialize volume vector $\mathbf{V}$ so that $V_1 = V_T$ and $V_k = 0$ for $k \geq 2$.
2. Repeat the following until a final distribution of $\mathbf{V}_F$ is obtained.
   (a) Choose DCPs i and j at random and solve the two DCP optimization (2.13), for $V_T = V_i + V_j$.
   (b) Update $V_i = V_S$ and $V_j = V_T - V_S$.

This independent randomized interaction (IRIs) is the simplest model to imitate the exchanging of fluid between dropicles colliding at random during an agitation process that

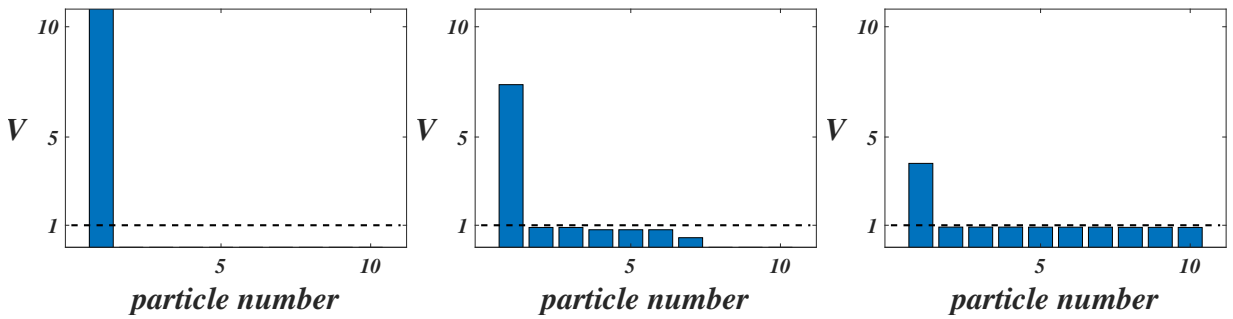

(a) Initial stage (b) Intermediate stage (c) Final stage

Figure 2.13: The volume in each of the 10 hollow sphere DCPs (Fig.2.4) as they interact according to the randomized procedure. (a) is the initial distribution. (b) shows the result after 100 interactions. (c) shows the end state after 1000 interactions. The unit volume is V_{IS}.

leads to emulsification. The detailed statistical mechanics of this problem is further studied in the next chapter. For the geometries considered here, exclusively pairwise interactions are reasonable since not many dropicles can interact simultaneously with any other dropicle at a given time.

Fig. 2.13 shows how the distribution changes as we increase the number of IRIs. The volume that was initially attached to one DCP distributes to other DCPs as they interact. Once the system reaches state Fig. 2.13c the minimum energy distribution is achieved (Theorem 2.3.5) and any additional interaction of the dropicles does not change the final distribution (Chapter 3). During the simulation, the water-oil interfaces of the dropicles do not need to have the same radius of curvature. However once the final distribution $\mathbf{V}_F$ is achieved, the radius of curvature is identical among the dropicles.

The final distributions $\mathbf{V}_F$ of a 20 DCP system are shown in Fig. 2.14a. The colors of the histogram represent simulations of total volumes $20 * 0.6$ and $20 * 1.2$, respectively. For the smaller total volume (blue), the non-empty dropicles each contain equal volume of water. For the larger total volume (orange), there is one dropicle with an excess amount of water

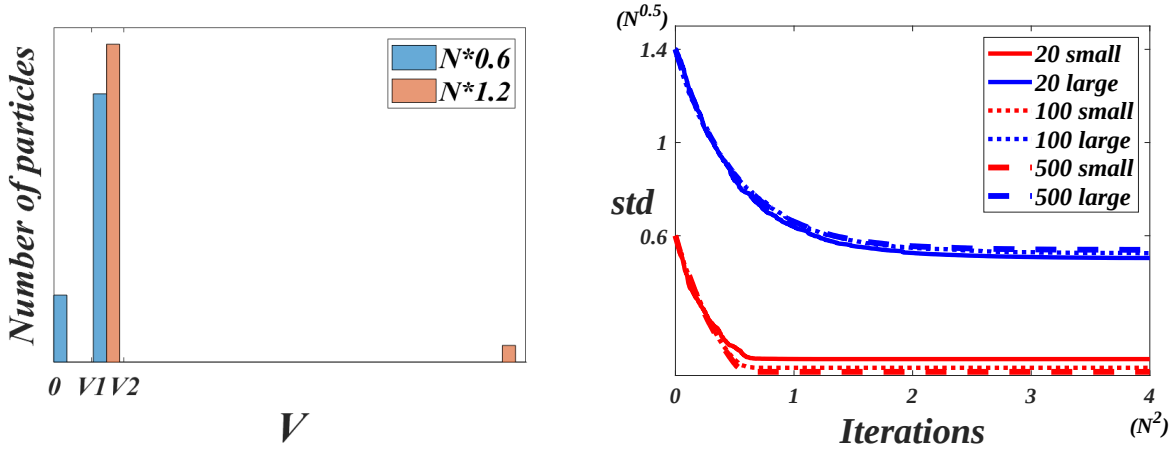

(a) (b)

Figure 2.14: Simulation results on multiple hollow sphere DCPs (Fig.2.4). (a) is a histogram of the final distribution of a 20 spherical DCP system. The total volumes of the blue and orange distribution are $0.6N$ and $1.2N$ respectively, where N is the number of DCPs. (b) plots the standard deviation of the volume vector $\mathbf{V}$ with respect to the number of IRIs. The red and blue lines correspond to the total volume of $0.6N$ (small) and $1.4N$ (large) respectively, where $N = 20, 100,$ and 500. Each line is the mean of 20 simulations. The number of IRIs is normalized by N^2, and the standard deviation is normalized by $V_{IS}\sqrt{N}$.

while all the other dropicles contain equal volume. These results agree with Theorems 2.3.4 and 2.3.5.

Another question that the randomized procedure raises is how many IRIs are needed to achieve $\mathbf{V}_F$. In physical experiments, this corresponds to how much mixing is needed to distribute the water between all the DCPs. We numerically calculate the standard deviation of $\mathbf{V}$ as we increase the number IRIs for different number of DCPs N and total volumes $0.6N$ and $1.4N$ (Fig. 2.14b). We observe a decreasing trend and that it flattens out once $\mathbf{V} = \mathbf{V}_F$. Note that for systems with total volume $1.4N$, more number of IRIs are required to achieve a final distribution. This is because the system with total volume $0.6N$ needs to fill fewer DCPs compared to that with a total volume $1.4N$. Also, notice that the curves

with different numbers of DCPs overlap for total volume of $0.6N$ and $1.4N$. This indicates that there is a general trend that determines the number of IRIs.

CHAPTER 3

Statistical energy minimization theory for systems of drop-carrier particles

This chapter is based on [DLN21] (Reprinted manuscript with permission from [DLN21] as follows: Ryan Shijie Du et al., Physical Review E, 104, 015109 and 2021 Copyright (2021) by the American Physical Society. http://dx.doi.org/10.1103/PhysRevE.104.015109).

3.1 Introduction

In this chapter, we numerically model two DCP geometries, axisymmetric hollow spheres and hollow cylinders as seen in Figure 3.1a and Figure 3.1b. Based on the previous chapter, in this chapter we (a) perform physical experiments of two DCPs splitting and compare the results with the numerical results, (b) provide a statistical theory for the random pairwise interaction model and use this to calculate the probability density function (PDF) of the required interactions to achieve uniform distribution, and (c) based on the works of (b) develop a measure that calculates the performance of a DCP and propose the best DCP. We also consider the case when there are two DCPs with different sizes and show that this significantly reduces the number of interactions required to arrive at a uniform state.

In Section 3.2, we investigate the fluid-filling behavior of single DCPs, followed in Section 3.3 by a study of interactions between two DCPs, which is compared with physical macro-scale experiments. We extend the two-DCP study to include interactions between two different (heterogeneous) sized DCPs. In Section 3.4, we build upon the two-DCP model to develop

a theory of multi-DCP systems that are either homogeneous or heterogeneous. We use a mixture model [MLR19] to derive the probability density function (PDF) for the number of Independent Random Interactions (IRIs) required for all DCPs to contain a uniform volume of target solution. Finally, in Section 3.5, we present a parametric study of DCP geometries searching for an optimal DCP for applications.

3.2 Minimum Energy Theory for an Axisymmetric Particle

In this section, we review the minimal energy theory to model the behavior of a target fluid captured by single axisymmetric DCP. We focus on the hollow sphere and hollow cylindrical DCPs as shown in Figure 3.1a and Figure 3.1b, and we take the target fluid to be water and the surrounding fluid to be oil.

We determine the equilibrium configuration for a DCP with a specified water volume by solving the corresponding energy minimization problem for surface configurations with volume constraints (Figure 3.1c) detailed in Chapter 2. The surface energy E of a three phase DCP-water-oil system is

$$E = \sigma_{\text{wo}} A_{\text{wo}} + \sigma_{\text{wp}} A_{\text{wp}} + \sigma_{\text{op}} A_{\text{op}} \tag{3.1}$$

where A_{wo} is the surface area of the water-oil interface, A_{wp} that of the water-DCP interface, and A_{op} that of the oil-DCP interface. σ's correspond to the interfacial energies per area. Our DCPs have surface components that are either hydrophilic or hydrophobic, therefore the corresponding surface energy has additional terms analogous to (3.1). Our model assumes that the buoyancy effects are negligible, and surface tensions dominate, consistent with on the microscale.

For an axisymmetric DCP, the minimal surface configuration is comprised of partial spheres with a contact angle that satisfies the Young-Dupré equation on smooth surfaces [BS15, MBK87]. If the DCP has two openings (e.g.: cylinder), the two spheres share the same radius. This fact reduces the scope of the numerical search for minimal energy configurations.

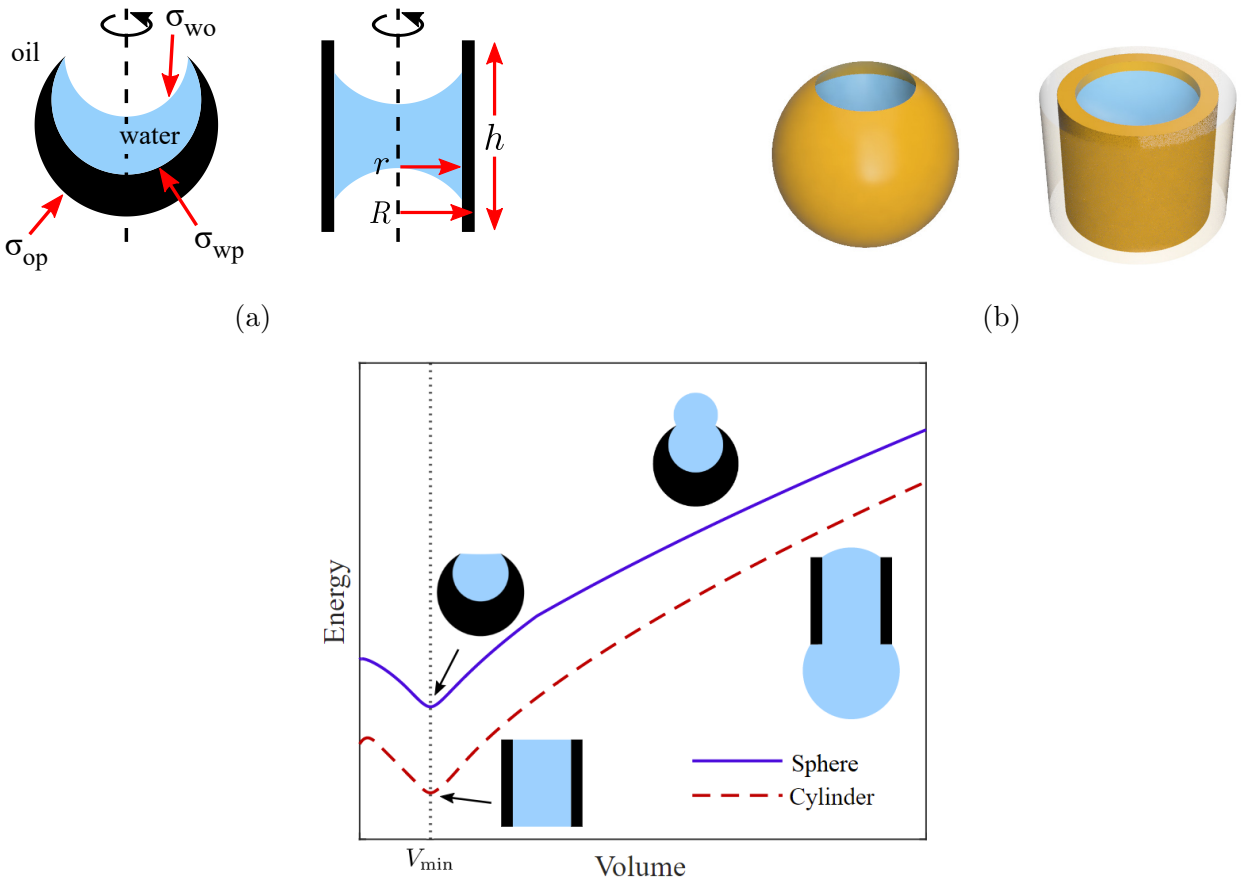

Figure 3.1: Basic parameters and behavior of axisymmetric hollow sphere and cylindrical DCPs. (a) Cross section of a hollow sphere and a cylindrical DCPs. The blue represents the water phase, black the DCP, and white the surrounding oil. The σ's are interfacial energies per area for each interface, and the cylinder is labelled with geometry parameters. (b) The full hollow sphere and cylindrical DCP. The experimental cylinder has two layers, one hydrophilic layer (yellow) and one hydrophobic layer (clear). (c) The corresponding Energy-Volume graph for a cylinder and hollow sphere DCP. The offset between the two curves is artificially added for illustration.

The theoretical properties of the energy-volume $E-V$ graph have been extensively studied in the previous chapter. For example, the energy minimum occurs when the oil-water surface is

flat (see Figure 3.1(c)). hollow sphere and cylindrical DCPs can be efficiently fabricated at the micro-scale and are simple to model computationally. The hollow sphere DCPs are introduced in [RDA22] - they are called crescent particles in [RDA22]. They are hydrophilic spherical DCPs with a smaller offset sphere removed, creating a fishbowl shape as shown in Figure 3.1a. The hollow sphere geometry has three parameters: the radius of the inner carved-out sphere, the opening aperture, and the outer radius of the DCP. The hollow cylindrical DCPs are introduced in [DOW20]. They are hydrophilic inside and on the ends while the outer surface is hydrophobic. The geometry has three parameters: the inner radius r, the outer radius R, and the height h (see Figure 3.1b). Though the physical cylindrical DCPs have certain thickness of both the hydrophilic and hydrophobic layers [DOW20] (Figure 3.1b), the thickness of the hydrophobic layer has minimal effect on the exterior wetting and is neglected in the model.

3.3 Two-Particle Interaction

In this section we experimentally measure the exchange of fluid between two DCPs and compare the results with theoretical energy minima for a two-DCP system. From the energy volume graph in Figure 3.1 one can derive a solution to the energy minimization problem of a two-DCP system

$$\min_{0 \leq V \leq V_T} \{E_1(V) + E_2(V_T - V)\} \tag{3.2}$$

for a fixed total volume V_T. Here the total energy is composed of the energy of the first DCP with volume V, $E_1(V)$, and the energy of the second DCP, $E_2(V_T - V)$. This provides a theoretical prediction to compare with experiments, which we perform on a macro-scale to accurately measure the volume V and $V_T - V$. We use cylindrical DCPs as they are easier to fabricate and sturdier to work on the macro-scale. We conduct experiments on DCPs of equal size and shape as well as experiments with different sizes (Figure 3.3). We denote these plots as splitting graphs, where we plot the individual DCP volumes (V and $V_T - V$) against

the total volume (V_T).

3.3.1 Experimental Methods

	Reynolds Number	Bond Number	Ohnesorge Number	Weber Number	Capillary Number
Expression	$\rho u L/\mu$	$\Delta\rho g L^2/\sigma$	$\mu/\sqrt{\rho\sigma L}$	$\rho u^2 L/\sigma$	$\mu u/\sigma$
Experiments in [DOD21]	2×10^{0}	1×10^{-4}	3×10^{0}	2×10^{1}	1×10^{1}
Experiments in Section 3.3	4×10^{-2}	4×10^{-2}	4×10^{-1}	3×10^{-4}	6×10^{-3}

Table 3.1: Dimensionless number estimates. ρ, u, L, μ, g and σ are the density, characteristic velocity, characteristic length, viscosity, gravitational acceleration, and surface tensions respectively.

To experimentally validate our models, we perform experiments with macro-scale DCPs, which can be individually maniupulated and easily visualized. Macro-scale DCPs are fabricated of the same two polymers used to make micro-scale DCPs, hydrophilic poly(ethylene glycol) diacrylate (PEGDA, Mw $\approx$ 575; 437441, Sigma-Aldrich) and hydrophobic poly(propylene glycol) diacrylate (PPGDA, Mw $\approx$ 800; 455024, Sigma-Aldrich). Both polymers are mixed with 1% V:V photoinitiator (2-hydroxy-2-methylpropiophenone, Darocur 1173, 405655, Sigma-Aldrich) for UV-crosslinking. We fabricate macro-scale DCPs with an inner hydrophilic layer (PEGDA) and outer hydrophobic layer (PPGDA) as previously described [WOW20]. Using this approach we are able to create macro-scale DCPs with minimal variation in size and shape (CV<10%).

To replicate the physics of the microscale system with the macro-scale DCP's we use hydrophilic and hydrophobic fluid phases that have minimal density differences to study fluid break up. This is critical since surface tension forces dominate other forces such as gravity at the microscale (i.e. Bond number $\ll 1$). For the outer hydrophobic fluid phase we use

uncrosslinked, liquid PPGDA as it has similar density to water (1.07 g/cm^3). To minimize the gravitational effects further, we adjust the density of the water phase to match PPGDA by adding 8% V:V glycerol to the water solution, which results in a small Bond number (Table 3.1).

We experimentally study the splitting behavior of two DCPs using a 3D-printed, motorized rig in which macro-DCPs are clamped to and pulled apart at a constant speed while submerged in PPGDA oil (see Figure 3.2(a)). We begin the experiment with the DCPs touching and their aqueous fluid distributed between the DCPs as seen at $t = 0$ s in Figure 3.2(b). We then pull the DCPs apart at a relative speed of about 1 mm/s from each other. This is slow enough that dynamic effects are limited (Table 3.1). Eventually, the catenoid formed between the DCPs breaks, at which point we stop the experiment and carefully remove the DCPs from the PPGDA oil bath, leaving behind the water droplets captured by each DCPs as a sphere. We take a top view image of the water droplets and process the photos in MATLAB to calculate the volume of the water in each DCPs. We compare these observations with our simulations in Figure 3.3.

Additionally, we match our simulation's surface tension coefficients to the macro-scale experiments by making contact angle measurements. First, we normalize the water-oil coefficient $\sigma_{\text{wo}} = 1$. From here, we only need to examine the energy deviations from the empty DCP energy. Thus, we are only interested in $\sigma_{\text{op}} - \sigma_{\text{wp}}$, which is given by the contact angle [MBK87]. We measure the contact angle of a water droplet on a flat hydrophilic slab with the droplet and slab submerged in oil. The contact angle is 69.5°, so $\sigma_{\text{op}} - \sigma_{\text{wp}} = \cos(69.5°) = 0.35$.

3.3.2 Homogeneous Interaction

We study the interaction between a pair of homogeneous DCPs with the same shape and same size. Theoretical prediction of the behavior of the particle splitting graph is discussed in Chapter 2. In particular, Chapter 2 proves that there exists a volume V_1 such that for all volume $V_T < V_1$, one DCP takes no volume. They also prove that there exists a volume V_b

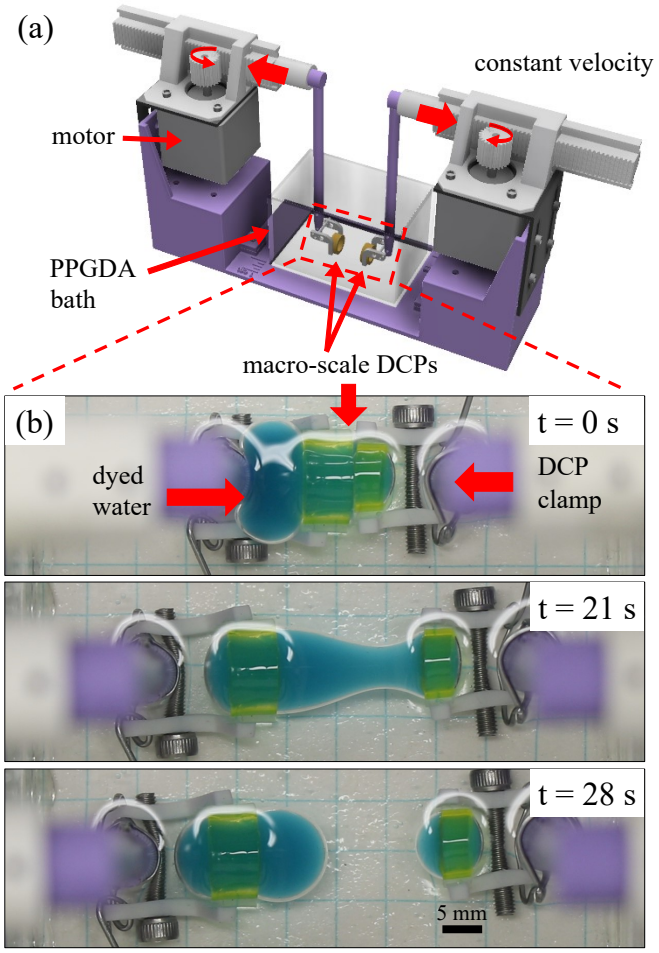

Figure 3.2: Experimental setup and time-lapse of macroscopic two-DCP interaction. (a) CAD diagram illustrating the experimental setup for making two DCPs interact by pulling them apart. (b) Top-view of time-lapse experiment of heterogeneous cylindrical DCPs (yellow) which are filled with a water-glycerol mixture (blue), submerged in a PPGDA bath. The left DCP is approximately twice the dimensions of the smaller right DCP. Scale 5 mm. Graph pad squares 6.35 mm.

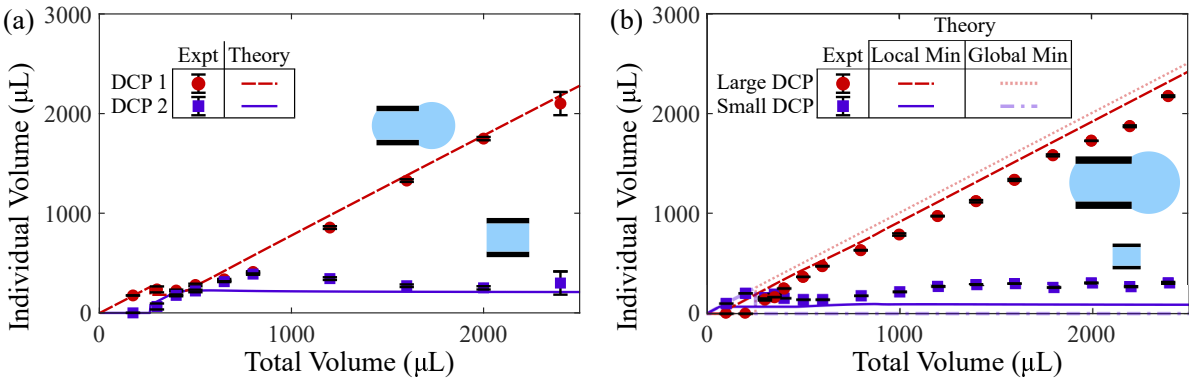

Figure 3.3: Fluid splitting graphs for cylindrical DCPs: (a) Splitting graph for two identical cylindrical DCPs (b) Splitting graph for two heterogeneous cylindrical DCPs, where one cylinder is larger than the other. The measurements of physical experiments (Expt) and the theoretical predictions based on the discussions Chapter 2 (Theory) are respectively represented by dots with error bars and colored lines. Experimental data (each point represents 3 trials and the error bars are one standard deviation long) is compared to theoretical results with particle geometry and surface tensions that match the physical experiment, explained in Section 3.3.1.

such that for all volume $V_T \geq 2V_b$, one DCP takes volume in a specific range around $V_{\min}$ and the other DCP takes the rest.

The splitting graph of two identical cylinders is shown in Figure 3.3(a), with the experimental data overlaid. The experimental macro-scale cylinders have an inner radius $r = 2.8$ mm, a hydrophilic layer radius $R = 4.0$ mm, a hydrophobic layer radius $R_{hb} = 5.2$ mm, and a height $h = 8$ mm. The physical system exhibits the same important splitting properties. For a range of small total volumes (V_T), one DCP takes no water. We call this interval the No-Splitting Range. There is another interval of V_T where DCPs split the volume evenly, called the Even-Splitting Range. For large V_T, one DCP takes close to its energy minimizing volume $V_{\min}$ while the other DCP takes the remaining water. This is called the Large-Volume-Limit Range. For a labelled example splitting graph, see Figure 3.4(a), and for the precise definitions, see Section 3.4.

3.3.3 Heterogeneous Interactions

In this section, we explore the splitting of different sized DCPs of the same shape, which we call a heterogeneous interaction. Heterogeneous interactions take place between a small and a large DCP of the same shape. These interactions can optimize mixing (discussed in Section 3.4.2). Here we consider a case study with a large cylinder ($r = 5.0$ mm, $R = 6.0$ mm, $R_{hb} = 7.0$ mm, and $h = 6.0$ mm) and a small cylinder ($r = 2.8$ mm, $R = 4.0$ mm, $R_{hb} = 5.2$ mm, and $h = 3.0$ mm). The splitting graph of both experimental results and theoretical results for these heterogeneous DCPs are shown in Figure 3.3(b). Unlike homogeneous DCP interactions in Figure 3.3(a), heterogeneous interactions lack an Even-Splitting Range (i.e. water does not evenly distribute between particles), which we exploit in our theory. Otherwise, the heterogeneous system exhibits a similar behavior as the homogeneous system with the No-Splitting Range for small V_T and the Large-Volume-Limit Range for large V_T.

In the No-Splitting Range, experimental results match well with theory; in the Large-Volume-Limit Range, there is a discrepancy between experiments and the theoretical volumes

that minimize (3.2). This discrepancy is explained by the difference between the global and local energy minimizers as well as system dynamics. One volume configuration minimizing (3.2) is the global energy minimizer, in which the small DCP has zero water volume and the large DCP has all of the water. However, both DCPs take water volume in a manner more consistent with the local energy minimizer of (3.2), in which the small DCP takes a volume close to the single DCP energy minimizing volume ($V_{\min}$) and the large DCP takes the remaining water. The preference towards the local energy minimizer is due to the energy associated with dewetting a DCP. Additionally, for *admissible* DCPs that are defined and studied in Section 3.4, the local non-zero minimizer is in fact the global minimizer. Figure 3.3(b) shows that the local energy minimizer explains the experimental data better than the global energy minimizer. However, the local energy minimizer still does not completely explain experimental observations, but there is a fairly uniform volume difference between the two. This is due to the dynamics of capillary breakup, which we do not consider in our theoretical predictions [TSO92]. For simplicity, we continue using the tractable energy minimizing strategy from (3.2) in our subsequent sections as an approximation of pairwise water splitting behavior.

3.4 Systems of Multiple Particles

In this section, we use the pairwise splitting model to simulate multi-DCP systems (homogeneous and heterogeneous). Within a system of DCPs, the DCPs exchange fluid with each other in randomly-chosen, pairwise interactions – resembling how DCPs collide and exchange fluids in experiments – to achieve a system-wide minimal energy distribution, resulting in a uniform distribution of water among the DCPs. These pairwise interactions follow the two-DCP splitting graph (Figure 3.3).

We develop an analytic theory for the PDF of the number of these Independent Random Interactions (IRIs) required for homogeneous and heterogeneous systems to converge to

equilibrium and show that the theory agrees well with numerical simulations. We further investigate the effects of heterogeneous DCPs on the number of IRIs. As long as the DCPs satisfy our requirements for α-*admissible* DCPs, as defined in Section 3.4.2, this new theory is independent of the DCP geometry.

3.4.1 Number of Independent Random Interactions for Homogeneous Systems

We first study the number of IRIs for a system of homogeneous DCPs, i.e. identical DCPs. We initialize the homogeneous system with all the water in one DCP. The system has converged when all but one DCPs contain water volume around $V_{\min}$, the energy minimizing volume, and the remaining DCP contains the excess water volume.

In Section 3.3.2, we introduce three volume ranges (Figure 3.4(a)). Here we also name their end points.

A No-Splitting Range: the interval, $[0, W_{A,U}]$, of small total volumes (V_T) where one DCP takes no water

B Even-Splitting Range: the interval $[W_{B,L}, W_{B,U}]$ of V_T where the DCPs split water evenly

C Large-Volume-Limit Range: the interval $[W_{C,L}, \infty)$ of V_T where one DCP is filled, i.e. contains a volume in $[F_L, F_U]$, while the other DCP takes the remaining water. We define $F_L = \frac{W_{B,L}}{2}$ (Figure 3.1) and $F_U = \min\left(W_{A,U}, \frac{W_{B,U}}{2}\right)$.

We show shortly that these are the only possible volumes, the other volumes are therefore not considered. After two DCPs interact, we denote the resulting smaller volume V_{sm} and the larger volume V_{lg}. To consider a system with simple DCP interaction behavior, we introduce the concept of an *admissible* DCP. We define a DCP to be an *admissible* DCP if

$$F_L \leq V_{\min} < F_U.$$

All hollow sphere and cylinder DCPs studied in this chapter are *admissible* DCPs.

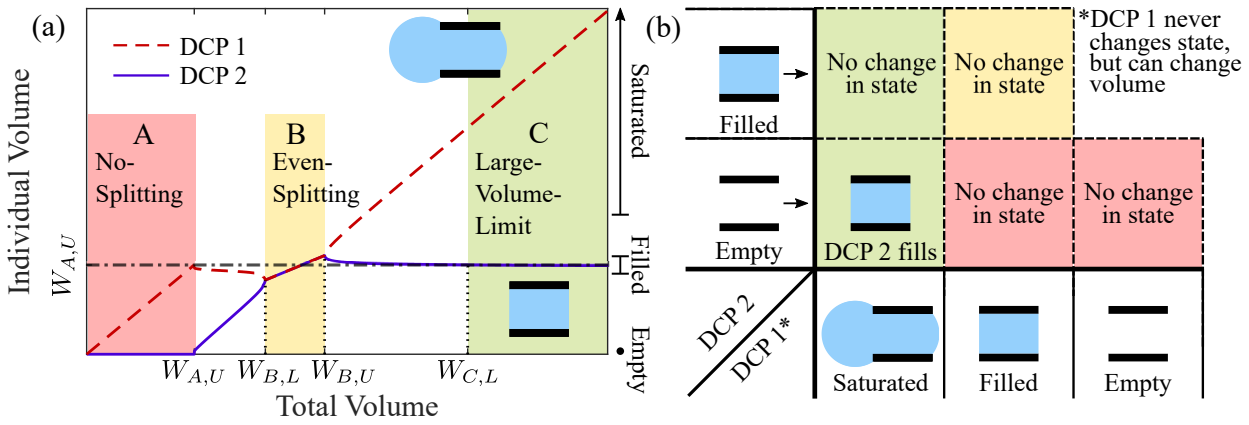

Figure 3.4: (a) An illustrative example of a homogeneous fluid splitting graph. $W_{A,U}$, $W_{B,L}$, $W_{B,U}$, and $W_{C,L}$ represent upper or lower volume boundaries of the No-Splitting (A), Even-Splitting (B), and Large-Volume-Limit (C) Ranges which are important to our analysis. $V_{\min}$ is the energy minimizing volume for a single DCP and is represented in Figure 3.1. (b) Possible DCP-DCP interactions in homogeneous system. DCPs can be in one of three states - empty, full, or saturated, carrying the entire system's excess fluid. Each dashed box indicates the equilibrium state after a 2-DCP interaction. The background color corresponds with a splitting range in (a), based on the summed volume of the initial DCPs.

We now consider a system of $N+1$ *admissible* DCPs. The system initially has all the of water attached to one DCP with the remaining DCPs empty. When the total system volume V_{t0} satisfies

$$V_{t0} \geq W_{C,L} + (N-1) \cdot F_U, \tag{3.3}$$

we claim that throughout the entire mixing process there are only three possible DCP states - empty DCPs, filled DCPs, and one saturated DCP with the remaining volume. A change in state would be, for example, an empty DCP becoming filled after interacting with the saturated DCP. We show this by considering all the possible interactions in a system as described above, which is summarized in Figure 3.4(b). For any pairwise interaction, we know that if $V_T > W_{C,L}$, one DCP is filled and the other DCP contains the remaining volume. Since $V_{t0} > W_{C,L}$, an interaction between the initial saturated DCP and an empty DCP

results in one filled DCP and one saturated DCP. This is still the case for all subsequent interactions between empty DCPs and the saturated DCP because the volume in the saturated DCP satisfies $V_{t0} - iW_{A,U} > W_{C,L}$ for all $i \in \{0, 1, \ldots, N-1\}$, the number of filled DCPs. The same reasoning shows that the interaction between a saturated DCP and a filled DCP does not result in any state change. Also since there is no interaction that results in two saturated DCPs, there is only one saturated DCP throughout the model. When two filled DCPs interact, the total system volume satisfies $W_{B,L} \leq 2F_U \leq W_{B,U}$, which results in even splitting. Although the volume in each DCP may change, both DCPs remain in the filled state. When a filled DCP interacts with an empty DCP, the total system volume is at most $W_{A,U}$. By the definition of $W_{A,U}$, we know that this interaction leaves one DCP empty, thus not changing the states of either DCP. It is clear that two empty DCPs do not change states after interaction. We have therefore showed that throughout the mixing process, all DCPs will fall into one of the three DCP states.

For the homogeneous system of DCPs, *convergence* is defined to be when all DCPs are filled except for the saturated DCP. The number of IRIs is defined as the number of pairwise random interactions to reach system *convergence*. The only state change occurs when an empty DCP becomes filled. Since filled DCPs cannot become empty, the number of filled DCPs monotonically increases and eventually every DCP except the saturated one becomes filled. The system reaches *convergence* in a finite number of interactions with probability one.

For a system of *admissible* DCPs with a V_{t0} that satisfies (3.3), the Total Number of IRIs is a random variable that follows a summed geometric distribution:

$$\begin{aligned} &\text{Total Number of IRIs} = \sum_{i=0}^{N-1} X_i, \\ &\text{where } X_i \sim \text{Geo}(p_i) \text{ with } p_i = \frac{N-i}{\binom{N+1}{2}}. \end{aligned} \tag{3.4}$$

X_i denotes the number of IRIs until the system makes a successful change of state from i filled DCPs to $(i+1)$ filled DCPs. A system with i filled and $N-i$ empty DCPs has $N-i$ possible pairs (empty-saturated) that can change state out of the total $\binom{N+1}{2}$ possible interactions.

Thus the number of IRIs until the next change of state, X_i, is a geometric distribution with the probability parameter p_i. This reasoning is similar to the Coupon Collector's Problem [FGT92]. We validate this theoretical result with numerical simulations in Section 3.4.4.

3.4.2 Number of Independent Random Interactions for Heterogeneous Systems

We consider a system of two differently-sized DCPs with the goal of filling all the smaller DCPs. We show that introducing large DCPs into the system decreases the number of IRIs. The system reaches *convergence* when all the small DCPs contain water within some volume range around $V_{\min}$. Here the large DCPs are auxiliary DCPs, providing a mechanism to transfer fluid to the smaller DCPs.

In the heterogeneous system, there are initially N_L large empty DCPs, N_S small empty DCPs, and one saturated large DCP which contains all the initial system volume. A large DCP has the same aspect ratio as a small DCP. And α is the ratio of the length scales of the two DCPs sizes. We assume the DCPs are all *admissible* DCPs, so the results in Section 3.4.1 still hold.

In contrast to Section 3.4.1, we only discuss two volume ranges present in Figure 3.5(a).

A No-Splitting Range: small total volumes (V_T) in the range $[W'_{A,L}, W'_{A,U}]$ where one DCP takes no water.

C Large-Volume-Limit Range: the interval $[W'_{C,L}, \infty)$ of V_T where the small DCP is filled, i.e. contains a volume in $[F'_L, F'_U]$, while the large DCP takes the remaining water. We define $F'_L = \max\left\{F_L, W'_{A,L}\right\}$ and $F'_U = \min\left\{W'_{A,U}, F_U\right\}$. $[F'_L, F'_U]$ is a subset of $[F_L, F_U]$.

The filled large DCPs contains a volume that is a scaling of the filled volumes of small DCPs as $[\alpha^3 F'_L, \alpha^3 F'_U]$.

Finally, we define an α-*admissible* DCP:

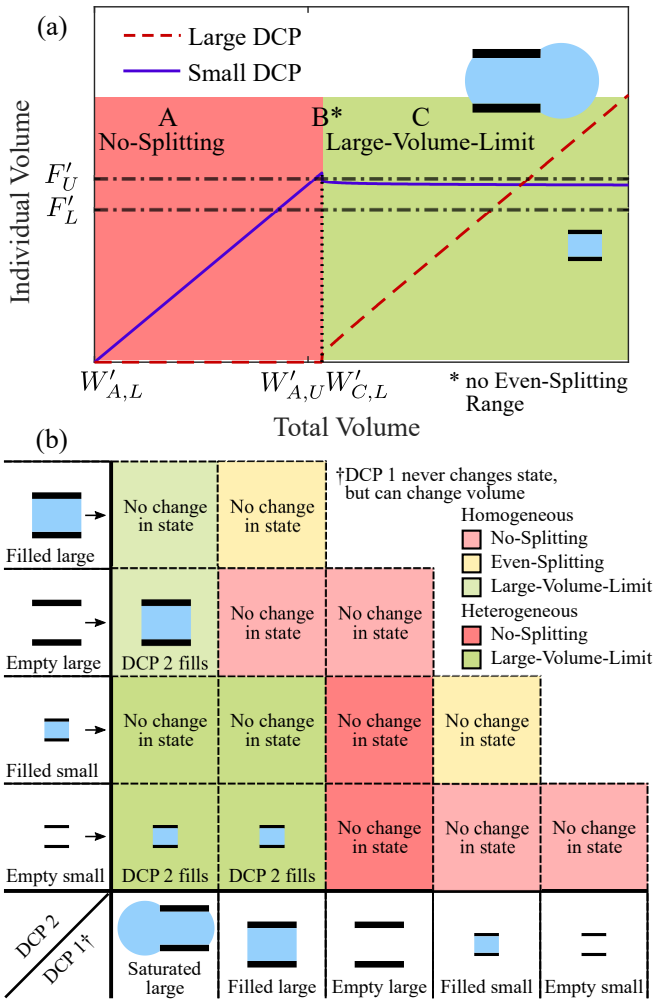

Figure 3.5: (a) An illustrative example of a heterogeneous splitting graph. $W'_{A,L}, W'_{A,U}$, and $W'_{C,L}$ represent the lower or upper boundaries of the No-Splitting (A) and Large-Volume-Limit (C) Ranges. For this example, the difference between $W'_{A,U}$ and $W'_{C,L}$ is very small (cf. Figure 3.3). Unlike the illustrative example, $W'_{A,L}$ does not necessarily have to be 0. (b) Possible DCP-DCP interactions in the heterogeneous system. The small DCP can be in one of two states - empty or full and the large DCP can be in one of three states - empty, full, or saturated, carrying the entire system's excess fluid. Each dashed box indicates the equilibrium state after a 2-DCP interaction, based on the summed volume of interacting DCPs.

1. Interactions between two same sized α-*admissible* DCPs satisfy the properties of an *admissible* DCP, and

2. Interactions between one small and one large (scale α) DCP have $V_{\min} < W'_{A,U}$.

3. Sufficiently large α (details discussed in the next paragraph)

With an $\alpha = 5$, the cylinder and hollow sphere DCPs in the parametric study in Section 3.5 are α-*admissible* DCPs. However this is not true in general. For example, short cylinders, with $1 \leq h/r < 2$, are not α-*admissible* DCP even though they are *admissible* DCPs.

Comment on the Scaling Ratio α for Heterogeneous System This paragraph explains the theoretical requirements on α for the results in Section 3.4.2 to hold. In practice, we can relax these constraints with minimal impact to our results. The core requirement is $\alpha^3 F_L \geq W'_{C,L}$ for every interaction, i.e., when a filled large DCP interacts with an empty small DCP, the small DCP is filled. We consider the worst case scenario: All N_S small empty DCPs interact with only one large DCP. In this case α needs to satisfy

$$\alpha^3 F_L = \alpha^3 V_{\min} \geq (N_S - 1) \cdot F'_U + W'_{C,L}. \tag{3.5}$$

Additionally, if every small DCP obtains water from a single large DCP, the volume in this large DCP should stay within the filled range to ensure that its future interactions follow the theoretical predictions. Thus also we need

$$\alpha^3 V_{\min} \geq (N_S - 1) \cdot F'_U + \alpha^3 \frac{W_{B,L}}{2}. \tag{3.6}$$

These requirements can lead to unreasonably large lower bounds on α, especially in a system with a large number of small DCPs (N_S). However, we can relax the bound on α with minimal deviation from our theory due to the probabilistic nature of the model. The essential condition is that the liquid volume in a filled large DCP should be larger than $W'_{C,L}$ throughout all the interactions. For a reasonable α value and a system with a significant number of large DCPs,

the worse scenario is unlikely to happen: there is only a small probability that all the small DCPs interact with a single large one; and large filled DCPs can interact with the saturated DCP and replenish their volumes.

For a system of α-*admissible* DCPs with total system volume

$$\begin{aligned} V'_{t0} \geq & (N_S - 1) \cdot F'_U + W'_{C,L} + \\ & (N_L - 1) \cdot \alpha^3 F_U + \alpha^3 W_{C,L} \\ =: & V_R \end{aligned} \tag{3.7}$$

and α sufficiently large that satisfies (3.5) and (3.6), the states of the DCPs are limited to: saturated large, filled large, empty large, filled small, and empty small. We denote this threshold system volume V_R. To show this, we first note that interactions between same-sized DCPs follow the splitting graph from Section 3.4.1. We then investigate interactions between large and small DCPs. When a large filled DCP interacts with a small empty DCP, with α above, the total interaction volume is $V_T \geq \alpha^3 F_L \geq W'_{C,L}$. Thus, the small DCP takes a volume of water that is in the Large-Volume-Limit Range, near $V_{\min}$. Though the large DCP volume decreases slightly, it remains in the Large-Volume-Limit Range. The same reasoning shows that an interaction between a saturated large DCP and a empty small DCP fills the small DCP. For the same reason, (saturated large) − (filled small) and (filled large) − (filled small) interactions do not change the states of the DCPs. Interactions between an empty large DCP and a filled small DCP do not change the states of the DCPs either. The small DCP takes all the volume in the system because the total volume $W'_{A,L} \leq F'_L < V_T < F'_U \leq W'_{A,U}$. Therefore we have shown that for heterogeneous DCP system, there are only three possible interactions that change the states of DCPs. The possible interactions are shown in Figure 3.5(b).

Similar to the homogeneous system, the number of IRIs for heterogeneous systems can be calculated theoretically. For a system as described above, the number of filled large and small DCPs monotonically increases, and eventually all small DCPs become filled. At this point, the system has reached *convergence*. The number of IRIs follows a "mixture model"

of a summed geometric distribution [MLR19]. Using the mixture model, the calculation of the probability density function generalizes the calculation in Section 3.4.1. A more detailed explanation can be found below in Section 3.4.3.

3.4.3 Proof of Probability Distribution of Number of IRIs

In the previous Section 3.4.2, we show that for a system of large and small α-*admissible* DCPs with a sufficiently large initial volume V'_{t0}, the number of IRIs follows a mixture of summed geometric distributions. This section details the calculation for the PDF of the number of IRIs. This calculation is a generalization of the calculation in Section 3.4.1 with additional use of the mixture model [MLR19].

For a system with N_S small particles and N_L large particles, we identify each state of our system in terms of a two element array: $[LF \;\; SF]$. Here, LF is the number of large filled DCPs, and SF is the number of small filled DCPs. The numbers of large empty and small empty DCPs are $N_L - 1 - LF$ and $N_S - SF$ respectively, with one large DCP that stays saturated during the mixing. All the possible states of $[LF \;\; SF]$ are organized graphically in Figure 3.6.

As we constructed in Section 3.4.2, the heterogeneous system is initialized such that the entire system volume V'_{t0} is in a single large saturated DCP. Therefore, the state array for the initial state is $[0 \;\; 0]$ and is represented in Figure 3.6 as the green cell. As the DCPs interact, there are only three interactions that change the states of the DCPs from empty to filled (Figure 3.5). Therefore, LF and SF only increase, which correspond respectively to the state moving upwards or rightwards in Figure 3.6. The system reaches *convergence* when $SF = N_S$, which is represented by cells in dark blue in Figure 3.6.

Similar to Section 3.4.1, the PDF for the number of interactions needed to fill a DCP (large or small) is modeled as the arrival time of a Bernoulli process. The heterogeneous system is more complicated because there are two possible state changes: a small DCP fills

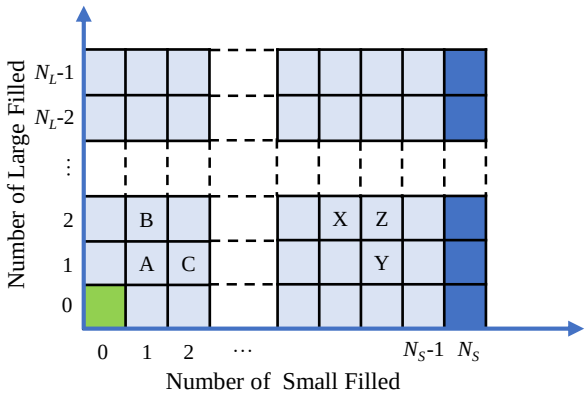

Figure 3.6: Graphical representation of all possible states of a heterogeneous DCP system with N_L large DCPs and N_S small DCPs. The green cell represents the initial state with a state array [0 0], and the dark blue cells represent the final states where all small DCPs are filled ($SF = N_S$). The letters in the boxes correspond the three-state systems in Figure 3.7.

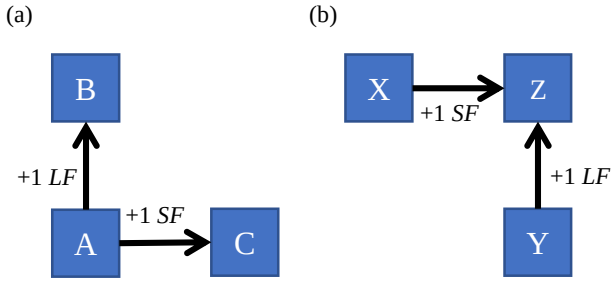

Figure 3.7: Graphical representation of example three-state systems. (a) State A can change into State B when a large DCP fills from empty and into State C when a small DCP fills. (b) State Z can be arrived at from State X when a small DCP fills from empty and from State Y when a large DCP fills.

or a large DCP fills. We calculate the number of IRIs needed to reach *convergence* using an inductive argument. The PDF for the number of IRIs needed to move out of a certain state uses information about how a state changes into subsequent states (Figure 3.7 (a)). Consider a state A, such that there are two possibilities for the next stage: a large DCP becomes filled and the state moves upward to B or a small DCP becomes filled and the state moves rightward to C. We denote the state arrays: $state_{\mathrm{A}}$= $[LF_A\ SF_A]$, $state_{\mathrm{B}}$= $[LF_A + 1\ SF_A]$, and $state_{\mathrm{C}}$= $[LF_A\ SF_A + 1]$.

Given that there are a total of $T = N_S + N_L$ DCPs in the system, the total number of possible interactions is $d = \binom{T}{2}$. The probability that an interaction changes the state of the system from $state_{\mathrm{A}}$ to $state_{\mathrm{B}}$ is denoted p_B. In order for this change of state to happen, one of the empty large DCPs must become filled by interacting with the saturated DCP, so $p_B = (N_L - 1 - LF_{\mathrm{A}})/d$. Similarly, the probability that an interaction changes the state from $state_{\mathrm{A}}$ to $state_{\mathrm{C}}$ is denoted p_C. For this change of state to occur, one of the small empty DCPs must interact with the saturated large DCP or a filled large DCP, so $p_C = (LF_{\mathrm{A}} + 1)(N_S - SF_{\mathrm{A}})/d$. We consider the process of the system exiting $state_{\mathrm{A}}$ as a Bernoulli process with probability $p_B + p_C$. The PDF for the number of interactions before the state changes from A (to either state B or C) is a geometric distribution:

$$\mathrm{Geo}\left(p_B + p_C\right).$$

We regard the particular jump from $state_{\mathrm{A}}$ to $state_{\mathrm{B}}$ and $state_{\mathrm{A}}$ to $state_{\mathrm{C}}$ as a splitting of the Bernoulli process with the splitting probability $p_B/(p_B + p_C)$ and $p_C/(p_B + p_C)$ respectively [Str10].

We also need to know the probability that the system visits a certain cell as the system evolves from the initial state to *convergence*. We denote the probability that a path traverses through $state_{\mathrm{A}}$ by q_A and similarly define q_B and q_C for $state_{\mathrm{B}}$ and $state_{\mathrm{C}}$ respectively. We also denote the probability that a path traverses through $state_{\mathrm{A}}$ and then $state_{\mathrm{B}}$ by $q_{A\to B}$; define $q_{A\to C}$ similarly. It is clear that $q_{A\to B} + q_{A\to C} = q_A$. We have from the previous

paragraph that

$$q_{A\to B} = q_A \frac{p_B}{p_B + p_C} \quad \text{and} \quad q_{A\to C} = q_A \frac{p_C}{p_B + p_C}.$$

We now change our perspective and focus on how the system reaches a certain state from the two states immediately prior. For example, we single out such a three-state system: a system of three states such that state Z is arrived via state X (from the left) or state Y (from below) (Figure 3.7(b)). We describe these states using the state array: $state_{\mathrm{X}}$= $[LF_Z \;\; SF_Z - 1]$, $state_{\mathrm{Y}}$= $[LF_Z - 1 \;\; SF_Z]$, and $state_{\mathrm{Z}}$= $[LF_Z \;\; SF_Z]$.

We observe that $state_{\mathrm{Z}}$ is a mixture of two states described by different PDFs. We assume inductively that we know f_X, f_Y, q_X, and q_Y and use the formula for the theory of mixture models to calculate the mixture's PDF (f_Z) [MLR19] ($*$ denotes convolution):

$$f_Z = r_{X\to Z}(f_X * f_{X\to Z}) + r_{Y\to Z}(f_Y * f_{Y\to Z}), \tag{3.8}$$

where $r_{X\to Z}$ and $r_{Y\to Z}$ are the fraction of $state_{\mathrm{Z}}$ that comes from $state_{\mathrm{X}}$ and $state_{\mathrm{Y}}$ respectively. $f_{X\to Z}$ is the PDF for the number of interactions that occur before the system changes state from $state_{\mathrm{X}}$ to $state_{\mathrm{Z}}$. Then $f_X * f_{X\to Z}$ is the PDF for the number of IRIs needed to reach $state_{\mathrm{Z}}$ from $state_{\mathrm{X}}$ and similarly for $f_Y * f_{Y\to Z}$. Our inductive step is complete if we calculate $r_{X\to Z}$, $r_{Y\to Z}$ and $f_{X\to Z}$, $f_{Y\to Z}$.

From the analysis of the ABC system, we calculate $f_{X\to Z}$, $f_{Y\to Z}$, $q_{X\to Z}$, and $q_{Y\to Z}$. Since all paths that visit $state_{\mathrm{Z}}$ must come from either $state_{\mathrm{X}}$ or $state_{\mathrm{Y}}$, the probability that a path traverses through $state_{\mathrm{Z}}$ is $q_Z = q_{X\to Z} + q_{Y\to Z}$. Then it follows that if a path traverses through $state_{\mathrm{Z}}$, the probability that the path arrives from $state_{\mathrm{X}}$ is

$$r_{X\to Z} = \frac{q_{X\to Z}}{q_Z},$$

and the probability that the path arrives from $state_{\mathrm{Y}}$ is

$$r_{Y\to Z} = \frac{q_{Y\to Z}}{q_Z}.$$

Through this formulation, we now have defined all of the components in (3.8) and can calculate the PDF of a new state cell from past state cells. Note that in the edge cases with $SF = 0$ or $LF = 0$, these states have only one source. In addition, the final states have $SF = N_S$ and correspond to the right most column in our state matrix. For these final states, there is only one source, which is from the left, as the cell below has already reached *convergence*.

The final distribution for the number of IRIs is the mixture of these N_L possible end states. For all the possible end states E_i, we have the corresponding probability that a path ends up at that end state q_{E_i} and the IRIs PDF f_{E_i}. We use the mixture model to derive the final probability density function:

$$f_{\text{final}}(x) = \sum_{i \in [0, N_L - 1]} q_{\text{E}_i} f_{\text{E}_i}(x).$$

An example of this PDF is presented in Figure 3.8b. This probabilistic methodology is applicable to systems with relaxed assumptions and more states. We validate this theoretical result with numerical simulations in the following section.

3.4.4 Probability Density Function Analysis of the number of IRIs

Equation (3.4) provides the probability density function for the number of IRIs needed to achieve a steady state redistribution of water amongst a large number of homogeneous DCPs. In Section 3.4.3, we present a recurrence procedure for the heterogeneous case of two DCP sizes. Here we compare these theoretical results with numerical simulations of pairwise IRIs. From these results, we find the optimal large to small particle ratio in the heterogeneous system to minimize the number of IRIs needed to reach steady state.

We consider a homogeneous system with 300 DCPs and initial system volume, V_{t0}, satisfying (3.3). We run 1,000 trials for this system. Figure 3.8a compares the IRIs distribution of the numerical simulations and our theoretically calculated probability density function (3.4). We perform a similar comparison of the IRIs distribution for a heterogeneous system

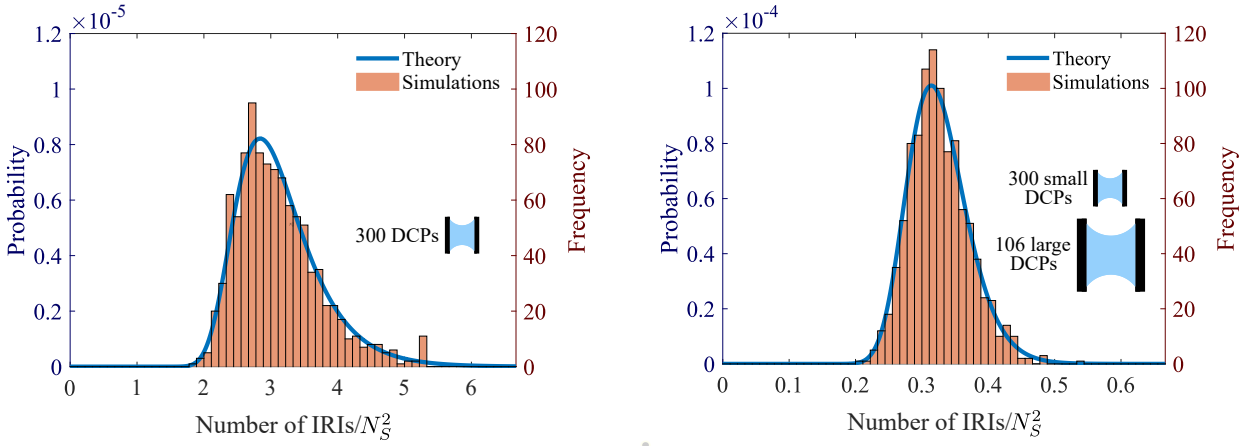

(a) (b)

Figure 3.8: Theoretical number of IRIs compared with numerical simulations. The histogram shows the distribution of number of IRIs from the numerical simulations (1,000 trials), and the blue curve is our theoretical prediction (3.4). Notice the change in the range of the x-axis. (a) Number of IRIs of a system with 300 homogeneous DCPs. The system starts with one saturated DCP with sufficiently large volume. (b) Number of IRIs of a system with 106 large DCPs and 300 small DCPs. The system starts with one saturated large DCP with sufficiently large volume.

with 106 large ($\alpha = 5$) DCPs and 300 small DCPs; all DCPs are empty initially, except for a large DCP that contains V'_{t0} satisfying (3.7). The results are shown in Figure 3.8b.

From Figure 3.8a and Figure 3.8b, we observe that introducing large DCPs decreases the number of IRIs required to reach equilibrium, as the presence of filled large DCPs increases the probability that a small DCP becomes filled. However, an excessive number of large DCPs slows the *convergence* of small DCPs. We choose the number of large DCPs to optimize $\overline{M}$ and $\overline{M} + 2\sigma_M$, where $\overline{M}$ is the mean number of IRIs and σ_M is its standard deviation.

We explore the optimal ratios of large to small DCPs for various systems in Figure 3.9. We consider a system of 300 small DCPs with i large DCPs. Figure 3.9a shows $\overline{M}$ and $\overline{M} + 2\sigma_M$ as a function of the number of large DCPs, i. The case with 106 large DCPs

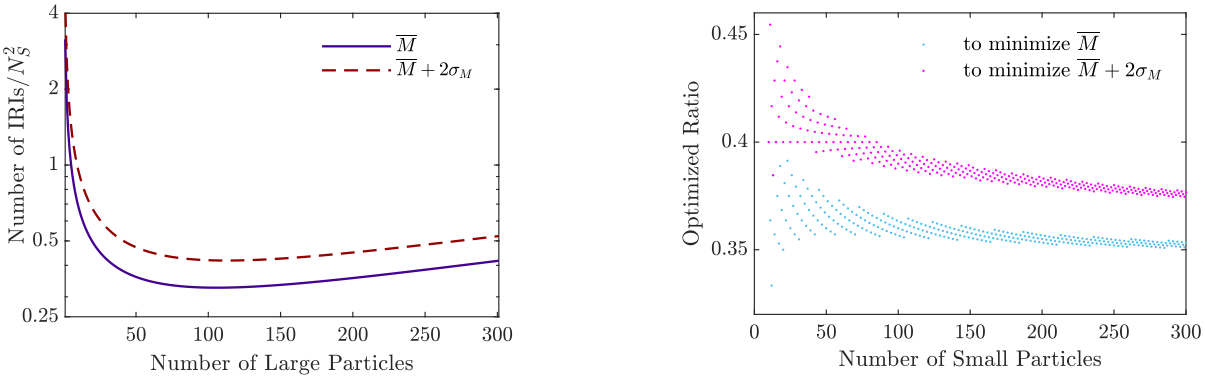

(a) (b)

Figure 3.9: Optimal number of large DCPs in heterogeneous systems. (a) Number of IRIs needed to achieve steady state vs. the number of large DCPs present. We plot the mean of number of IRIs ($\overline{M}$) and the mean plus two standard deviation of the number of IRIs ($\overline{M}+2\sigma_M$) for a system with 300 small DCPs and varying number of large DCPs. 106 large DCPs minimize $\overline{M}$ and 113 large DCPs minimize the $\overline{M}+2\sigma_M$. The y-axis is on log scale to emphasize the details at small value. (b) The optimal ratio of large to small DCPs to reduce the mean of number of IRIs ($\overline{M}$) or the mean plus two standard deviations of the number of IRIs ($\overline{M}+2\sigma_M$) for different numbers of small DCPs. The optimal ratios for optimizing both are between 0.3 to 0.4. The sweeping pattern is solely a product of the discrete increase in small DCPs.

minimizes $\overline{M}$ and 113 minimizes $\overline{M}+2\sigma_M$. Notice that introducing even a few large DCPs decreases the number of IRIs significantly. We repeat this calculation to find the optimal ratio for different numbers of small DCPs (Figure 3.9b). The ratios that minimize $\overline{M}$ and $\overline{M}+2\sigma_M$ are between 0.3 and 0.4.

3.5 Optimizing Particle Geometry

In this section, we present a method to optimize heterogeneous α-*admissible* DCPs to address system uniformity and conservation of target fluid. We first describe the parameters involved and then provide an example of the optimization process for cylindrical DCPs. An optimal DCP shape should minimize the variation of the fluid volume captured by the small DCPs. We consider a heterogeneous system with a sufficiently large initial system volume. After *convergence*, a small DCP is filled.

We define the range size R_C as the possible volume range of water after *convergence*. We calculate R_C numerically by finding the range of volume that the small particle takes in the Large-Volume-Limit Range. This is a subset of the theoretical range $[F'_L, F'_U]$. Moreover, in order to conserve target fluid, the optimal DCP should minimize the threshold system volume V_R. Recall that, in (3.7), V_R depends on both system parameters and DCP geometry. System parameters include the number of small and large DCPs in a system (N_S and N_L). DCP geometry affects the threshold volumes ($W_{C,L}$ and $W'_{C,L}$) and the upper bound of the filled range (F_U and F'_U). To find an optimal DCP geometry, we fix the system parameters and minimize R_C and V_R by exploring the geometric parameters.

3.5.1 Optimal Cylinder Geometry

Based on the above criteria, we perform a parametric study on cylinder DCPs to find the best cylindrical geometry for laboratory applications (for hollow sphere geometries see the next section, Section 3.5.2). This analysis exemplifies the general procedure of finding optimal DCP geometries within a class of DCPs. Following our discussion of cylinder DCPs in Section 3.2, we view the DCP as hydrophilic with an infinitesimally thin hydrophobic coating on the outside. For our case study, σ_{wo} is normalized to 1. For the hydrophilic surface, the water contact angle is acute with $\cos(\theta) = \sigma_{\text{os}} - \sigma_{\text{ws}} = 0.8$; for the hydrophobic surface, the water contact angle is obtuse with $\cos(\theta) = \sigma_{\text{os}} - \sigma_{\text{ws}} = -0.8$. Additionally, the size ratio of large

to small DCP is $\alpha = 5$. We also normalize DCP size such that $V_{\min} = 1$. The cylinder DCP geometries therefore have two parameters: the ratio of outer to inner radius R/r and the ratio of height to inner radius h/r. We vary those two to produce different DCP geometries.

We find that the optimal cylinder to minimize R_C is long (i.e. has larger h/r). In Figure 3.10a, we present the range of R_C for these geometries. We also see that the outer radius of the DCP does not affect R_C.

To minimize V_R in our parametric sweep, we must choose specific numbers of small and large DCPs. We choose $N_S = 300$ small and $N_L = 106$ DCPs based on Section 3.4.2. We calculate V_R using (3.7) and present the results in Figure 3.10b. Cylinders that are longer and have a thinner outer wall have lower V_R.

For our example of 300 small and 106 large DCPs, the cylinder DCP that minimizes both R_C and V_R is the DCP that is long and has a thin hydrophilic wall. In Figure 3.10c, we present the 2 dimensional cross section of the optimal cylinder DCP, which has $R/r = 1.1$, and $h/r = 4$. A DCP with such thin walls is structurally unstable. However, the hydrophobic wall thickness does not affect the behavior of the DCP, so the optimal DCP can be reinforced with a thick outer hydrophobic layer.

From 3.10a, (b), R_C and V_R are dominated by the parameter h/r: R_C and V_R are smaller when h/r is larger. This trend is due to the strong influence of h/r to the relative volume of the partial spheres that bulge outside the cylinder (as the one in Figure 3.1c) compared to the energy minimizing volume $V_{\min}$. As we increase the h/r ratio, the relative volume of water in the partial spheres decreases, which in turn decreases the values of R_C and V_R.

3.5.2 Optimal Hollow Sphere Geometry

We repeat the parametric study in Section 3.5.1 for hollow sphere DCPs. We use the same surface tension coefficients, α value, and numbers of large and small DCPs (N_S and N_L) in the calculation of R_C and V_R. We use the same numbers of DCPs because the results

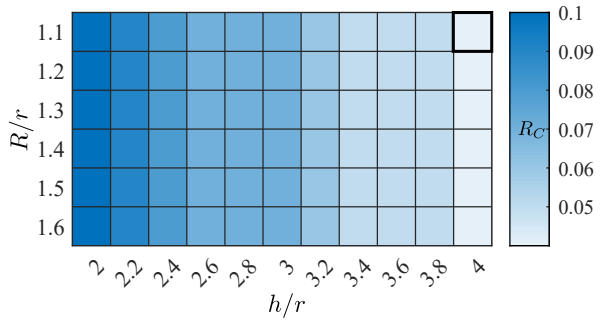

(a)

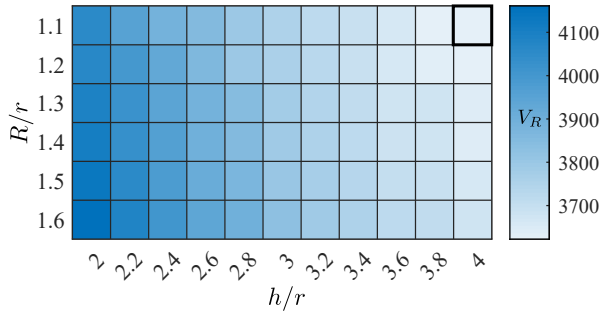

(b)

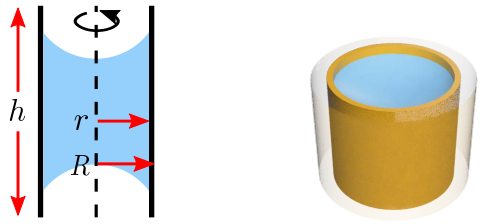

(c)

(d)

Figure 3.10: Parametric sweep of cylinder geometries for DCP optimization. (a) Heat map representing convergent range R_C. (b) Heat map representing initial volume requirement for target fluid V_R. (c) Cross section of optimal cylindrical DCP with outer radius/inner radius $R/s = 1.1$ and height/inner radius $h/r = 4$. This DCP has $R_C = 0.04$ and $V_R = 3623$. (d) Full optimal cylindrical DCP.

of Section 3.4.4 do not depend on the particle geometry. After we normalize $V_{\min} = 1$, the hollow sphere DCPs have two parameters: θ and γ (Figure 3.12). We obtain heatmaps for the

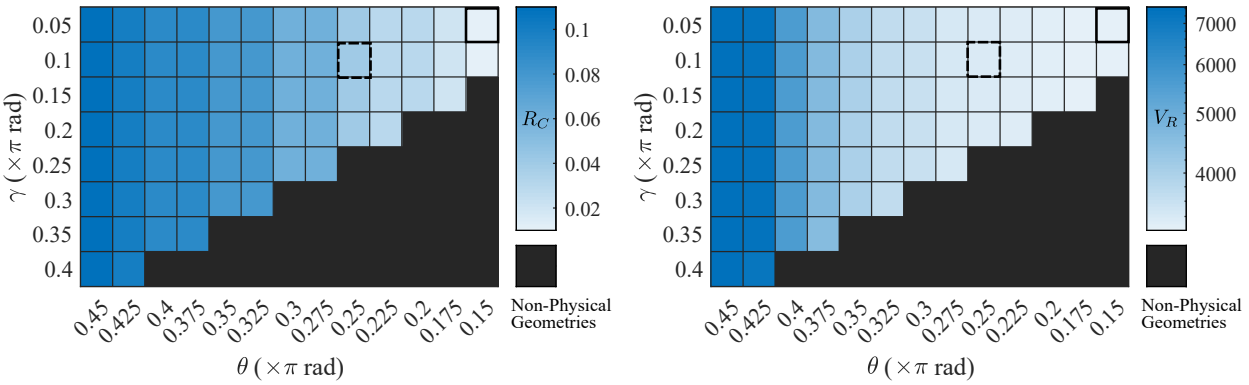

(a) (b)

Figure 3.11: The values of the optimization criteria for different hollow sphere geometries, presented using heat maps. The theoretical optimal DCP geometry is represented by the box with a thick solid outline and the best DCP for physical experiments is marked by thick dashed outline. (a) Heat map representing R_C. DCPs that have smaller openings have lower R_C while the outer wall thickness of the DCP does not affect R_C. (b) Heat map (log scale) representing V_R. The DCP geometries with smaller openings and thicker walls have lower V_R, with the effect of wall thickness much smaller than the effect of opening size. The theoretical optimal DCP has $R_C = 0.01$ and $V_R = 3228$. The best DCP for physical experiments has $R_C = 0.04$ and $V_R = 3388$.

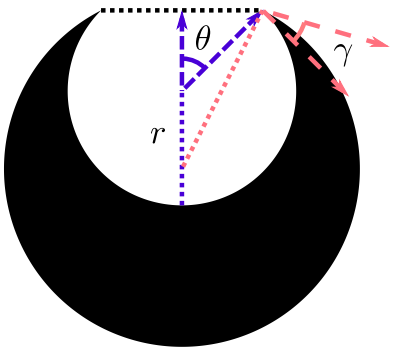

Figure 3.12: Graphical representation of parameters r, θ, and γ for hollow sphere geometries drawn over a 2D cross section of the hollow sphere DCP. r is the radius of the inner sphere, θ is the angle between the vertical and the line connecting the inner center to the edge of the opening, and γ is the angle between the inner sphere and the outer sphere at the edge of the opening. The parameter angles are drawn with dashed arrows. Radii of the inner (blue) and outer sphere (red) are drawn as dotted lines.

lengths of the convergent ranges, R_C, and threshold system volumes V_R for these geometries in Figure 3.11. We observe that geometries with a smaller θ have lower R_C and lower V_R. On the other hand, γ has a smaller effect on R_C and V_R, and lowering γ only lowers V_R. We observe that R_C and V_R are dominated by the value of θ. Here θ for spherical DCPs has an analogous role to h/r for cylindrical DCPs, in Section 3.5. The value θ determines the relative water volume of the partial sphere.

The hollow sphere DCP geometry that minimizes both the convergent range (R_C) and the system volume requirement (V_R) has a small opening and thin shell (Figure 3.13a). While the best theoretical DCP has a small opening and thin shell, additional factors are involved in a physical DCP design. Authors of [WOW20] show that a small opening makes it difficult for a DCP to load liquid. In addition, a thin shell is difficult to manufacture on the microscale. Taking the above factors into consideration, we can modify the parameters for an optimal hollow sphere DCP that would fare well in physical experiments (Figure 3.13b).

(a) (b)

Figure 3.13: Cross sectional representation for (a) the theoretical ideal DCP and (b) best DCP for physical experiments based on Figure 3.11. The physical parameters of (a) are $\theta = 0.15\pi$ rad $\gamma = 0.05\pi$ rad. and for (b) are $\theta = 0.3\pi$ rad and $\gamma = 0.1\pi$ rad.

CHAPTER 4

Dynamics of small particle inertial migration in curved square ducts

This chapter is based on [HHB22] (Reprinted manuscript with permission from [HHB22] as follows: Kyung Ha et al., SIAM Journal on Applied Dynamical Systems, 21(1):714–734, 2022 Copyright (2022) by SIAM. https://epubs.siam.org/doi/abs/10.1137/21M1430935).

4.1 Introduction

Our particle tracking model, which we call the Zero Level Fit (ZeLF) model, for neutrally buoyant spherical particles suspended in flow through curved square ducts is similar to that of Rasooli and Çetin [RC18] but differs in a few key ways: (a) the axial particle velocity is in constant equilibrium with the surrounding fluid, (b) the forces within a cross-section are decomposed solely into a secondary flow drag and inertial lift force, and (c) both the secondary flow drag and inertial lift force are modeled via relatively simple formulae. The assumption in (a), which includes neglect of the added mass force, is reasonable because equilibrium in the main direction of flow is reached quickly compared to the time scale of particle migration. Moreover, as the particle migrates in the cross-sectional plane the change in axial velocity is sufficiently smooth and slow for equilibrium to be maintained. The decomposition in (b) comes about after the careful analysis and decomposition of the forces on a neutrally buoyant particle in [HSB19] which, for example, reveals that the centripetal and centrifugal forces are approximately equal and opposite for a neutrally buoyant particle. For (c) we use an

approximation of inertial lift which preserves the topological structure of the zero level curves of the inertial lift force to ensure an accurate prediction of equilibria over a wide range of problem parameters. Put together, these simplifications expedite the calculation of particle trajectories allowing a detailed study of the resulting dynamical system.

While simulation data from [HSB19] can be interpolated directly and applied to the integration of particle trajectories, the ZeLF model provides a simpler closed-form model, facilitating rapid prototyping. Existing models in the literature often focus on modeling the inertial lift force as a sum of wall-induced, slip-shear and shear-gradient-induced components. Such models are generally one-dimensional in nature owing to the historical development of this decomposition via a study of particle migration in one-dimensional flows between two plane parallel walls. Rasooli and Çetin [RC18] remark that the application of such models "for the prediction of equilibria for particles in 3D Poiseuille flow in square and rectangular channels is quite questionable". They instead use Hood et al.'s approximation of the inertial lift force in straight rectangular ducts [HLR15] for their own particle tracking model applied to flow through curved rectangular ducts. Harding [Har18] explored the idea of combining the inertial lift force from a straight duct with drag forces induced from curved duct flow, which is a simple but useful way to describe behavior in curved ducts.

Using the ZeLF model we study the dynamics of particle migration in a curved square duct. We show that there are three regimes, a small κ regime in which a small number of stable equilibria exist, a large κ regime in which two stable attracting orbits exist, and the transition between these two regimes. This intermediate κ regime is of particular interest as it has only one focusing point. For this regime, we investigate the axial distance and time scale required for the focusing to occur, and how these depend on initial particle location in the cross-section. While previous studies have only looked at the dynamics within the cross-section, the axial dynamics are extremely important in the context of applications (e.g. cell isolation and separation) in which it is necessary for particles to be focused by the time they reach the end of the duct.

The chapter is organized as follows. Section 4.2 reviews the previous work done on particle flows in curved ducts. Section 4.3 describes how the ZeLF model for the particle dynamics is constructed. In particular, this section details the construction of the different components and how they are ultimately assembled for estimating particle trajectories to quickly and easily study the dynamics. In addition, the accuracy of the ZeLF model is shown by comparing it with the numerical model of [HSB19]. The ZeLF model is then used in Section 4.4 to analyse the migration dynamics of a small particle for the three regimes of small, intermediate and large κ value. We also illustrate how these compare with the dynamics predicted by the numerical model of [HSB19].

4.2 Background

The general setup of our curved square duct is depicted in Figure 4.1. The horizontal and vertical coordinates within the duct cross-section are $(r, z) \in [-\ell/2, \ell/2] \times [-\ell/2, \ell/2]$ where ℓ is the side length of the square cross-section. The cross-sectional coordinates map to points in the three dimensional duct via

$$\mathbf{x}(\theta, r, z) = (R + r)\cos(\theta)\mathbf{i} + (R + r)\sin(\theta)\mathbf{j} + z\mathbf{k}\,, \tag{4.1}$$

where θ is angular distance along the duct and R is the bend radius of the duct (measured to the center of the cross-section). The dimensionless parameter $\epsilon := \ell/(2R)$ is used to characterise the bend radius relative to half the cross-section height.

Let $\bar{p}, \bar{\mathbf{u}}$ describe the pressure and velocity fields, respectively, of a steady pressure driven flow through the curved square duct in the absence of any particles. The fluid is assumed to be incompressible with uniform density ρ and uniform viscosity μ. For convenience we separate $\bar{\mathbf{u}}$ into its axial component $\bar{\mathbf{u}}_a$ and secondary component $\bar{\mathbf{u}}_s$, specifically

$$\bar{\mathbf{u}}_a := (\bar{\mathbf{u}} \cdot \mathbf{e}_\theta)\mathbf{e}_\theta\,,$$

$$\bar{\mathbf{u}}_s := \bar{\mathbf{u}} - \bar{\mathbf{u}}_a\,.$$

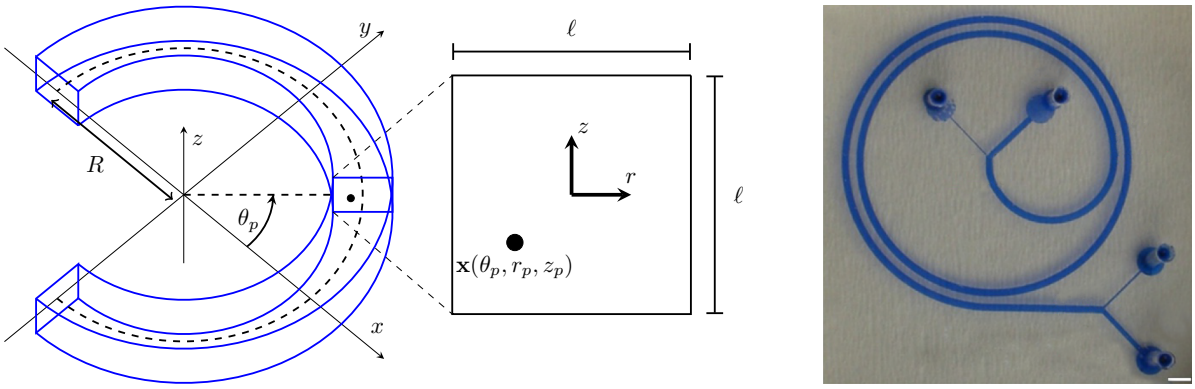

(a) (b)

Figure 4.1: Configurations of curved ducts. (a) Curved duct with square cross-section containing a spherical particle located at $\mathbf{x}_p = \mathbf{x}(\theta_p, r_p, z_p)$. The enlarged view of the cross-section around the particle illustrates the origin of the local r, z coordinates at the center of the duct, as first described in [HSB19]. The bend radius R is with respect to the center-line of the duct and is quite small here for illustration purposes. Note that we do not consider the flow near the inlet/outlet. (b) Photo of an actual curved microchannel, provided by and reproduced with the permission of the Warkiani Laboratory, University of Technology Sydney, Australia. Notice the bend radius is approximately constant for 7/4 turns. The scale bar on the bottom right is 2cm.

The maximum of $\bar{\mathbf{u}}_a$ is taken to be the characteristic flow velocity and is denoted by U_m. It is assumed that the Dean number $K = \mathrm{Re}_c^2 \epsilon$, where $\epsilon := \ell/(2R)$ (as defined earlier) and $\mathrm{Re}_c = (\rho/\mu) U_m \ell/2$ is the channel Reynolds number, is small enough that the inertia of the fluid flow through the curved duct does not perturb the axial velocity component significantly from the Poiseuille flow obtained in a straight duct. The secondary flow $\bar{\mathbf{u}}_s$, consisting of two counter rotating vortices in the cross-sectional plane, scales with $U_m\sqrt{K\epsilon}$ [Har19].

A spherical particle with radius $a < \ell/2$ is then suspended in the fluid flow resulting in the new pressure and velocity fields $p, \mathbf{u}$, respectively. The location of the particle is described by the location of its center $\mathbf{x}_p = \mathbf{x}(\theta_p, r_p, z_p)$. We assume the particle is free

to spin, which features in the calculation of the forces that influence its motion [HSB19]. However, in this study we do not track the particle spin as our aim is to produce a simplified model of the particle's position. The flow fields $p, \mathbf{u}$ are non-steady due to the motion of the spherical particle suspended in it. However, as in [HSB19], we move to the reference frame rotating with the cross-section containing the particle center, in which the angular coordinate is $\theta' = \theta - \theta_p$ and the radial and vertical coordinates remain unchanged. In this rotating reference frame, the fluid motion may be taken as steady and a disturbance flow $q', \mathbf{v}'$ is introduced which describes the difference between $\bar{p}, \bar{\mathbf{u}}$ and $p, \mathbf{u}$ in that frame. The force on the particle can be decomposed into three components: a gravity/buoyancy balance $\mathbf{F}_g$, a centrifugal/centripetal force balance $\mathbf{F}_c$ and a remaining hydrodynamic component $\mathbf{F}_{nb}$. There is an analogous decomposition of the torque which we do not describe in detail.

A recent paper explored the effects of non-neutral particle buoyancy for curved ducts having a rectangular cross-section [HS20]. Perturbations due to non-neutral buoyancy were found to be small for Froude numbers larger than 3, $\mathrm{Fr}^2 = U_m^2 a/(g\ell^2)$, and particle density ρ_p satisfying $|\rho_p - \rho| \leq \rho/2$. Since this is the case for typical applications of inertial microfluidics, for simplicity, we here restrict attention to neutrally buoyant particles.

For a neutrally buoyant particle (for which $\mathbf{F}_g = 0$ and $\mathbf{F}_c \approx 0$ once axial equilibrium is achieved) only the hydrodynamic force component remains, namely

$$\mathbf{F}_{nb} = \int_{|\mathbf{x}' - \mathbf{x}'_p| = a} \mathbf{n} \cdot \left(-q' \mathbf{I} + \mu \left(\nabla' v' + \nabla' v'^{\,T} \right) \right) \, dS' \,,$$

where $|\mathbf{x}' - \mathbf{x}'_p| = a$ is the surface of the particle, primes denote variables in the rotating reference frame, and $\mathbf{n}$ is the outward pointing normal. Upon non-dimensionalizing for a viscous flow, using the characteristic length a and velocity $U = U_m a/\ell$, one may perform a perturbation expansion of q' and $\mathbf{v}'$ with respect to the particle Reynolds number $\mathrm{Re}_p = (\rho/\mu) U_m a^2/\ell$, which is assumed to be sufficiently small. Notice that particles are expected to quickly approach terminal velocity as determined by Stokes' drag law and, thereafter, Re_p is the effective Stokes number during particle migration. For convenience and since $\bar{\mathbf{u}}_s$ scales

with $U_m\sqrt{K\epsilon} = \mathrm{Re}_p U\kappa$, where

$$\kappa = \ell^4/(4a^3R), \tag{4.2}$$

the secondary component of the background flow velocity is considered to be $\mathcal{O}(\mathrm{Re}_p)$. Consequently, the leading order component of $\mathbf{F}_{nb}$ describes the primary force balance governing the axial velocity of the particle $u_p = d\theta_p/dt$ (and analogously the leading order component of the torque describes the primary balance governing its spin $\mathbf{\Omega}_p$).

The first order component of $\mathbf{F}_{nb}$ describes the forces governing particle migration within the cross-section, specifically the inertial lift $\mathbf{L}$ and secondary flow drag $\mathbf{D}$. The perturbation analysis yields [HLR15]

$$\mathbf{L} \propto \rho U_m^2 a^4/\ell^2 = \mu a U \mathrm{Re}_p \tag{4.3}$$

and, recalling that $\bar{\mathbf{u}}_s \propto \mathrm{Re}_p U\kappa$ and using the Stokes drag law to approximate the secondary drag force, it follows that

$$\mathbf{D} \approx 6\pi\mu a\bar{\mathbf{u}}_s \propto \mu a U \mathrm{Re}_p \kappa\,. \tag{4.4}$$

Therefore, one expects $\mathbf{D} \propto \kappa\mathbf{L}$.

Computational approximations of $\mathbf{L}$ and $\mathbf{D}$ have been previously obtained over several cross-sectional shapes (square, rectangular and trapezoidal), in each case for a number of particle sizes and duct bend radii, including for straight ducts ($R \to \infty$) [HSB19]. A key factor in determining the stability of equilibria and the existence of slow manifolds is the intersection of zero level curves of the r and z components of the net migration force $\mathbf{L} + \mathbf{D}$. Using these, a number of significantly different types of migration dynamics were identified. For rectangular cross-sectional shape in particular, but also for trapezoidal cross-sections, these were found to depend on the value of κ.

Ducts with square cross-sections were less studied in [HSB19] but three different types of migration dynamics were identified, characterized by four stable equilibria, a single stable equilibrium, and a pair of stable limit cycles. In this chapter, we undertake a detailed examination of migration dynamics in ducts with square cross-sectional shapes. For this

purpose, it is desirable to construct a simpler model, which we call the Zero Level Fit (ZeLF) model, which is more tractable for studying the dynamical system of the particle motion in depth.

4.3 Constructing the ZeLF model

The inertial lift $\mathbf{L}$ experienced by the particle is primarily due to the disturbance of the axial flow along the duct. We assume that $\mathbf{L}$ is well approximated by that for the case of flow through a duct with the same cross-section in the limit $R \to \infty$ ($\epsilon \to 0$). To this, we add the effect of drag force $\mathbf{D}$ approximated by the Stokes drag law applied to the secondary velocity field $\bar{\mathbf{u}}_s$ describing the flow vortices in the cross-section that are due to the curvature of the duct also obtained for the limit $\epsilon \to 0$. Specifically, we compute $\hat{\mathbf{u}}_s = \lim_{R\to\infty} \frac{\bar{\mathbf{u}}_s}{U_m\sqrt{K\epsilon}}$ and then subsequently approximate $\bar{\mathbf{u}}_s$ as $\bar{\mathbf{u}}_s \approx U_m\sqrt{K\epsilon}\hat{\mathbf{u}}_s$. A similar model was briefly explored in [Har18], focusing on a duct having a rectangular cross-section and using numerical simulation data to compute the forces; for a sufficiently small ratio of duct height ℓ to bend radius R, the predicted net force driving particle migration was found to be similar to that of the more complex model [HSB19] summarized in the previous section.

However, in contrast to the model of [Har18], here we fit simple model functions to simulation data for a small particle suspended in flow through a curved duct having a square cross-section and use these functions to estimate the force components. Our model functions preserve the topology of the zero level sets for the inertial lift and drag allowing us to retain the correct migration dynamics for ducts with large bend radius. Additionally, the model smooths over some of the numerical noise/error which is present in the simulation data.

A weakness of this modeling approach is that it may not be appropriate for ducts having a smaller bend radius where the curved geometry of the duct has a noticeable influence on both the inertial lift force and the secondary drag force. As the bend radius increases, the influence of the curved geometry on both of these components decays. Therefore our

modeling of both the inertial lift force and secondary drag forces are expected to be most accurate for ducts having a large bend radius compared with the cross-sectional width.

Understanding the axial distance traveled by a particle during migration is crucial to the design of devices for particle focusing and separation. Hence, herein we couple this to the cross-sectional dynamics in a simplified manner. We take the axial velocity of the particle to always be equal to the terminal velocity if it were to remain fixed at its current cross-section location. This is a reasonable assumption because the axial velocity is expected to reach equilibrium on a much faster time scale than that of the cross-sectional migration. Further, since the axial velocity of the particle (at equilibrium) is similar to that of the background flow (there is a small 'slip' but it is order $(a/\ell)^2$) then this may be approximated by $\bar{\mathbf{u}}_a(r_p, z_p)$. Similar to $\bar{\mathbf{u}}_s$, we approximate $\bar{\mathbf{u}}_a$ with a simple model function for the limit $\epsilon \to 0$.

In the remainder of the chapter we describe our model non-dimensionalising the cross-sectional coordinates according to

$$(r, z) = \left(\frac{\ell}{2}\tilde{r}, \frac{\ell}{2}\tilde{z}\right) . \tag{4.5}$$

This is most convenient because the rescaled cross-sectional domain $(\tilde{r}, \tilde{z}) \in [-1, 1] \times [-1, 1]$ is independent of any physical parameters (in contrast to scaling with respect to the particle radius a for which the non-dimensionalized duct dimensions are ℓ/a).

The following subsections outline the construction of the different model components before describing how they are assembled for the computation of particle trajectories.

4.3.1 Modeling the inertial lift force

We first give the model for the inertial lift acting on a particle and then discuss its derivation. The dimensionless component of lift in the r direction within the cross-section, for a particle

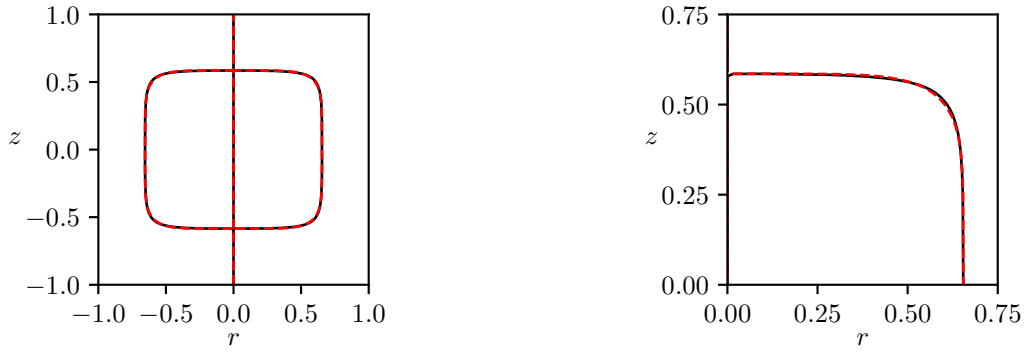

(a) The zero level set curve of L_r

(b) Zoom of the zero level set curve of L_r

Figure 4.2: Fit of the zero level set curve of $f(\tilde{r},\tilde{z}) = \tilde{r}(1 - 12.7\tilde{r}^6 - 24.8\tilde{z}^6)$ (in red) with that of $\tilde{L}_r$ from finite element computations from [HSB19] (in black). Figure (a) shows the two over the entire cross-section whereas figure (b) zooms into a portion of the upper right quadrant. The difference between the two is difficult to discern at both scales.

with position $(\tilde{r}_p, \tilde{z}_p) = (\tilde{r},\tilde{z})$, is approximated by

$$\hat{L}_r(\tilde{r},\tilde{z}) = \tilde{r}\left(1 - 12.7\tilde{r}^6 - 24.8\tilde{z}^6\right)\exp\left(2.95 - 1.43\tilde{r}^2 - 4.23\tilde{z}^2 - 1.98\tilde{r}^4 \right.$$
$$\left. +5.28\tilde{r}^2\tilde{z}^2 - 1.10\tilde{z}^4 + 2.35\tilde{r}^6 - 1.16\tilde{r}^4\tilde{z}^2 - 7.16\tilde{r}^2\tilde{z}^4 + 3.51\tilde{z}^6\right). \quad (4.6)$$

Similarly, because of the expected symmetry for a straight duct with square cross-section, the component in the z direction is approximated as

$$\hat{L}_z(\tilde{r},\tilde{z}) = \hat{L}_r(\tilde{z},\tilde{r}).$$

In the dimensional setting these two inertial lift force components are

$$L_r, L_z = \rho U_m^2 \frac{a^4}{\ell^2}\hat{L}_r, \rho U_m^2 \frac{a^4}{\ell^2}\hat{L}_z\,.$$

The inertial lift force model was constructed as follows. First the factor preceding the exponential in $\hat{L}_r$, $f(\tilde{r},\tilde{z}) = \tilde{r}(1 - 12.7\tilde{r}^6 - 24.8\tilde{z}^6)$, was determined by trial and error to give a good match between its zero level contour and the zero level contour of an interpolation of L_r data computed via numerical simulations for a small particle (specifically with $a/\ell = 1/20$)

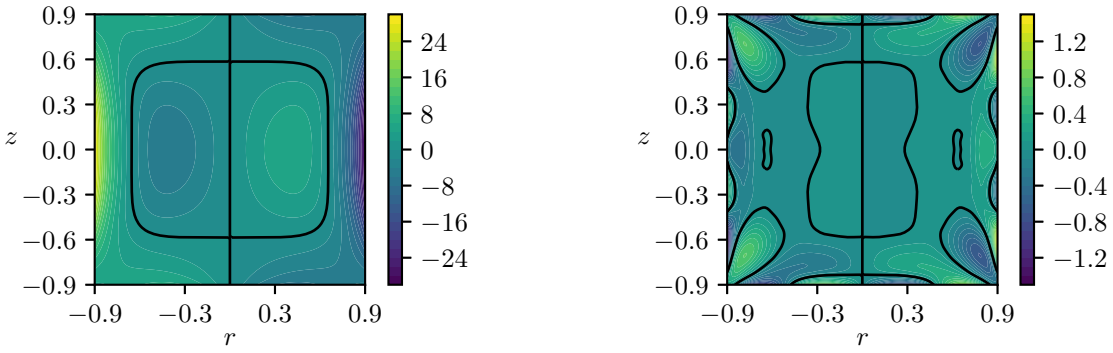

(a) Inertial lift model $\hat{L}_r$

(b) Error of $\hat{L}_r$

Figure 4.3: Model of the inertial lift force $\hat{L}_r(\tilde{r}, \tilde{z})$: (a) $\hat{L}_r$ over the cross-section excluding a small region around the walls; (b) the difference between the model and results computed from finite element solutions [HSB19].

in a straight duct as described in [HSB19]; see Figure 4.2. This ensures the prediction of the correct location and stability of equilibria for a straight duct. The exponential factor, with exponent consisting of a polynomial in $\tilde{r}, \tilde{z}$, was then added to improve the global accuracy of the model in a way that does not modify the zero level contours. The coefficients of the polynomial (in the exponent) were obtained via a constrained least squares fitting to the interpolation of the L_r data from the numerical simulations. There is a classical trade-off between accuracy and simplicity of the model in determining a suitable degree of the polynomial within the exponent. Compared with the simulation data, the specific model (4.6) achieves a L_2 relative error of 3.8%, see Figure 4.3.

4.3.2 Modeling the secondary drag force

The secondary drag force on the particle is approximated by combining Stokes' drag law with the velocity of the secondary component of the fluid flow through a curved duct in the limit $\epsilon \to 0$. The secondary component consists of two counter-rotating vortices which are orthogonal to the main direction of flow. For a slow laminar flow through a curved duct,

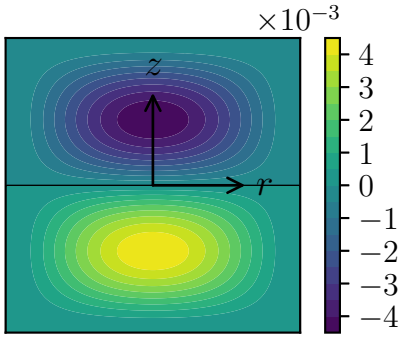

(a) Stream-function model Φ_1

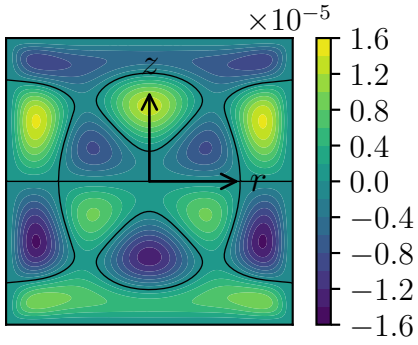

(b) Error of Φ_1

Figure 4.4: Model of the secondary vortices: (a) streamfunction $\Phi_1(r, z)$ and (b) the difference between $\Phi_1(r, z)$ and the streamfunction from a finite difference computation over the cross-section in the limit $\epsilon \to 0$.

it can be shown that the velocity of the secondary component scales as $U_m\sqrt{K\epsilon} = \epsilon \mathrm{Re}_c U_m$ [Har19, HSB19]. The two velocity components can be described via a stream-function $\Phi(\tilde{r}, \tilde{z})$, specifically with $-\partial\Phi/\partial\tilde{z}$ and $\partial\Phi/\partial\tilde{r}$ describing the velocity in the $\tilde{r}$ and $\tilde{z}$ directions, respectively.

The fundamental scale and topology of Φ is approximated as

$$\Phi_0(\tilde{r}, \tilde{z}) = -0.01591\epsilon \mathrm{Re}_c U_m (1 - \tilde{r}^2)^2 \tilde{z} (1 - \tilde{z}^2)^2 \,.$$

This approximation ensures that both $-\partial\Phi/\partial\tilde{z}$ and $\partial\Phi/\partial\tilde{r}$ are zero on the duct walls, describes two counter rotating vortices with the correct orientation, has the desired odd symmetry with respect to $\tilde{z}$, and has even symmetry with respect to $\tilde{r}$ as required in the limit $\epsilon \to 0$. The factor 0.01591 was determined to fit the velocity fields obtained from a finite difference solution of the Navier–Stokes equations governing the background flow in the limit $\epsilon \to 0$ and at small flow rate.

The accuracy of the secondary velocity approximation can be improved with the addition

of further terms. We have performed an L_2 fit of the model

$$\Phi_N(\tilde{r},\tilde{z}) = \Phi_0(\tilde{r},\tilde{z})\sum_{n=0}^{N}\sum_{i=0}^{n}\beta_{2i,2(n-i)}\tilde{r}^{2i}\tilde{z}^{2(n-i)},$$

for $N \in \mathbb{N}$, to the stream-function computed from the above mentioned finite difference solution of the Navier–Stokes equations. Fits were determined for several N but $N = 1$ was found to be sufficiently accurate for our study. In particular, we obtained

$$\Phi_1(\tilde{r},\tilde{z}) = \Phi_0(\tilde{r},\tilde{z})(0.9833 + 0.2289\tilde{r}^2 - 0.0178\tilde{z}^2)$$

where the coefficients have been rounded to four decimal places. A plot of the approximation Φ_1 is shown in Figure 4.4 alongside a plot of the error with respect to the finite-difference solution. The relative error of Φ_1 is found to be 0.3% making it sufficiently accurate for the study of dynamics herein.

For a small spherical particle, the drag force within the cross-sectional plane can be estimated using Stokes' drag law in conjunction with the velocities obtained from the stream-function Φ_1. Specifically, for a small particle suspended in the flow and which is not moving with respect to the $\tilde{r},\tilde{z}$ coordinates, one can use the approximation

$$D_r, D_z = -6\pi\mu a\frac{\partial\Phi_1}{\partial\tilde{z}}, 6\pi\mu a\frac{\partial\Phi_1}{\partial\tilde{r}}$$

for the radial and vertical components of the drag force respectively. Taking the scaling of Φ_1 into account, it is reasonable to non-dimensionalize the secondary drag force according to

$$\begin{aligned} D_r,\, D_z &= \mu a\epsilon\Re_c U_m\tilde{D}_r,\, \mu a\epsilon\Re_c U_m\tilde{D}_z \\ &= \rho U_m^2\frac{a\ell^2}{4R}\tilde{D}_r,\, \rho U_m^2\frac{a\ell^2}{4R}\tilde{D}_z\,. \end{aligned}$$

It is important to note that this approximation will not be accurate when the particle is very close to a wall, or for larger particles. The true drag coefficient is larger for increasing particle size, and additionally the drag coefficient increases when the particle approaches a wall. Since our interest is primarily smaller particles and their dynamics away from the walls we stick with Stokes' drag law to maintain the simplicity of the model.

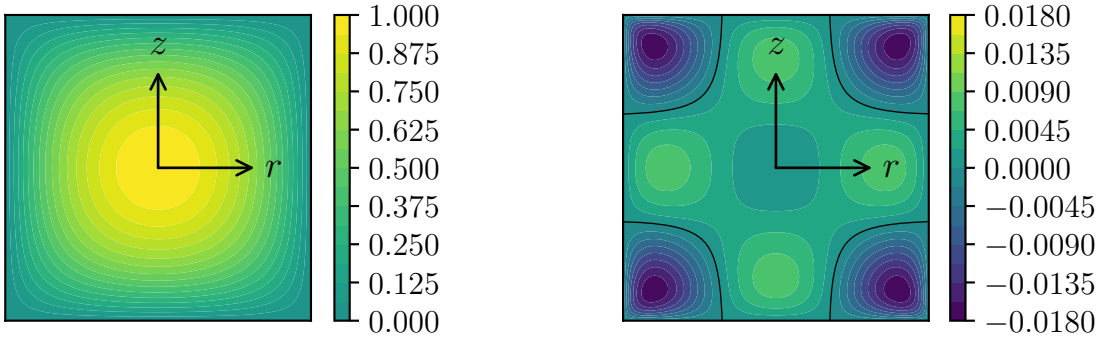

(a) Axial velocity model u_1

(b) Error of u_1

Figure 4.5: (a) Model function for the axial velocity $u_1(\tilde{r}, \tilde{z})/U_m$ and (b) the difference between this and a finite difference computation of Poiseuille flow through a straight square duct with unit wall length.

4.3.3 Modeling the axial velocity

The particle travels with an axial velocity which is close to that of the background fluid flow. For a slow laminar fluid flow through a curved square duct (with no particles), the axial velocity field is quite close to Poiseuille flow in a straight square duct, specifically within $O(\epsilon)$. With U_m denoting the maximum axial velocity, then a simple approximation of the dimensionless Poiseuille flow is given by

$$u_0(\tilde{r}, \tilde{z}) = U_m(1 - \tilde{r}^2)(1 - \tilde{z}^2)\,. \tag{4.7}$$

This approximation attains the expected maximum, satisfies no-slip boundary conditions on the walls, and has the even symmetry with respect to r and z that is expected for this flow.

The accuracy of the simple approximation (4.7) degrades away from the wall and the center, and can be improved by the addition of further terms in a similar manner to that used above for the streamfunction. Thus, we perform a simple L_2 fit of the model

$$u_N(\tilde{r}, \tilde{z}) = u_0(\tilde{r}, \tilde{z}) \left(1 + \sum_{n=1}^{N} \sum_{i=0}^{n} \alpha_{2i,2(n-i)} \tilde{r}^{2i} \tilde{z}^{2(n-i)} \right), \tag{4.8}$$

for a given $N \in \mathbb{N}$, with an axial velocity field computed from a finite difference solution of Poiseuille flow in a straight duct. The general form (4.8) retains all of the features of u_0 described above but provides a better approximation for increasing N. We constructed approximations for several N but here too found that $N = 1$ was sufficiently accurate for our study. Specifically, we obtained

$$u_1(\tilde{r}, \tilde{z}) = u_0(\tilde{r}, \tilde{z}) \left(1 + 0.1818(\tilde{r}^2 + \tilde{z}^2)\right),$$

where the coefficient has been rounded to four decimal places. A plot of the approximation u_1 is shown in Figure 4.5 alongside a plot of the error $u_1 - u_a$ (both scaled with U_m) where $u_a = \lim_{R\to\infty} \bar{\mathbf{u}}_a \cdot \mathbf{e}_\theta$, i.e. the axial flow through a straight square duct. The relative error $\|u_1 - u_a\|_2 / \|u_a\|_2$ is found to be 1.1% making u_1 sufficiently accurate for the study of dynamics herein. The terminal velocity of a particle is thus approximated as

$$u_p \approx u_1(r_p, z_p).$$

4.3.4 Putting the model together

We now approximate the net force on the particle in the r, z directions as

$$F_r = L_r + D_r, \quad F_z = L_z + D_z,$$

respectively. If we non-dimensionalize F_r, F_z with the same scale as L_r, L_z, that is

$$F_r = \rho U_m^2 a^4 / \ell^2 \hat{F}_r, \quad F_z = \rho U_m^2 a^4 / \ell^2 \hat{F}_z,$$

then we obtain

$$\hat{F}_r = \hat{L}_r + \kappa \tilde{D}_r, \quad \hat{F}_z = \hat{L}_z + \kappa \tilde{D}_z,$$

with $\kappa = \ell^4/(4a^3 R)$ as defined in (4.2). This highlights the fact that κ describes the magnitude of the secondary drag force relative to the inertial lift force.

Using Stokes' drag law, the terminal velocity of a small particle due to the net migration force is

$$v_r = \frac{F_r}{6\pi\mu a} = \frac{L_r + D_r}{6\pi\mu a}, \quad v_z = \frac{F_z}{6\pi\mu a} = \frac{L_z + D_z}{6\pi\mu a}.$$

In this study, it will be convenient to non-dimensionalize these velocities according to the secondary fluid velocity scale (rather than a scaling based on the inertial lift force). This is because we generally expect the secondary flow to be the dominant effect for a small particle and the inertial lift force can be viewed as a perturbation to this. In particular, we introduce

$$v_r = \epsilon \mathrm{Re}_c U_m \tilde{v}_r \,, \quad v_z = \epsilon \mathrm{Re}_c U_m \tilde{v}_z \,.$$

Consequently, we express $\tilde{v}_r, \tilde{v}_z$ as

$$\tilde{v}_r = \frac{1}{6\pi}\left(\frac{\hat{L}_r}{\kappa} + \tilde{D}_r\right) \,, \quad \tilde{v}_z = \frac{1}{6\pi}\left(\frac{\hat{L}_z}{\kappa} + \tilde{D}_z\right) \,.$$

Then, the trajectory of a particle with center $(\tilde{r}_p, \tilde{z}_p)$ is modeled via the first order system of ordinary differential equations

$$\frac{d\tilde{r}_p}{d\tilde{t}} = \tilde{v}_r\left(\tilde{r}_p, \tilde{z}_p\right) \,, \tag{4.9a}$$

$$\frac{d\tilde{z}_p}{d\tilde{t}} = \tilde{v}_z\left(\tilde{r}_p, \tilde{z}_p\right) \,, \tag{4.9b}$$

where $\tilde{t}$ is dimensionless time, related to physical time t by $t = R\tilde{t}/(U_m \mathrm{Re}_c)$.

Observe that our model of particle migration depends only on the cross-sectional coordinate $(\tilde{r}_p, \tilde{z}_p)$ and is independent of the current angular location within the curved duct θ_p. In order to study how far a particle travels through the curved duct over the time scale at which inertial migration takes place it is necessary to re-incorporate the axial motion into the model. In practice, particles lag slightly from the surrounding fluid velocity. However, for a small particle, this lag is sufficiently small that it is reasonable to take the background fluid velocity at the particle center as an approximation of the particle's axial velocity. Therefore, we can incorporate this into our system of ordinary differential equations (4.9) by adding

$$\frac{d\tilde{s}_p}{d\tilde{t}} = \frac{d}{d\tilde{t}}(\mathrm{Re}_c \theta_p) = \frac{1}{(1+\epsilon\tilde{r}_p)} \frac{u_1\left(\tilde{r}_p, \tilde{z}_p\right)}{U_m} \,, \tag{4.10}$$

where θ_p tracks the angular coordinate of the particle in the curved duct and $\tilde{s}_p = \mathrm{Re}_c \theta_p$ is the corresponding dimensionless arc-length along the central axis of the channel that is

related to the physical arc length $s_p = R\theta_p$ by

$$\tilde{s}_p = \frac{\mathrm{Re}_c}{R} s_p \,. \tag{4.11}$$

We refer to $\tilde{s}_p$ as the distance the particle has travelled down the channel, where $\theta_p(0) = \tilde{s}_p(0) = 0$. Finally, in keeping with the assumption made in developing this model, we take the $\epsilon \to 0$ limit of (4.10).

To summarise, the complete ZeLF model is described by the first-order system of ordinary differential equations, involving just the single dimensionless parameter κ,

$$\begin{aligned}
\frac{d\tilde{r}_p}{d\tilde{t}} = \frac{1}{6\pi\kappa}\tilde{r}_p\left(1 - 12.7\tilde{r}_p^6 - 24.8\tilde{z}_p^6\right)\exp\big(2.95 - 1.43\tilde{r}_p^2 - 4.23\tilde{z}_p^2 - 1.98\tilde{r}_p^4 \qquad &(4.12a)\\
+5.28\tilde{r}_p^2\tilde{z}_p^2 - 1.10\tilde{z}_p^4 + 2.35\tilde{r}_p^6 - 1.16\tilde{r}_p^4\tilde{z}_p^2 - 7.16\tilde{r}_p^2\tilde{z}_p^4 + 3.51\tilde{z}_p^6\big)\\
+ 0.01591(1-\tilde{r}_p^2)^2(1-\tilde{z}_p^2)\big(0.9833 + 0.2289\tilde{r}_p^2\\
- 4.9699\tilde{z}_p^2 - 1.1445\tilde{r}_p^2\tilde{z}_p^2 + 0.1246\tilde{z}_p^4\big)\,,\\
\frac{d\tilde{z}_p}{d\tilde{t}} = \frac{1}{6\pi\kappa}\tilde{z}_p\left(1 - 24.8\tilde{r}_p^6 - 12.7\tilde{z}_p^6\right)\exp\big(2.95 - 4.23\tilde{r}_p^2 - 1.43\tilde{z}_p^2 - 1.10\tilde{r}_p^4 \qquad &(4.12b)\\
+5.28\tilde{r}_p^2\tilde{z}_p^2 - 1.98\tilde{z}_p^4 + 3.51\tilde{r}_p^6 - 7.16\tilde{r}_p^4\tilde{z}_p^2 - 1.16\tilde{r}_p^2\tilde{z}_p^4 + 2.35\tilde{z}_p^6\big)\\
+ 0.01591\tilde{r}_p(1-\tilde{r}_p^2)\tilde{z}_p(1-\tilde{z}_p^2)^2\big(3.4754 + 1.3734\tilde{r}_p^2 - 0.0712\tilde{z}_p^2\big)\,,\\
\frac{d\tilde{s}_p}{d\tilde{t}} = \big(1 + 0.1818(\tilde{r}_p^2 + \tilde{z}_p^2)\big)\,(1-\tilde{r}_p^2)(1-\tilde{z}_p^2)\,. \qquad &(4.12c)
\end{aligned}$$

Results from this model are straightforward to translate from dimensionless to dimensional coordinates as needed.

4.4 Results of the ZeLF model

In this section, we investigate particle motion and its dependence on κ using the ZeLF model. Figure 4.6 illustrates the migration of particles via five snapshots in time for three distinct κ values. The particles migrate towards a single fixed point ($\kappa = 25$), one of multiple fixed points ($\kappa = 1$) or to a stable orbit ($\kappa = 200$). The particle color indicates the dimensionless distance $\tilde{s}_p$ traveled down the channel by the particle.

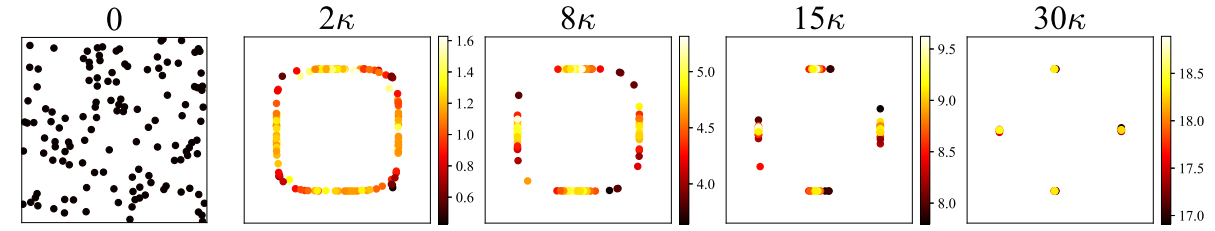

(a) $\kappa = 1$

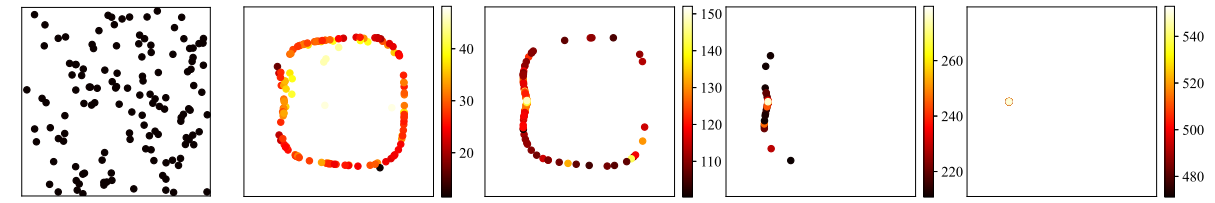

(b) $\kappa = 25$

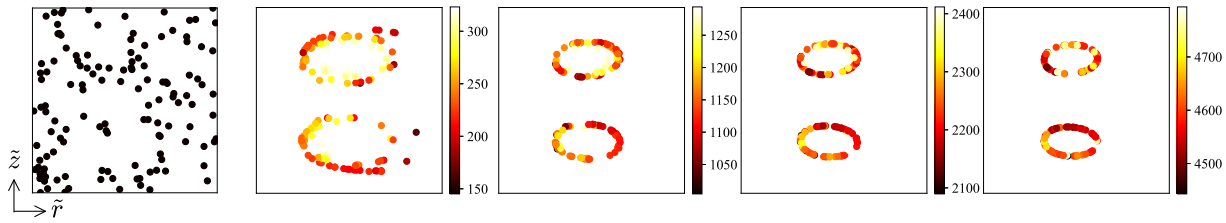

(c) $\kappa = 200$

Figure 4.6: Cross-sectional positions of 128 particles, initially randomly distributed within the cross-section, $[-1, 1]^2$. Each snapshot of the cross-section corresponds from left to right to the time $\tilde{t} = 0, 2\kappa, 8\kappa, 15\kappa$, and 30κ, and from top to bottom (a) small, (b) intermediate, and (c) large κ. The color scheme shows the axial distance each particle has traveled, calculated by (4.12c).

We observe three distinct behaviors, here termed "multi-focus", "unique-focus" and "periodic orbit", corresponding to κ small ($\kappa \lesssim 10$), intermediate ($10 \lesssim \kappa \lesssim 25$), and large ($\kappa \gtrsim 25$). Since we are interested in the long term behavior of the particles we only discuss the long-time limit sets (ω-limit sets [GH13]). The limit sets are composed of equilibria, which are classified as stable nodes or foci, saddle points, and unstable nodes by their eigenvalues,

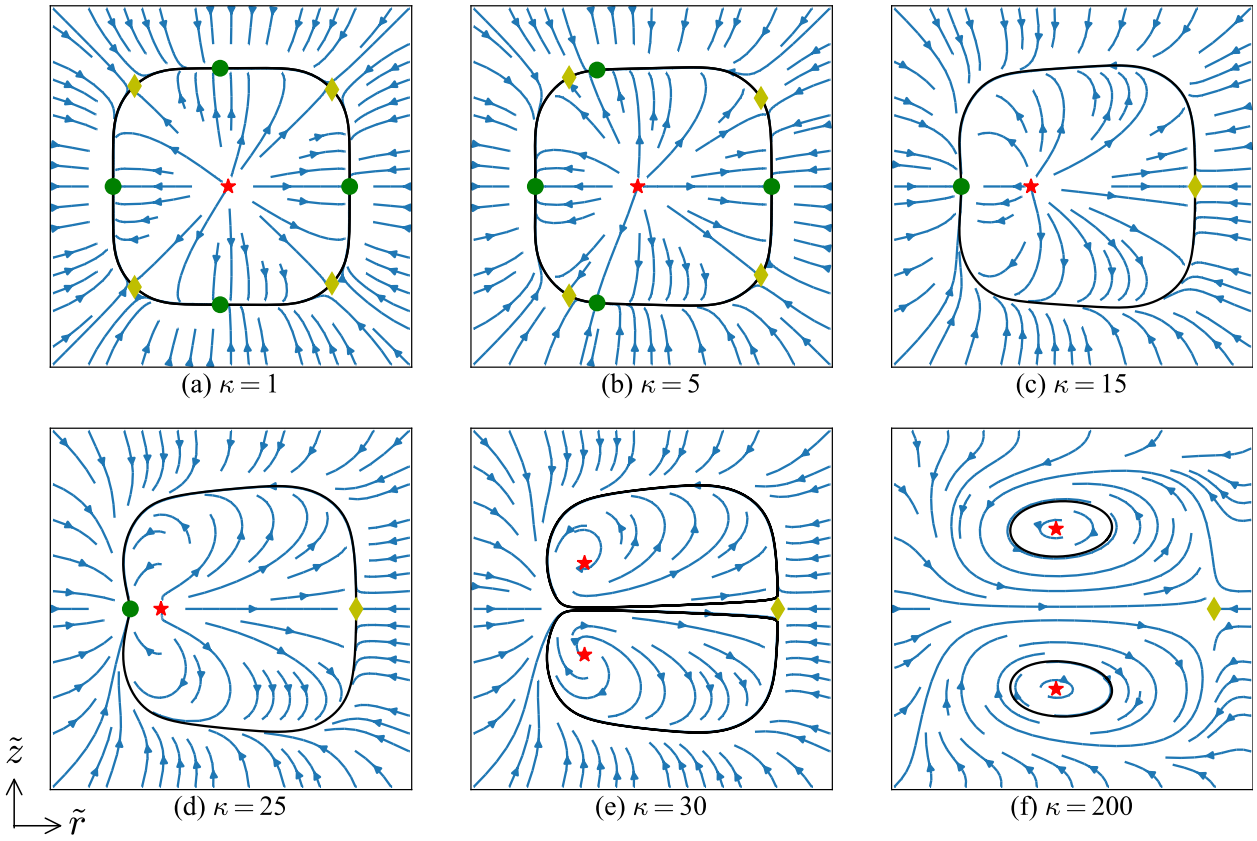

Figure 4.7: Particle trajectories for different κ values within the cross-section, $[-1, 1] \times [-1, 1]$. The equilibria are in different colors and shapes: stable nodes (green $\bullet$), saddle points (yellow $\diamondsuit$) and unstable nodes (red $\star$). For $\kappa \leq 25$, the black line represents the heteroclinic orbit that connects the saddle to the stable equilibria. For $\kappa \geq 30$, the black line represents the limit cycle.

and limit cycles, also classified as either stable or unstable by their Poincaré map.

4.4.1 Multi-focus behavior - small κ

For small κ, there are multiple stable nodes or focusing points near the center of each side of the cross-section, multiple saddle points near the corners of the cross-section, and one unstable node in the middle (Figure 4.7ab). For each saddle point, there is a heteroclinic orbit that

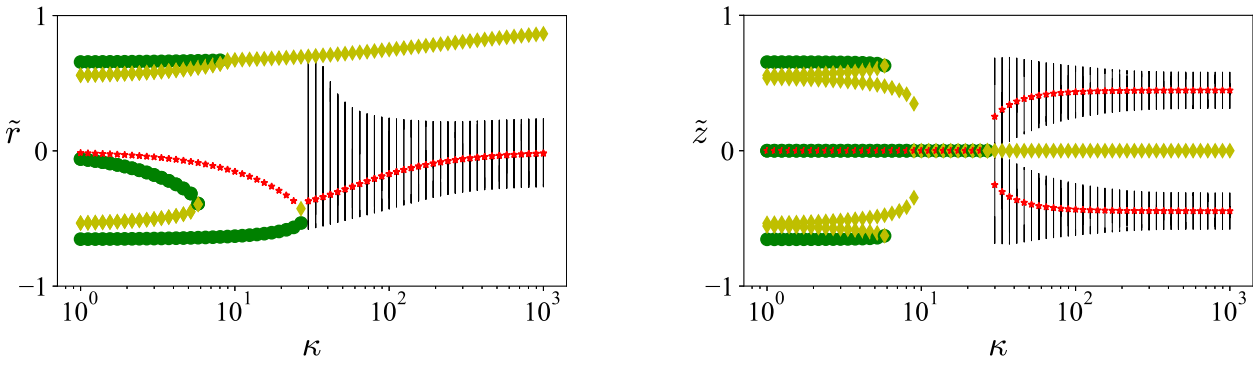

(a) κ-$\tilde{r}$ position

(b) κ-$\tilde{z}$ position

Figure 4.8: Equilibrium positions and the limit cycle range as a function of κ. The equilibria are in different colors and shapes: stable nodes (green •), saddle points (yellow ♢) and unstable nodes (red ⋆). The range of the limit cycles are shown in black vertical lines.

connects to a stable node which acts as a slow manifold. The particles quickly migrate onto one of these heteroclinic orbits, and then slowly converge to the stable node (Figure 4.6a). Therefore, the migration velocity of the particle on the slow manifold determines the time needed for the particles to converge to the stable nodes. These particle trajectories are similar to those in a straight duct which is expected since as $R \to \infty$, $\kappa \to 0$ [HSB19, HKD16].

4.4.2 Unique focus behavior - intermediate κ

As κ increases the system undergoes saddle-node bifurcation as the stable node and saddle point in each of the upper and lower halves of the duct merge and disappear. Simultaneously a (subcritical) pitchfork bifurcation happens as two saddle points and one stable node on the outer side (right side) merge and become a saddle point (Figure 4.8). This results in a system with a unique stable equilibrium point that attracts all particles in the duct (Figure 4.7cd). All equilibria lie on the $\tilde{r}$-axis, due to the vertical reflection symmetry, with the stable node on the inner side (left side) of the duct. Similar to the multi-focus behavior, there exist heteroclinic orbits that connect the saddle to the stable node which act as a slow manifold

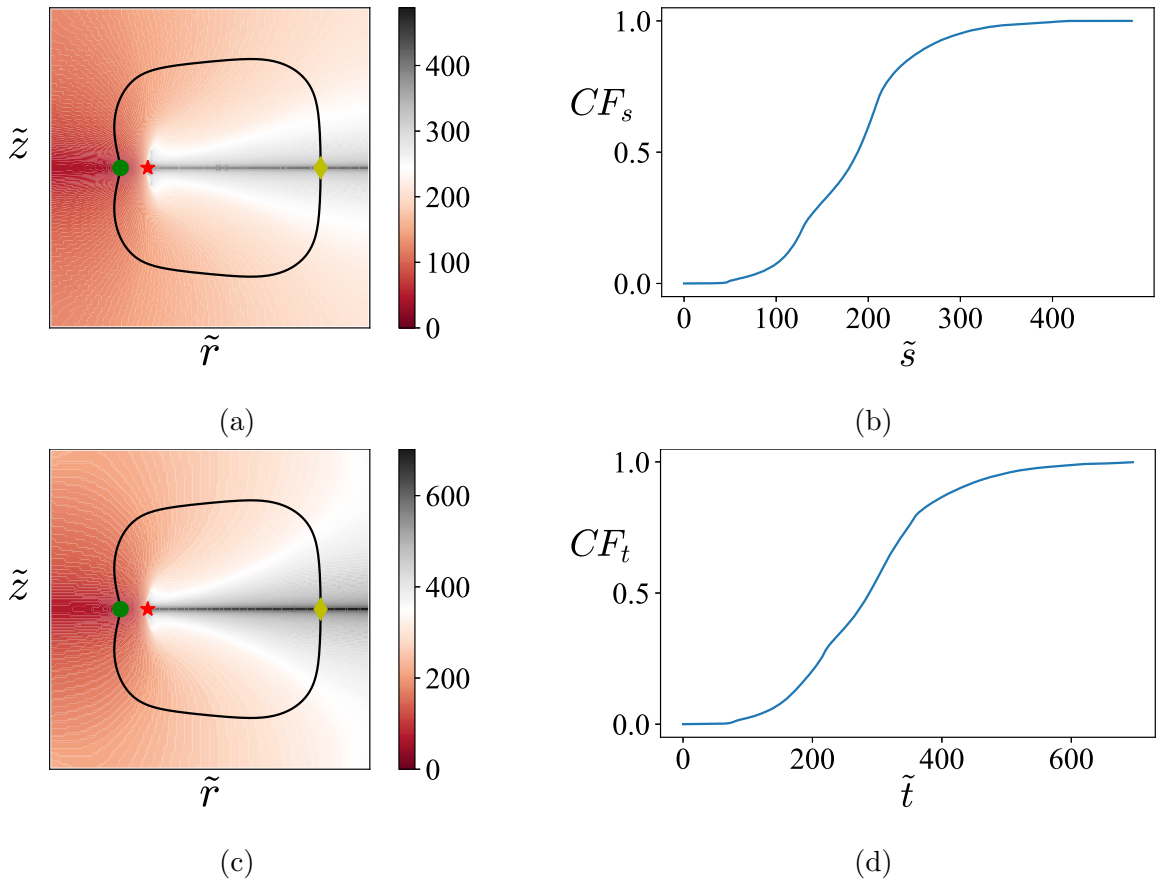

Figure 4.9: On the left are heat maps of the cross-section, $[-1,1] \times [-1,1]$, that show the (a) axial distance $\tilde{s}_p^*$ and (c) time $\tilde{t}^*$, defined in (4.13), required to focus from a position in the cross-section to the stable equilibrium point for $\kappa = 25$. The equilibria are shown in different colors and shapes: stable nodes (green $\bullet$), saddle points (yellow $\diamondsuit$) and unstable nodes (red $\star$). The black solid line represents the heteroclinic orbit connecting the saddle to the stable node. On the right, the graphs show (b) CF_s versus $\tilde{s}$ and (d) CF_t versus $\tilde{t}$ as defined in (4.14), i.e. the fraction of the cross-sectional area from which particles have focused within the given distance $\tilde{s}$ and time $\tilde{t}$.

(Figure 4.6b).

The axial distance and time required for particles to focus on this equilibrium point are important since they determine the length and run time of the apparatus to achieve particle

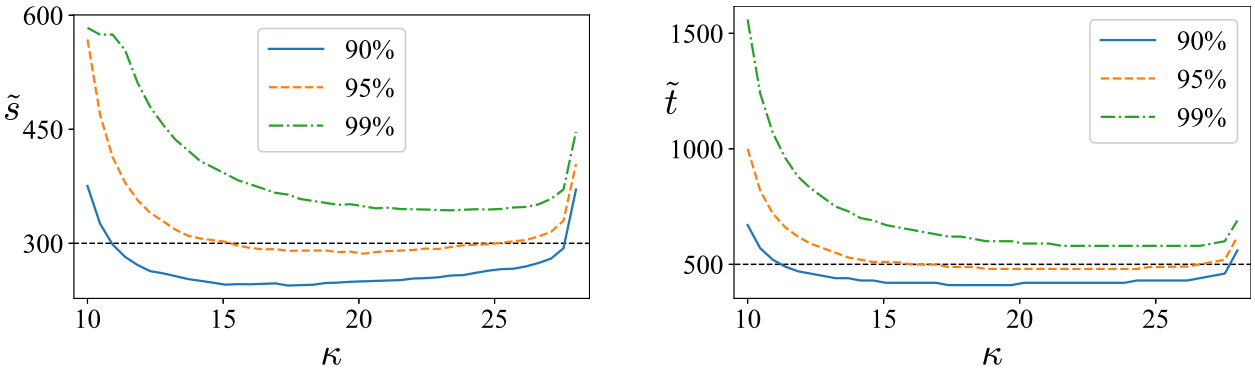

(a) (b)

Figure 4.10: (a) axial distance $\tilde{s}$ and (b) time $\tilde{t}$ required for 90% (blue), 95% (red), 99% (green) of the particles to focus to the equilibrium for intermediate κ. The dashed horizontal line indicates the distance and time at which approximately 95% of particles with $15 \leq \kappa \leq 25$ are focused.

focusing. Technically, if a particle does not start on the stable equilibrium point $(\tilde{r}^*, \tilde{z}^*)$ it will take infinite time to arrive at the exact equilibrium point. However, we consider that a particle has "focused" at the equilibrium point if the distance from the particle to the equilibrium is smaller than a certain threshold, which we choose to be 0.01 for this chapter. We define

$$\tilde{t}^*(\tilde{r}, \tilde{z}) = \min\left\{\tilde{t} : \left\|(\tilde{r}_p, \tilde{z}_p)(\tilde{t}) - (\tilde{r}^*, \tilde{z}^*)\right\| < 0.01,\ (\tilde{r}_p, \tilde{z}_p)(0) = (\tilde{r}, \tilde{z})\right\}, \tag{4.13a}$$

$$\tilde{s}_p^*(\tilde{r}, \tilde{z}) = \tilde{s}_p(\tilde{t}^*(\tilde{r}, \tilde{z})), \tag{4.13b}$$

which correspond to the required time and axial distance for a particle at an initial position $(\tilde{r}, \tilde{z})$ in the cross-section to focus. The heat maps in Figure 4.9ac show, $\tilde{s}_p^*$ and $\tilde{t}^*$ over the cross-section for $\kappa = 25$. In each map, black shows the region from which the focusing distance or time is greatest, and dark red shows the region from which the focusing distance or time is shortest.

In order to understand the overall focusing ability in a given axial length or time, we compute the fraction of the channel cross-section area from which particles will have focused

in distance $\tilde{s}$ or time $\tilde{t}$. We define these functions $CF_s(\tilde{s})$ and $CF_t(\tilde{t})$, respectively, as:

$$CF_s(\tilde{s}) = \frac{1}{4}\int_{-1}^{1}\int_{-1}^{1} \chi_{\tilde{s}_p^* \le \tilde{s}}(\tilde{r},\tilde{z}) d\tilde{r} d\tilde{z}, \tag{4.14a}$$

$$CF_t(\tilde{t}) = \frac{1}{4}\int_{-1}^{1}\int_{-1}^{1} \chi_{\tilde{t}^* \le \tilde{t}}(\tilde{r},\tilde{z}) d\tilde{r} d\tilde{z}, \tag{4.14b}$$

where $\chi_{\tilde{s}_p^* \le \tilde{s}}$ and $\chi_{\tilde{t}^* \le \tilde{t}}$ are characteristic functions with unit value where $\tilde{s}_p^*(\tilde{r},\tilde{z}) \le \tilde{s}$ and $\tilde{t}^*(\tilde{r},\tilde{z}) \le \tilde{t}$, respectively, and which are zero elsewhere. Assuming that the particles are initially randomly distributed in the cross-section, CF_s and CF_t give good approximations of the fraction of particles focused after a given distance $\tilde{s}$ and time $\tilde{t}$. Figure 4.9bd plot $CF_s(\tilde{s})$ and $CF_t(\tilde{t})$ for $\kappa = 25$. We observe that the plots of CF_s and CF_t are qualitatively similar. This is due to the fact that the change of axial velocity is relatively slow and smooth over the slow manifold.

For engineering design one needs to know the duct length/number of turns of the spiral the duct length required for the majority (e.g. 95%) of particles to focus. This corresponds to finding $\tilde{s}$ satisfying $CF_s(\tilde{s}) = f$, where f is the fraction of particles focused. Figure 4.10 shows for $10 \le \kappa \le 28$ the axial distance and time required for 90, 95, and 99% of the particles to focus. There is only weak dependence on κ for a significant portion of this range. These plots show that a given duct geometry may be used to focus a range of particle sizes. For example, from Figure 4.10a, we see that a duct of length $\tilde{s} = 300$ will focus at least 95% of particles corresponding to $15 \le \kappa \le 25$. Once we know the duct length we can estimate how many turns of the spiral required for the focusing. Note that the bend radius is not constant along the spiral however the duct width is much smaller than the bend radius, allowing for small variation in the bend radius in real devices (see e.g. Fig. 4.1b). As an example, using physical parameters in [RSR17, WKW16] the number of rotations corresponding to $\tilde{s} = 300$ is approximately 4 and 1-5, respectively. We note that the duct cross-sections used in the experiments are rectangular rather than square. Still this suggests that only a modest number of turns may be needed to achieve the desired focusing. Then, since the particle radius is $a = G/\kappa^{1/3}$, where $G = (\ell^4/4R)^{1/3}$ captures the other geometrical parameters of the

duct, at least 95% of all particles of size

$$0.34G \approx G/25^{1/3} \leq a \leq G/15^{1/3} \approx 0.41G$$

will focus after passing through the duct. From Figure 4.10b we see that this focusing takes a time $\tilde{t} \approx 500$. Differences in the size of particles results in different focusing points and, hence, particle separation by size. In practice, there needs to be a significant separation, within the cross section, between focusing positions (as a function of particle size) for effective separation. For example, in Figure 4.8a, the variation in the radial coordinate is not large so that separation may be difficult. In general, for square ducts, the focusing position may not have sufficient variation and other cross-sectional shapes may be preferred as discussed in [HSB19]. An analysis similar to this work could be carried out for different cross-sections.

4.4.3 Periodic orbit behavior - large κ

As κ increases further, the system undergoes two bifurcations as the stable and unstable nodes on the $\tilde{r}$-axis collide and give birth to an unstable node on either side of the $\tilde{r}$-axis (Figure 4.11a). For κ between 25 and 25.5, there exists a vertical pitchfork bifurcation where the unstable node bifurcates to a pair of unstable nodes and a saddle point between them. For κ between 27.5 and 28.5, there exists a horizontal saddle-node bifurcation where the saddle point and the stable node cancel out each other. Since $d\tilde{z_p}/d\tilde{t} = 0$ on the $\tilde{r}$-axis, the latter bifurcation is determined by $d\tilde{r_p}/d\tilde{t}$ on the axis, which is shown in Figure 4.11b. After the two bifurcations occur, there remains two periodic periodic orbits on either side of the $\tilde{r}$-axis, each around one of the unstable nodes (Figure 4.7e). For $\kappa = 30$, the periodic orbits are large with varying particle speeds, slower near the saddle point and where the saddle-node bifurcation occurs. As κ increases the periodic orbits become smaller and the particle speed becomes more uniform as they effectively follow the Dean flow (Figure 4.7f, and 4.8).

These periodic orbits are attractive limit cycles that are unique on each half domain, as shown by calculating the Poincaré map [GH13]. We choose the manifold that defines the

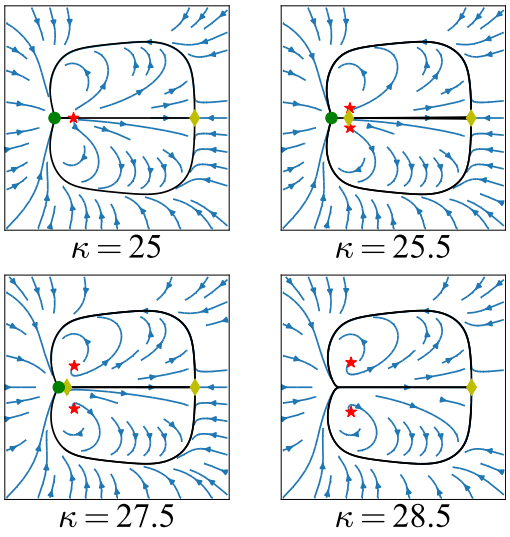

(a) Particle trajectories and equilibria

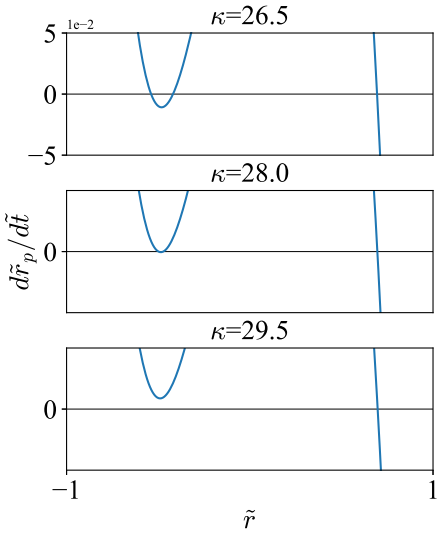

(b) $d\tilde{r_p}/d\tilde{t}$ on the $\tilde{r}$ axis

Figure 4.11: The two bifurcations between $\kappa = 25$ and 30 within the cross-section, $[-1, 1] \times [-1, 1]$. (a) presents the particle trajectories and the equilibria in different colors and shapes: stable nodes (green $\bullet$), saddle points (yellow $\diamondsuit$) and unstable nodes (red $\star$). For $\kappa \leq 28$, the black line represents the heteroclinic orbit that connects the equilibria on the $\tilde{r}$ axis. For $\kappa = 28.5$, the black line represents the limit cycle. (b) are graphs of $d\tilde{r_p}/d\tilde{t}$ on the $\tilde{r}$ axis for $28 \leq \kappa \leq 28.2$

Poincaré map as the vertical line through the unstable equilibrium point in the top half of the duct (Figure 4.12b) and define the Poincaré map $P : (0, 1) \to (0, 1)$ taking as input the $\tilde{z}$-coordinate of a particle on the manifold and yielding as output the $\tilde{z}$-coordinate of that particle after a full rotation around the unstable equilibrium. Figure 4.12a shows the $P(\tilde{z}) - \tilde{z}$ value for the variable $\tilde{z}$. There are three zeros of the function, the middle one corresponding to the unstable node of the system and the other two corresponding to the limit cycle. The sign on either side of the zeros indicates that this limit cycle is attractive.

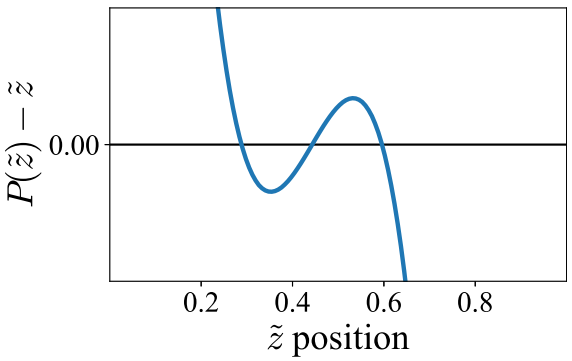

(a) Poincare map for $\kappa = 200$

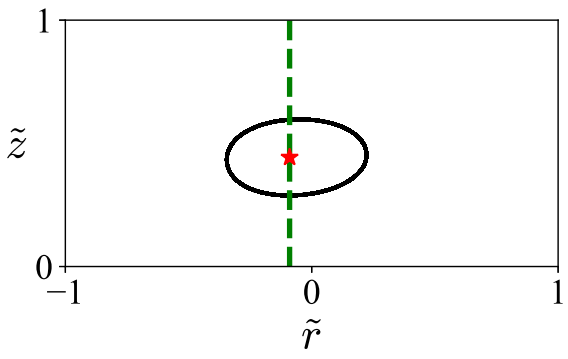

(b) Limit cycle and the manifold

Figure 4.12: The Poincaré map $P(\tilde{z})$ of the upper half domain, $[-1, 1] \times [0, 1]$, for $\kappa = 200$. The manifold we choose for the Poincaré map is the vertical line that passes through the unstable nodes (red $\star$) as shown in (b) and (a) is the difference between $\tilde{z}$ and its Poincaré map $P(\tilde{z})$, i.e. $P(\tilde{z}) - \tilde{z}$.

4.4.4 Comparison of ZeLF and detailed numerical models

Recall that the ZeLF model used for the above analysis is an approximation of the detailed numerical model of [HSB19]. We here compare the predictions of particle dynamics of these two models. From the ZeLF model, we have found that the particle dynamics will differ depending on the value of the parameter κ. For small κ ($\lesssim 10$) there are multiple points in the duct cross-section to which particles focus depending on their initial position; for intermediate κ ($10 \lesssim \kappa \lesssim 25$) there is a unique point to which all particles will focus, regardless of their initial position; for large κ ($\gtrsim 25$) there are no stable focus points but particles initially located in the top/bottom half of the duct cross-section will migrate to a periodic orbit in the top/bottom half of the cross-section. Similar changes in particle dynamics are seen using the detailed numerical model but these occur at slightly different values of κ.

Using a square duct with parameters $l = 2$, $80 \leq R \leq 5120$ and $a = 0.05, 0.10, 0.15, 0.20$, Figure 4.13 shows the nature of the particle dynamics predicted by the detailed numerical model of [HSB19] for different values of κ. Also shown, for comparison, are the predictions of

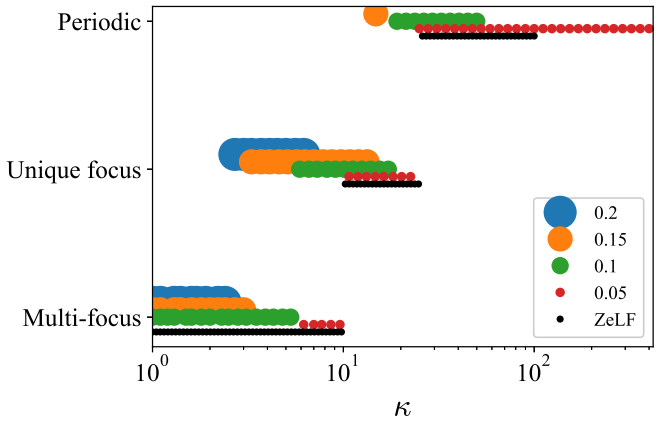

Figure 4.13: κ values and particle flow behavior of the numerical Model. The flow behavior is classified as described in section 4.4.4. The different sized circles indicate the four different sized particles from $a = 0.05$ to 0.2. The black line indicates the flow behavior of the ZeLF model. As the size of the particles decrease the behavior matches that of the ZeLF model. Due to the restriction on the range of R, the data points of particles with size $a = 0.15$ and 0.2 do not fully extend to exhibit the periodic flow behavior.

the ZeLF model which assumes that the particle size is small compared to the size of the duct ($a \ll \ell$) and that the bend radius R is large ($\epsilon \to 0$). There is excellent agreement between the ZeLF model and the numerical model for small particle size. As the particle size increases the numerical model gives transitions between the different behaviors at smaller values of κ, but qualitatively we continue to observe the same three regimes occurring in the same order.

CHAPTER 5

Conclusion

In this thesis, we build a mathematical model for two microfluidic problems - microdroplet formation using DCPs and particle focusing in curved ducts. We analyze the models to investigate their properties and to build a theory behind each phenomenon.

In Chapter 2 and Chapter 3, we develop a mathematical theory for the recently developed DCP technology that generates microdroplets [WOW20, DOD21, RDA22]. One of the benefits of the DCP technology is that it captures a predetermined amount of target fluid after simple mixing. In Chapter 2, we explain that this fluid distribution minimizes the surface tension energy of the system. Based on the previous theory of energy minimizing surfaces [AHV15] we calculate the energy-volume graph of a single axisymmetric particle. Unlike the previous work that focuses on simple geometries such as parallel flat planes, we focus on shapes that are of particular interest in the emerging DCP technologies. With the energy-volume graph of a single DCP, we simulate the fluid exchange assuming that the particles undergo random pairwise interactions. The simulations demonstrate that for sufficiently large total volumes the long-time equilibrium distribution consists of $N-1$ dropicles with the same volume and the N-th one with the remaining large volume. The non-zero volume of the $N-1$ dropicles only depends on the DCP geometry and is the main feature of the DCP system as it creates uniform droplet sizes that work as miniature test tubes for biochemical applications [WOW20]. We prove that this uniform distribution minimizes the energy of the multi-DCP system for DCPs in which the energy curve has certain properties - related to the cavity of the particles. This proof solely depends on the

shape of the energy-volume graph, thus it generalizes to non-axisymmetric DCPs such as the ones described in [WOW20, DOW20, DOD21]. This is advantageous since the microscale limits the number of axisymmetric designs that can be manufactured.

In Chapter 3, we expand on Chapter 2 by comparing the energy volume graph with physical experiments, building a theory on the number of Independent Random Interactions (IRIs), and analyzing the effect of a multi-DCP system with two different sized DCPs. First, we perform controlled splitting experiments of two dropicles. The experiment results agree with the surface energy minimization theory developed in Chapter 2. Next, we develop a theory that calculates the number of IRIs necessary to obtain a uniform distribution in a multi-DCP system. By assuming that the total target fluid volume is large enough, the dropicles divide into three categories (Figure 3.4), which simplifies the types of IRIs that occur. This simplification enables us to calculate the explicit probability density function (PDF) of the required IRIs, which agrees with the simulation results. The analogous experiments and theory are applied to a heterogeneous DCP system - a system with two different-sized particles. Compared to the homogeneous IRIs theory, we demonstrate that the inclusion of large DCPs speeds up the distribution process - up to 10 fold with the right ratio of large DCPs. This is due to the heterogeneous systems not having an Even-Splitting Range (Figure 3.3). The heterogeneous IRIs theory provides a method to measure how well a given DCP generates uniform droplets. We optimize the geometries of the cylinder and sphere DCPs using the criteria.

Surface energy minimization theory and the pairwise interaction model explain the uniform distribution of fluid captured in each DCP. However, there are some discrepancies between the experiments and theory. Some of the discrepancies can be explained by extending the application of the surface energy minimization theory. For example, in the experiments, we observe large droplets with multiple DCPs attached to them. This droplet-multiple DCPs complex is equivalent to a single DCP containing a large amount of water and multiple empty DCPs in our analysis: The DCPs detaching from the complex is equivalent to the empty

DCP interacting with the DCP with a large volume. Some discrepancies should be dealt with in more depth. One main concern of the energy minimization model is that it ignores the effect of fluid dynamics. As the heterogeneous two-particle splitting experiments demonstrate in Chapter 3, the effect of fluid dynamics can result in local energy minimum configurations. In the applications, the effect of fluid dynamics will become more important as Table. 3.1 suggests. For example, it should perform an important role in splitting the DCPs apart, since if we consider only the surface tension energy, the energy minimizing configuration is all the DCPs attached to a single large droplet. We do not observe such configurations after sufficient agitation, suggesting that the fluid dynamics break the large droplets and DCPs into uniform dropicles. Understanding how this occurs will further guide the design of DCPs.

In Chapter 4, we study the particle focusing phenomenon flowing down a curved square duct. Building on previous work [HSB19] we develop a simplified model for the migration of a small neutrally buoyant spherical particle suspended in relatively slow flow through microfluidic curved ducts with a square cross-section. While curved ducts with a square cross-section are not as effective as rectangular (or other) cross-sections for particle separation by size, they exhibit a wide range of interesting bifurcations. We model the inertial lift force by first fitting the zero level curves to data obtained from simulations of a small particle in a straight duct. Then, multiplying by the exponential of a polynomial in the cross-section coordinates, we fit the inertial lift force over the entire cross-section in a manner that does not modify the zero level curves already modeled. This two-step process captures the correct topology of the inertial lift force and correctly predicts equilibria for large bend radii. To this, we add a simple drag force model to capture the effect of the secondary motion of the background flow. The ratio of the secondary drag to inertial lift forces is parameterized by a single dimensionless variable κ. Unlike previous studies, we also incorporate travel along the duct into the trajectory model to enable an analysis of the time and distance required for particles to focus. Using this model we identify three different κ regions with distinctive flow behavior and analyze the dynamics of each region and the bifurcations between the

regions. We also introduce a simple criterion to categorize these three κ behavior. This categorization aids in identifying appropriate ranges of physical parameters when designing a curved duct for focusing purposes. The methodology and analysis applied to extract and understand the κ dependence of the model can be applied to other shaped ducts as well. In addition, we show that a duct of a given length will focus particles over a range of κ values. This is an important observation as it establishes that a single device design can focus multiple particle sizes simultaneously. This approach has been applied to rectangular ducts as well [VHS21]. It will be interesting to study if this observation holds for other duct shapes and/or non-spherical particles, in which the focusing points for particles of different sizes have sufficiently different radial coordinates to enable practical particle separation.

REFERENCES

[ABS03] S. L. Anna, N. Bontoux, and H. A. Stone. "Formation of dispersions using "flow focusing" in microchannels." *Applied Physics Letters*, **82**(3):364–366, 2003.

[AHV15] A. Akbari, R. J. Hill, and T. G. van de Ven. "Catenoid stability with a free contact line." *SIAM Journal on Applied Mathematics*, **75**(5):2110–2127, 2015.

[AP98] U. M. Ascher and L. R. Petzold. *Computer methods for ordinary differential equations and differential-algebraic equations*, volume 61. SIAM, 1998.

[Asm99] E. S. Asmolov. "The inertial lift on a spherical particle in a plane Poiseuille flow at large channel Reynolds number." *Journal of Fluid Mechanics*, **381**:63–87, 1999.

[BBH10] A. A. S. Bhagat, H. Bow, H. W. Hou, S. J. Tan, J. Han, and C. T. Lim. "Microfluidics for cell separation." *Medical & biological engineering & computing*, **48**(10):999–1014, 2010.

[BBW98] A. J. Bernoff, A. L. Bertozzi, and T. P. Witelski. "Axisymmetric surface diffusion: dynamics and stability of self-similar pinchoff." *Journal of Statistical Physics*, **93**(3-4):725–776, 1998.

[BHW07] N. R. Beer, B. J. Hindson, E. K. Wheeler, S. B. Hall, K. A. Rose, I. M. Kennedy, and B. W. Colston. "On-chip, real-time, single-copy polymerase chain reaction in picoliter droplets." *Analytical Chemistry*, **79**(22):8471–8475, 2007.

[Bru19] N. D. Brubaker. "Two-dimensional capillary origami with inextensibility and free triple-contact points." *SIAM Journal on Applied Mathematics*, **79**(2):572–593, 2019.

[BS15] J. Bostwick and P. Steen. "Stability of constrained capillary surfaces." *Annual Review of Fluid Mechanics*, **47**, 2015.

[CND15] D. J. Collins, A. Neild, A. DeMello, A.-Q. Liu, and Y. Ai. "The Poisson distribution and beyond: methods for microfluidic droplet production and single cell encapsulation." *Lab on a Chip*, **15**(17):3439–3459, 2015.

[Di 09] D. Di Carlo. "Inertial microfluidics." *Lab on a Chip*, **9**(21):3038–3046, 2009.

[DLN21] R. S. Du, L. Liu, S. Ng, S. Sambandam, B. H. Adame, H. Perez, K. Ha, C. Falcon, J. de Rutte, D. Di Carlo, et al. "Statistical energy minimization theory for systems of drop-carrier particles." *Physical Review E*, **104**(1):015109, 2021.

[DOD21] G. Destgeer, M. Ouyang, and D. Di Carlo. "Engineering design of concentric amphiphilic microparticles for spontaneous formation of picoliter to nanoliter droplet volumes." *Analytical Chemistry*, **93**(4):2317–2326, 2021.

[DOW20] G. Destgeer, M. Ouyang, C.-Y. Wu, and D. Di Carlo. "Fabrication of 3D concentric amphiphilic microparticles to form uniform nanoliter reaction volumes for amplified affinity assays." *Lab on a Chip*, 2020.

[DST21] D. Davini, B. Samineni, B. Thomas, A. H. Tran, C. Zhu, K. Ha, G. Dasika, and L. White. "Using physics-informed regularization to improve extrapolation capabilities of neural networks." *Neurips 2021 Poster session*, 2021.

[EGD70] M. A. Erle, R. Gillette, and D. Dyson. "Stability of interfaces of revolution with constant surface tension-the case of the catenoid." *The Chemical Engineering Journal*, **1**(2):97–109, 1970.

[FGT92] P. Flajolet, D. Gardy, and L. Thimonier. "Birthday paradox, coupon collectors, caching algorithms and self-organizing search." *Discrete Applied Mathematics*, **39**(3):216–217, 1992.

[GD71] R. Gillette and D. Dyson. "Stability of fluid interfaces of revolution between equal solid circular plates." *The Chemical Engineering Journal*, **2**(1):44–54, 1971.

[GD72] R. Gillette and D. Dyson. "Stability of axisymmetric liquid-fluid interfaces towards general disturbances." *The Chemical Engineering Journal*, **3**:196–199, 1972.

[GF14] T. M. Geislinger and T. Franke. "Hydrodynamic lift of vesicles and red blood cells in flow — from Fåhræus and Lindqvist to microfluidic cell sorting." *Advances in Colloid and Interface Science*, **208**:161–176, 2014.

[GH13] J. Guckenheimer and P. Holmes. *Nonlinear oscillations, dynamical systems, and bifurcations of vector fields*, volume 42. Springer Science & Business Media, 2013.

[GHH20] R. Grotheer, L. Huang, Y. Huang, A. Kryshchenko, O. Kryshchenko, P. Li, X. Li, E. Rebrova, K. Ha, and D. Needell. "Covid-19 literature topic-based search via hierarchical nmf." In *Proceedings of the 1st Workshop on NLP for COVID-19 (Part 2) at EMNLP 2020*, 2020.

[Har18] B. Harding. "A study of inertial particle focusing in curved microfluidic ducts with large bend radius and low flow rate." In *Proceedings of the 21st Australasian Fluid Mechanics Conference, Adelaide, South Australia, Australia*. Australasian Fluid Mechanics Society, 2018. Contribution number 603.

[Har19] B. Harding. "A Rayleigh–Ritz method for Navier–Stokes flow through curved ducts." *The ANZIAM Journal*, **61**(1):1–22, 2019.

[HHB22] K. Ha, B. Harding, A. L. Bertozzi, and Y. M. Stokes. "Dynamics of small particle inertial migration in curved square ducts." *SIAM Journal on Applied Dynamical Systems*, **21**(1):714–734, 2022.

[HKD16] K. Hood, S. Kahkeshani, D. Di Carlo, and M. Roper. "Direct measurement of particle inertial migration in rectangular microchannels." *Lab on a Chip*, **16**(15):2840–2850, 2016.

[HL74] B. P. Ho and L. G. Leal. "Inertial migration of rigid spheres in two-dimensional unidirectional flows." *Journal of Fluid Mechanics*, **65**(2):365–400, 1974.

[HLR15] K. Hood, S. Lee, and M. Roper. "Inertial migration of a rigid sphere in three-dimensional Poiseuille flow." *Journal of Fluid Mechanics*, **765**:452–479, 2015.

[HN19] B. Hanysz and W. Nowicki. "The capillary bistable switch constrained by pinning/wetting angles as a sensor of pressure." *The European Physical Journal E*, **42**(9):1–5, 2019.

[HRD22] K. Ha, J. de Rutte, D. Di Carlo, and A. L Bertozzi. "Surface energy minimizing configurations for axisymmetric microparticles." *Journal of Engineering Mathematics*, **134**(1):1–19, 2022.

[HS19] T. C. Hagen and P. H. Steen. "Volume scavenging of networked droplets." *Physica D: Nonlinear Phenomena*, **394**:1–15, 2019.

[HS20] B. Harding and Y. M. Stokes. "Inertial focusing of non-neutrally buoyant spherical particles in curved microfluidic ducts." *Journal of Fluid Mechanics*, **902**, 2020.

[HSB19] B. Harding, Y. M. Stokes, and A. L. Bertozzi. "Effect of inertial lift on a spherical particle suspended in flow through a curved duct." *Journal of Fluid Mechanics*, **875**:1–43, 2019.

[KKN97] T. Kawakatsu, Y. Kikuchi, and M. Nakajima. "Regular-sized cell creation in microchannel emulsification by visual microprocessing method." *Journal of the American Oil Chemists' Society*, **74**(3):317–321, 1997.

[LBF08] H.-W. Lu, F. Bottausci, J. D. Fowler, A. L. Bertozzi, C. Meinhart, et al. "A study of EWOD-driven droplets by piv investigation." *Lab on a Chip*, **8**(3):456–461, 2008.

[LRD21] S. Lee, J. de Rutte, R. Dimatteo, D. Koo, and D. Di Carlo. "Scalable fabrication and use of 3D structured microparticles spatially functionalized with biomolecules." *ACS nano*, 2021.

[LS95] B. J. Lowry and P. H. Steen. "Capillary surfaces: stability from families of equilibria with application to the liquid bridge." *Proceedings of the Royal Society of London. Series A: Mathematical and Physical Sciences*, **449**(1937):411–439, 1995.

[LS97] B. J. Lowry and P. H. Steen. "Stability of slender liquid bridges subjected to axial flows." *Journal of Fluid Mechanics*, **330**:189–213, 1997.

[LSB13] M. G. Lee, J. H. Shin, C. Y. Bae, S. Choi, and J.-K. Park. "Label-free cancer cell separation from human whole blood using inertial microfluidics at low shear stress." *Analytical chemistry*, **85**(13):6213–6218, 2013.

[MBK87] A. D. Myshkis, V. G. Babskii, N. D. Kopachevskii, L. A. Slobozhanin, and A. D. Tyuptsov. *Low-gravity fluid mechanics: mathematical theory of capillary phenomena*. Springer, 1987.

[MBS15] E. Z. Macosko, A. Basu, R. Satija, J. Nemesh, K. Shekhar, M. Goldman, I. Tirosh, A. R. Bialas, N. Kamitaki, E. M. Martersteck, J. J. Trombetta, D. A. Weitz, J. R. Sanes, A. K. Shalek, A. Regev, and S. A. McCarroll. "Highly parallel genome-wide expression profiling of individual cells using nanoliter droplets." *Cell*, **161**(5):1202–1214, 2015.

[MC65] G. Mason and W. Clark. "Liquid bridges between spheres." *Chemical Engineering Science*, **20**(10):859–866, 1965.

[MHR10] D. Mark, S. Haeberle, G. Roth, F. von Stetten, and R. Zengerle. "Microfluidic lab-on-a-chip platforms: requirements, characteristics and applications." *Chem. Soc. Rev.*, **39**:1153–1182, 2010.

[MLR19] G. J. McLachlan, S. X. Lee, and S. I. Rathnayake. "Finite mixture models." *Annual review of statistics and its application*, **6**:355–378, 2019.

[MMG04] J.-P. Matas, J. F. Morris, and É. Guazzelli. "Inertial migration of rigid spherical particles in poiseuille flow." *Journal of Fluid Mechanics*, **515**:171–195, 2004.

[MRK20] H. E. Munoz, C. T. Riche, J. E. Kong, M. van Zee, O. B. Garner, A. Ozcan, and D. Di Carlo. "Fractal lamp: Label-free analysis of fractal precipitate for digital loop-mediated isothermal nucleic acid amplification." *ACS Sensors*, **5**(2):385–394, 2020.

[MT14] J. M. Martel and M. Toner. "Inertial focusing in microfluidics." *Annual Review of Biomedical Engineering*, **16**(1):371–396, 2014.

[NAM13] S. Neukirch, A. Antkowiak, and J.-J. Marigo. "The bending of an elastic beam by a liquid drop: A variational approach." *Proceedings of the Royal Society A: Mathematical, Physical and Engineering Sciences*, **469**(2157):20130066, 2013.

[NK12] W. C. Nelson and C.-J. Kim. "Droplet actuation by electrowetting-on-dielectric (EWOD): A review." *Journal of Adhesion Science and Technology*, **26**(12-17):1747–1771, 2012.

[PMC00] O. Pitois, P. Moucheront, and X. Chateau. "Liquid bridge between two moving spheres: an experimental study of viscosity effects." *Journal of Colloid and Interface Science*, **231**(1):26–31, 2000.

[RC18] R. Rasooli and B. Cetin. "Assessment of lagrangian modeling of particle motion in a spiral microchannel for inertial microfluidics." *Micromachines*, **9**(9):433, 2018.

[RDA22] J. de Rutte, R. Dimatteo, M. M. Archang, M. van Zee, D. Koo, S. Lee, A. C. Sharrow, P. J. Krohl, M. Mellody, S. Zhu, et al. "Suspendable hydrogel nanovials for massively parallel single-cell functional analysis and sorting." *ACS nano*, 2022.

[REM05] Y. I. Rabinovich, M. S. Esayanur, and B. M. Moudgil. "Capillary forces between two spheres with a fixed volume liquid bridge: theory and experiment." *Langmuir*, **21**(24):10992–10997, 2005.

[RS86] M. J. Russo and P. H. Steen. "Instability of rotund capillary bridges to general disturbances: experiment and theory." *Journal of Colloid and Interface Science*, **113**(1):154–163, 1986.

[RSR17] H. Ramachandraiah, H. A. Svahn, and A. Russom. "Inertial microfluidics combined with selective cell lysis for high throughput separation of nucleated cells from whole blood." *RSC Advances*, **7**(47):29505–29514, 2017.

[SAP02] L. A. Slobozhanin, J. I. D. Alexander, and V. D. Patel. "The stability margin for stable weightless liquid bridges." *Physics of Fluids*, **14**(1):209–224, 2002.

[SH89] J. A. Schonberg and E. J. Hinch. "Inertial migration of a sphere in Poiseuille flow." *Journal of Fluid Mechanics*, **203**:517–524, 1989.

[SP96] L. A. Slobozhanin and J. M. Perales. "Stability of an isorotating liquid bridge between equal disks under zero-gravity conditions." *Physics of Fluids*, **8**(9):2307–2318, 1996.

[SR20] P. Shi and R. Rzehak. "Lift forces on solid spherical particles in wall-bounded flows." *Chemical Engineering Science*, **211**:115264, 2020.

[SS61] G. Segre and A. Silberberg. "Radial particle displacements in Poiseuille flow of suspensions." *Nature*, **189**(4760):209–210, 1961.

[SSA12] L. A. Slobozhanin, V. M. Shevtsova, J. I. D. Alexander, J. Meseguer, and J. M. Montanero. "Stability of liquid bridges between coaxial equidimensional disks to axisymmetric finite perturbations: a review." *Microgravity Science and Technology*, **24**(2):65–77, 2012.

[Str92] D. Strube. "Stability of a spherical and a catenoidal liquid bridge between two parallel plates in the absence of gravity." In *Microgravity Fluid Mechanics*, pp. 263–269. Springer, 1992.

[Str10] R. L. Streit. "The Poisson point process." In *Poisson Point Processes*, pp. 11–55. Springer, 2010.

[TCL06] Y.-C. Tan, V. Cristini, and A. P. Lee. "Monodispersed microfluidic droplet generation by shear focusing microfluidic device." *Sensors and Actuators B: Chemical*, **114**(1):350–356, 2006.

[TSO92] M. Tjahjadi, H. A. Stone, and J. M. Ottino. "Satellite and subsatellite formation in capillary breakup." *Journal of Fluid Mechanics*, **243**:297–317, 1992.

[VHS21] R. N. Valani, B. Harding, and Y. M. Stokes. "Bifurcations in inertial focusing of a particle suspended in flow through curved rectangular ducts." *arXiv preprint arXiv:2112.04658*, 2021.

[Vog87] T. I. Vogel. "Stability of a liquid drop trapped between two parallel planes." *SIAM Journal on Applied Mathematics*, **47**(3):516–525, 1987.

[Vog89] T. I. Vogel. "Stability of a liquid drop trapped between two parallel planes ii: General contact angles." *SIAM Journal on Applied Mathematics*, **49**(4):1009–1028, 1989.

[VS10] M. J. Vogel and P. H. Steen. "Capillarity-based switchable adhesion." *Proceedings of the National Academy of Sciences*, **107**(8):3377–3381, 2010.

[WB10] D. Wang and S. Bodovitz. "Single cell analysis: the new frontier in 'omics'." *Trends in Biotechnology*, **28**(6):281 – 290, 2010.

[Wen99] H. C. Wente. "A surprising bubble catastrophe." *Pacific Journal of Mathematics*, **189**(2):339–375, 1999.

[WGL14] M. E. Warkiani, G. Guan, K. B. Luan, W. C. Lee, A. A. S. Bhagat, P. Kant Chaudhuri, D. S.-W. Tan, W. T. Lim, S. C. Lee, P. C. Y. Chen, C. T. Lim, and J. Han. "Slanted spiral microfluidics for the ultra-fast, label-free isolation of circulating tumor cells." *Lab on a Chip*, **14**:128–137, 2014.

[WGZ14] B. L. Wang, A. Ghaderi, H. Zhou, J. Agresti, D. A. Weitz, G. R. Fink, and G. Stephanopoulos. "Microfluidic high-throughput culturing of single cells for selection based on extracellular metabolite production or consumption." *Nature Biotechnology*, **32**(5):473–478, 2014.

[WKW16] M. E. Warkiani, B. L. Khoo, L. Wu, A. K. P. Tay, A. A. S. Bhagat, J. Han, and C. T. Lim. "Ultra-fast, label-free isolation of circulating tumor cells from blood using spiral microfluidics." *Nature Protocols*, **11**(1):134–148, 2016.

[WLW12] L. Wang, D. Liu, X. Wang, and X. Han. "Mixing enhancement of novel passive microfluidic mixers with cylindrical grooves." *Chemical engineering science*, **81**:157–163, 2012.

[WOW20] C.-Y. Wu, M. Ouyang, B. Wang, J. de Rutte, A. Joo, M. Jacobs, K. Ha, A. L. Bertozzi, and D. Di Carlo. "Monodisperse drops templated by 3D-structured microparticles." *Science Advances*, **6**(45), 2020.

[XZG17] H.-D. Xi, H. Zheng, W. Guo, A. M. Gañán-Calvo, Y. Ai, C.-W. Tsao, J. Zhou, W. Li, Y. Huang, N.-T. Nguyen, et al. "Active droplet sorting in microfluidics: a review." *Lab on a Chip*, **17**(5):751–771, 2017.

[Zho97] L. Zhou. "On stability of a catenoidal liquid bridge." *Pacific Journal of Mathematics*, **178**(1):185–198, 1997.